University of Cincinnati

Date: 7/1/2015

I, Anna S Nagle , hereby submit this original work as part of the requirements for the degree of Doctor of Philosophy in Biomedical Engineering.

It is entitled:

Biomechanical Measurements of the Human Female Levator Ani Muscle Ex Vivo and In Vivo

Student's name: **Anna S Nagle**

This work and its defense approved by:

Committee chair: T. Douglas Mast, Ph.D.

Committee member: Ryo Minoguchi,

Committee member: Balakrishna Haridas, PH.D.

Committee member: Jing-Huei Lee, Ph.D.

16267

Biomechanical measurements of the human female levator ani muscle *ex vivo* and *in vivo*

A dissertation submitted to the
Graduate School
of the University of Cincinnati
in partial fulfillment of the
requirements for the degree of

Doctor of Philosophy

in the Biomedical Engineering Program
of the College of Engineering and Applied Science
by

Anna S. Nagle

June 2015

Dissertation Committee:
T. Douglas Mast (Chair)
Balakrishna Haridas
Jing-Huei Lee
Ryo Minoguchi

Abstract

Pelvic floor disorders (PFD) are highly prevalent in women but little is understood about their development at a biomechanical level even though such knowledge could help to prevent, diagnose, and treat PFD. Of particular importance to preventing pelvic organ prolapse and stress urinary incontinence are the biomechanical properties of the pubovisceral muscle (PVM): the portion of the levator ani which forms a sling around the urethra and vagina. The goal of this research is to measure the biomechanics of the levator ani, particularly at low strains. This dissertation presents biomechanical measurements of cadaveric levator ani, the validation of a correlation-based texture tracking algorithm on an *ex vivo* model of the PVM, and the use of the texture tracking algorithm on *in vivo* images of the PVM to measure strain.

To determine the passive behavior of the levator ani at low strains, nine post-menopausal, thawed, fresh-frozen female cadavers were dissected to obtain samples of the levator ani for uniaxial extension testing. The nine samples underwent preconditioning and uniaxial biomechanical analysis in the fiber direction on a tensile testing apparatus after the original width, thickness, and length were measured. The load extension data and measured dimensions were used to calculate stress-strain curves for each sample. The resulting stress-strain curves up to 10% strain were fit to five different constitutive models to determine which model was most appropriate for the data. A power-law model with two parameters was found to fit the data most accurately. Constitutive parameters did not correlate significantly with age in this study; this may be because all of the cadavers were post-menopausal.

To validate and optimize a correlation-based texture tracking algorithm to measure displacement and strain on volumetric ultrasound images of the PVM, an *ex vivo* model was constructed using bovine skeletal muscle. A sonomicrometry system was used to provide an independent measure of strain while the model was deformed by a series of small inden-

tations and volumetric ultrasound images were obtained. Two likelihood functions for the algorithm were compared: an exponential sum function proposed by Clocksin et al. (2002) and the more common Pearson correlation coefficient. Strains were computed using both likelihood functions over a range of sizes for the tracked tissue sub-volume to determine an optimum sub-volume size. Echo decorrelation of the ultrasound signal was compared to accuracy of the texture tracking algorithm by analyzing images separated by increasing indentation sizes. Sub-volumes three to four times the image correlation length yielded the smallest strain errors. The two likelihood functions provided comparable results overall, with the Pearson likelihood yielding slightly higher root-mean-square errors than the Clocksin likelihood at most of the sub-volume sizes investigated. A series of small, incremental strains yielded lower levels of decorrelation of the ultrasound signal and resulted in more accurate strain tracking than larger increments of strain. At the optimal sub-volume sizes, strains were measured in the PVM model with accuracy sufficient for useful characterization of the levator ani *in vivo*.

To test the feasibility of using the optimized algorithm to measure PVM strain *in vivo*, six women were recruited to undergo an imaging procedure. Volumetric translabial ultrasound images were obtained while the PVM was deformed incrementally using a transvaginal cylindrical balloon catheter with an inline pressure transducer. The texture tracking algorithm was used to measure strain in the anterior and posterior regions of the PVM on the left and the right side. Stiffness was calculated as the estimated intra-abdominal pressure divided by the strain. No statistical differences were found between PVM stiffness in different regions nor between the women who had PFD and the women who were asymptomatic. The procedure was shown to be feasible, but could be improved with better setup and improvements to the texture tracking algorithm.

The biomechanical information on the levator ani obtained both *ex vivo* and *in vivo* in this dissertation can be used to better model the levator ani, and the techniques developed

can enable future studies to obtain more knowledge about levator ani biomechanics. This information will be important in the prevention and treatment of PFD by helping clinicians make earlier and more precise diagnoses and by helping engineers to make more accurate models of the causes of PFD.

Acknowledgements

This work was supported by NSF grant #IIP-0652208, NSF grant #DGE-0528532, and NIH grant R01 CA158439.

I would like to thank all the faculty members, staff members at UC and at P&G, post-docs, graduate students, and undergraduate students who have worked hard on the projects involved in this dissertation and all the people who have helped me along the way. This long list includes Doug Mast, Balakrishna Haridas, Jing-Huei Lee, Ryo Minoguchi, Melanie Hansmann, John Norcom, Marepalli Rao, Ashok Nageswaran, Gaurav Srivastava, Chris Weidner, Rahul Ramachandran, John Vennemeyer, Jason Kleinhenz, Ananth Gopalakrishnan, Saurabh Datta, Vasant Salgaonkar, Chandra Priya Karunakaran, Swetha Subramanian, Kyle Rich, Tyler Fosnight, Fong Ming Hooi, Mark Burgess, Amel Alqadah, Cameron Hoerig, Ryan Keil, Teckla Akinyi, Kevin Haworth, Jason Raymond, Jonathan Kopechek, Kate Hitchcock, Steven Perrin, Matthew Gruber, Kirthi Radhakrishnan, Jonathan Sutton, Nik Ivancevich, Kenneth Bader, Guillaume Bouchoux, Jennifer Hurley, Varun Krishnamurthy, Swathi Balaji, Kristen Kinneberg, Mike Sanderson, Denis Bailey, Linda Moeller, Lori Beth Derenski, Martin Molony, Steven Kleeman, Ann Choe, and Matthew Barker.

TABLE OF CONTENTS

LIST OF FIGURES

Figure

LIST OF TABLES

Table

Chapter I

Introduction

1.1 Background

1.1.1 Clinical significance: Pelvic Floor Disorders

Pelvic floor disorders (PFD) include a spectrum of interrelated conditions including voiding, defecation, and sexual dysfunctions as well as pelvic organ prolapse, of which urinary incontinence, anal incontinence, and prolapse are the most common (Bourcier et al., 2004; Jelovsek and Barber, 2006). Urinary incontinence can be subdivided into stress urinary incontinence, where leakage occurs when there is an increase in intra-abdominal pressure, and urge urinary incontinence, where the patient feels the urge to urinate abnormally frequently, often due to overactive bladder (Steers, 2002; Weber and Brubaker, 2004). Anal incontinence occurs when there is leakage of solid and/or liquid feces; some studies also include leakage of flatal gas (Lawrence et al., 2008; Weber and Brubaker, 2004). Pelvic organ prolapse occurs when pelvic organs herniate into the vagina; common types include cystocele (prolapse of the bladder), rectocele (prolapse of the rectum), and enterocele (prolapse of the small bowel) (Bump et al., 1996; Weber and Brubaker, 2004).

PFD adversely impact women (and to a smaller degree, men) in a myriad of ways. Although PFD are unlikely to cause death or severe morbidity, they lower quality of life

and body image (Jelovsek and Barber, 2006). Women with prolapse have a lower body image than those without, and this lowered body image affects their personal relationships, work, and daily activities (Lowder et al., 2010). A study of middle-aged women showed that urinary incontinence severity was negatively correlated to quality of life, even when adjusted for compounding factors such as age and education level (Saadoun et al., 2006).

Estimates of prevalence of PFD based on response to questionnaires vary due to different definitions and methodologies, but it is clear these are common conditions (Barber, 2007). A survey by Lawrence et al. (2008) for women in California aged 25 to 84 showed that stress urinary incontinence affected 15%, overactive bladder affected 13%, pelvic organ prolapse affected 6%, and anal incontinence affected 25% of respondents. A similar survey by Wu et al. (2014) for non-pregnant women aged 20 and over in the United States found that urinary incontinence affected 17.1%, fecal incontinence affected 9.4%, and pelvic organ prolapse affected 2.9% of respondents

Significant risk factors of PFD include increased vaginal parity (number of vaginal births), number of pregnancies, age (particularly menopausal status), obesity, and having had a hysterectomy (Wu et al., 2014; Lawrence et al., 2008), of which vaginal parity is the greatest (DeLancey et al., 2003). Because obesity and age are important risk factors for PFD, PFD prevalence is expected to increase as the population ages and the obesity epidemic continues (Wu et al., 2009), though there was no statistically significant increase in prevalence from 2005 to 2010 based on surveys of women in the United States (Wu et al., 2014).

With pregnancy and parity key risk factors for PFD, it is understandable that PFD are far more common in women than men. Urinary incontinence was reported for 26.3% of women and 5.0% of men in a 1999 study done in Austria (Temml et al., 2000). A study in the 2000s in the United States found that urinary incontinence was reported in 51.1% of women and 13.9% of men (Markland et al., 2011). It is not clear if the approximate doubling in rate of incontinence is due to the time period, location, methodology, or other factors.

1.1.2 Pelvic Floor Anatomy

To understand the mechanisms behind pelvic floor disorders in women, it is important to have an understanding of the anatomy of the female pelvic support structures, though there is not a consensus of how to describe the pelvic floor (Kearney et al., 2004). For example, Bourcier et al. (2004) consider the pelvic floor to consist of the levator ani muscle (LA) and the coccygeus while Weber and Brubaker (2004) consider the coccygeus to be part of the levator ani itself and describes the pelvic floor as the levator ani muscle and its associated connective tissue attachments. Bourcier et al. (2004) describe the LA as consisting of four main parts: the ilioccygeus, the pubococcygeus, the pubovaginalis, and the puborectalis. Weber and Brubaker (2004) describe the LA as two main parts: the diaphragmatic part consisting of the coccygeus and the ilioccygeus muscles and the pubovisceral part consisting of the pubococcygeus and the puborectalis. In a literature review by Kearney et al. (2004), the pelvic floor anatomy was described by 16 different overlapping terms for different parts of the muscle even though the actual anatomy in terms of origin-insertion pairs was consistent.

To explain the anatomy in more detail, the terminology from Bourcier et al. (2004) will be used throughout this dissertation unless otherwise specified. The LA spans the bony pelvic ring with the pubic bones anteriorly, the ischial spines laterally, and the sacrum posteriorly and is the effective contractile support structure of the region. The medial fibers that attach the pubis to the lateral vaginal wall form the pubovaginalis. Other medial fibers from the pubis fuse with the external anal sphincter to form the puborectalis. Still other fibers from the pubis extend to the fascia covering the obturator internus to form the puboccygeus. The illioccygeus is the portion of the levator ani that arises from the lateral wall of the pelvis posteriorly to the ischial spine. The coccygeus forms a fibromuscular sheet that forms a triangle attaching to the ischial spines and the lateral surface of the coccyx and the sacrum, but does not contribute to active movement of the pelvic floor. The connective tissue that

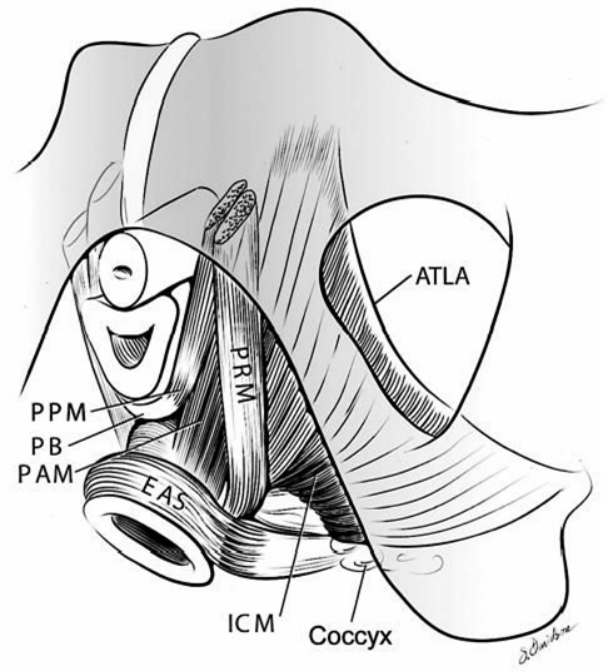

Figure 1.1: Diagram from Kearney et al. (2004) depicting the levator ani muscle seen from below. The following abbreviations are used: ATLA = arcus tendineus levator ani, EAS = external anal sphincter, ICM = iliococcygeal muscle, PAM = puboanal muscle, PB = perinial body, PPM = puboperineal muscle, and PRM = puborectal muscle.

attaches the pelvic organs to the pelvic walls is the endopelvic fascia and consists of collagen, elastin, smooth muscle, blood vessels, and nerves. The arcus tendineus is a fibrous band that is stretched from the pubic bone to the ischial spine on both sides of the pelvis (Bourcier et al., 2004). Figures 1.1 and 1.2 show the anatomy using the Federative Committee on Anatomical Terminology (1998) terminology system. In this system, the puboccygeus is divided into the puboperinealis and the puboanalis (Kearney et al., 2004).

The portions of the LA that attach to the pubic bone, known as the pubococcygeus, puboovaginalis, and puborectalis, are impossible to differentiate in MRI and ultrasound imaging (Dietz et al., 2005). For the rest of this dissertation, they will be collectively referred to as the pubovisceral muscle (PVM) following the convention of DeLancey et al. (2003) and Dietz et al. (2005).

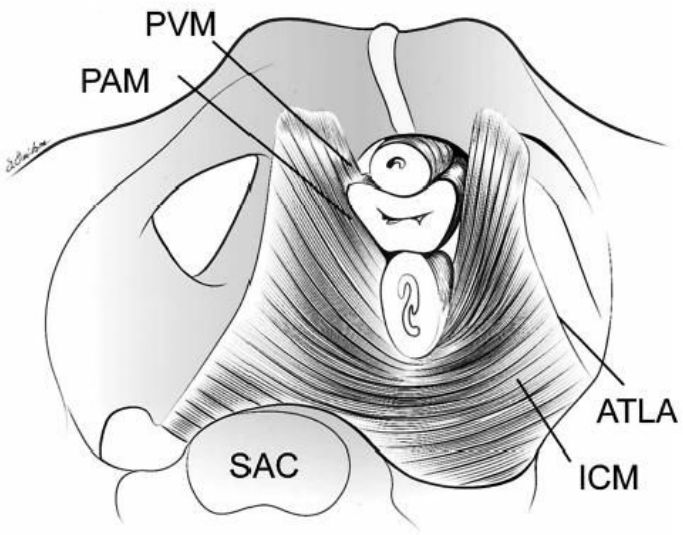

Figure 1.2: Diagram from Kearney et al. (2004) depicting the levator ani muscle seen from above. The following abbreviations are used: ATLA = arcus tendineus levator ani, ICM = iliococcygeal muscle, PAM = puboanal muscle, PVM = pubovaginal muscle, and SAC = sacral promontory.

The opening in the LA through which the urethra, vagina, and rectum pass is called the urogenital hiatus (Ashton-Miller and DeLancey, 2007). The rectum is not included in the name, because the LA attaches directly to the anus (Ashton-Miller and DeLancey, 2007). The LA is a skeletal muscle with a constant baseline tone that keeps the hiatus closed by compressing the urethra, vagina, and rectum against the public bone (Weber and Brubaker, 2004; Ashton-Miller and DeLancey, 2007). Through providing this closure pressure, it helps to prevent urinary and fecal incontinence and is the key factor in preventing prolapse (Ashton-Miller and DeLancey, 2007). When the LA functions properly, the endopelvic fascia serve to stabilize the pelvic organs in their positions above the LA with minimal tension (Ashton-Miller and DeLancey, 2007). When the LA is damaged, the pelvic floor opens, putting additional strain on the suspensory ligaments, causing them to stretch and eventually fail, allowing the pelvic organs to prolapse (Ashton-Miller and DeLancey, 2007). During moments of increased intra-abdominal pressure, such as a sneeze or cough,

the LA contracts to support the urethra through the endopelvic fascia (Ashton-Miller and DeLancey, 2007). If the endopelvic fascia has breaks in its continuity, the LA has damage, or the connection between the LA and the fascia is broken, the urethra's support will become overly compliant leading to stress urinary incontinence (Ashton-Miller and DeLancey, 2007).

The mechanisms behind maintaining continence and pelvic organ support are complex and depend on factors including pelvic floor muscle speed, strength, timing, and coordination (Devreese et al., 2004). In a study by Devreese et al. (2004) comparing age matched continent and incontinent women, the pelvic floor muscle resting tone did not significantly differ between the two groups. What was significantly different was the strength of the pelvic floor contraction as well as the coordination of the contraction during a cough (Devreese et al., 2004). It is likely that the most important factor to pelvic organ prolapse is the biomechanical parameters of the pubovisceral portion (PVM) of the levator ani. Finite element models show that whether or not other support structures are damaged, prolapse can only occur if the PVM is impaired (Chen et al., 2006)

There is still little knowledge on what about the pelvic floor morphology and function contributes to its damage during childbirth (Siafarikas et al., 2015). The vagina, cervix, and pelvic floor undergo remodeling during pregnancy to permit higher strains than could normally be sustained (Fung, 1993). Forcep use in delivery, prolonged second stage of labor, and large infant size are correlated to damage to the PVM and to prolapse (Ashton-Miller and DeLancey, 2009).

1.1.3 Levator Ani Biomechanics

Knowledge of the stress-strain relationship of a material is essential to allow the formation of boundary-value problems and for predictions to be made and tested (Fung, 1993). One important way to study PFD is to create finite element models which can study the development of disorders from different damages to the pelvic support structures (Li et al.,

2010b). One issue limiting the use of finite element models are the lack of validated material models for the pelvic floor structures (Ren et al., 2015). Several groups have constructed finite element models (FEM) of the LA to simulate vaginal childbirth in order to map locations of high stress and likely damage that could lead to PFD (Li et al., 2010b). By modeling childbirth, it may be possible to pinpoint mechanisms of LA injury that may lead to better treatment of the PFD that may result from the injuries. In addition to modeling childbirth, modeling the LA of women with PDF allows the mechanisms of the disorders to be better understood, which will lead to better PFD treatments (Chen et al., 2009a). Considering that about 30% of PFD surgeries are unsuccessful (DeLancey, 2005), modeling of a patient's LA biomechanics may allow more effective surgery planning and prediction of surgical outcomes.

In a continuum mechanics framework, the relationship between stress and strain in a material is mathematically described with a constitutive equation based on experimental data and assumptions about the material's response to loading (Khraishi and Shen, 2014). Most engineering structural materials can sufficiently be described by one of three major equations: one each for the perfectly elastic solid, the nonviscous fluid, and the Newtonian viscous fluid (Khraishi and Shen, 2014). However, most biological materials require more complicated constitutive equations (Fung, 1994). In these studies, the choice of constitutive equation to model the biomechanics of the pelvic floor can make a large difference (Li et al., 2011). Hyperelastic models are the only way to effectively model finite deformations of soft tissues (Fung, 1993). A strain energy function can be defined based on the state of deformation as a function of the strain components (Fung, 1994; Holzapfel, 2000). The stress is derived by differentiating the strain energy function with respect to the strain (Holzapfel, 2000; Roan and Vemaganti, 2007).

Most biological materials show the features of viscoelasticity consisting of hysteresis, relaxation, and creep (Fung, 1993). An important property of living tissue that when it is subjected to periodic loading, it reaches a steady-state stress-strain loop that is not depen-

dent on the strain rate, meaning that the stress-strain loop is repeatable (Fung, 1994).

Early models of the pelvic floor relied on constitutive properties of other body tissues (Jing, 2010). Li et al. (2010b) notes that studies have used material properties for the heart and facial muscles, despite the large differences in stress-strain responses since they lacked data from the LA itself. More recent studies have used properties based on cadaveric tissues or animal tissue through uniaxial and biaxial mechanical tests (Jing, 2010). Cadaveric tissue can approximate the sub-failure passive properties of the muscle, but are unable to represent the *in vivo* active properties of the muscle (Van Ee et al., 2000).

A number of different animal models have been used in pelvic floor research, though none can fully replicate human biomechanics (Abramowitch et al., 2009). It has been shown that the macro and micro anatomy of the rat's vaginal supportive connective tissue attachments are similar to those of a human, making it a suitable model for pelvic organ prolapse research concerning the contribution of connective tissue (Moalli et al., 2005). However, the rat LA serves to support the tail rather than the pelvic organs as is the case with nearly all quadrupeds (Abramowitch et al., 2009). Non-human primates move in a more bipedal manner with the LA serving an important role in vaginal support, making them a better model for LA research (Abramowitch et al., 2009). Humans give birth in a more complex manner than other primates due to their bipedal posture and relatively larger brains, so the manner and frequency in which the LA is damaged during the birth process is quite different (Parente et al., 2011).

1.1.4 Levator Ani *in vivo* Imaging

Imaging of the pelvic floor is an essential tool to clinicians to diagnose PFDs (Bourcier et al., 2004). It is also of key importance to finite element models by providing the geometry of the organs and tissues (Noakes et al., 2008). There no single imaging technique that can show all kinds of PFD and explain their causes, but there are a number of different

techniques that have their own strengths and weaknesses (Wieczorek et al., 2011). Three important techniques currently in use are magnetic resonance imaging (MRI), radiologic voiding and defecating studies, and ultrasound imaging (Bourcier et al., 2004; Ahmad et al., 2015).

MRI is considered the gold standard for assessing the static anatomy of the pelvic floor muscles, their attachments, and the pelvic organs (Bourcier et al., 2004; Wieczorek et al., 2011). Constantinou et al. (2002) used dynamic MRI to capture images of the pelvic floor in a relaxed and a contracted state in order to measure LA function (Fig. 1.3). The advantages of MRI include a global view of the pelvis, no adverse biologic effects of the imaging modality, high differentiation between tissue types, ability to measure muscle volume, and visualization of defects in the LA (Bourcier et al., 2004; Ahmad et al., 2015). Its drawbacks include high cost, long procedure duration, contraindications with certain patient populations, and slow frame rate (Wieczorek et al., 2011).

Radiologic voiding and defecating studies have the bladder and/or rectum filled with an X-ray opaque fluid and then X-ray images taken at different stages of voiding or defecation (Bourcier et al., 2004). Defecating proctography is the gold standard for diagnosis of rectocele and involves opacification of the small bowel and rectosigmoid with liquid barium contrast (Steensma et al., 2010). Dynamic defecating proctography, also known as cystocolpoproctography, additionally opacifies the vagina (Ahmad et al., 2015). These techniques are useful for assessment of prolapse as well as voiding and defecation dysfunctions difficult to visualize with MRI or ultrasound (Bourcier et al., 2004; Wieczorek et al., 2011). However, they have the very significant disadvantage of exposure to radiation, which means they cannot be used routinely (Ahmad et al., 2015). Other disadvantages including a long and complex procedure, being uncomfortable for the patient, and an inability to visualize the periurethral structions and pelvic floor muscles (Bourcier et al., 2004; Steensma et al., 2010).

Ultrasound imaging is useful for visualizing a range of pathological features and is espe-

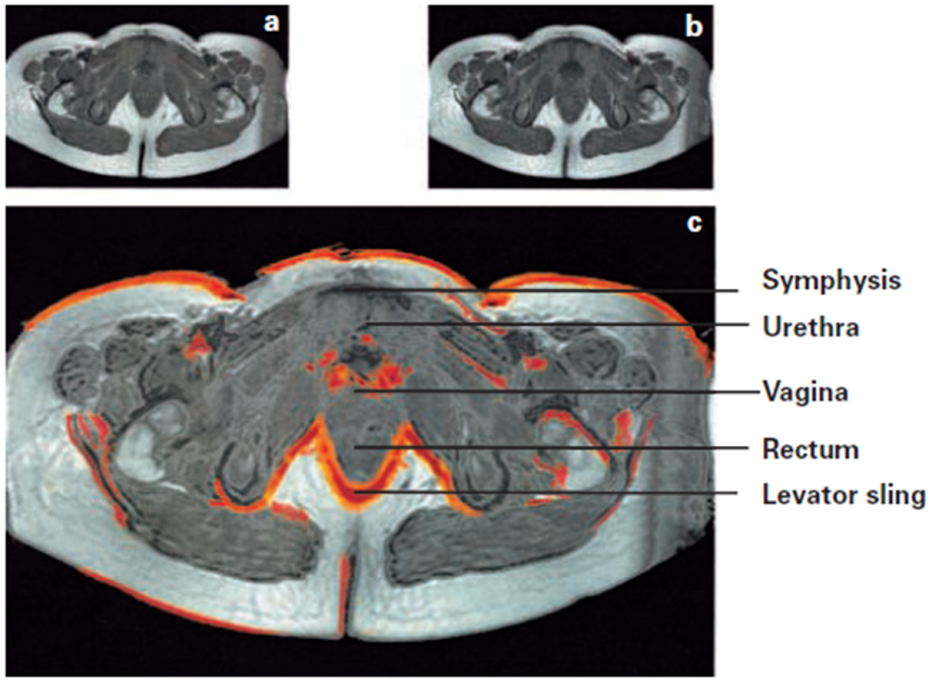

Figure 1.3: MRI from Constantinou et al. (2002) used to calculate range of pelvic floor displacement, including an axial view of the subject before (a) and after (b) a pelvic floor contraction. The composite image (c) shows the difference between a and b in orange.

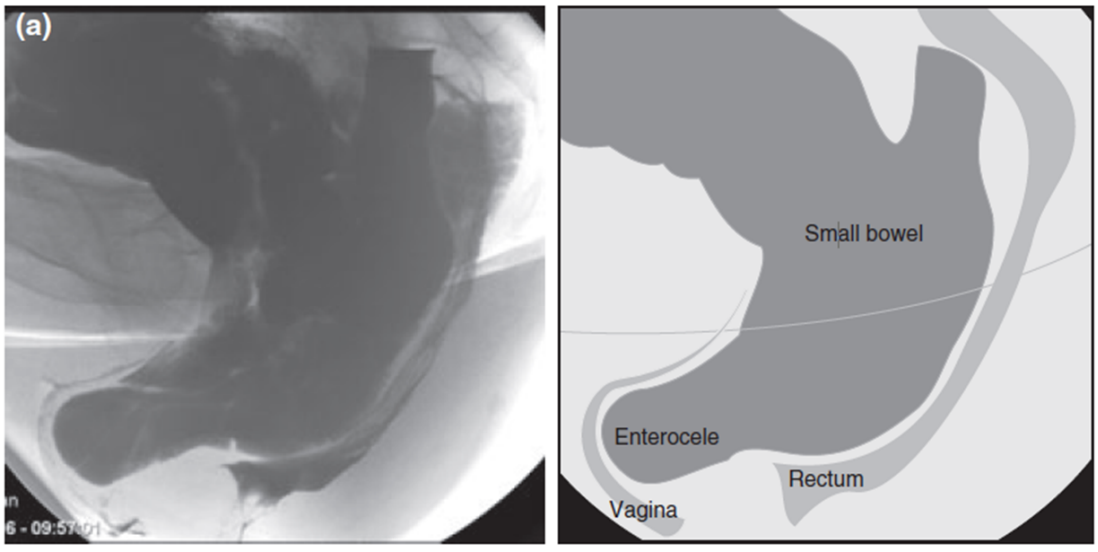

Figure 1.4: Defecation proctography image from Steensma et al. (2010) demonstrating the presence of enterocele.

Figure 1.5: 3D ultrasound image from Dietz et al. (2008) of a levator ani defect resulting from childbirth. The left image is the axial plane of the urogenital hiatus at 36 weeks pregnancy and the right image is of the same women 4 months after childbirth. Note the defect in the PVM on the patient's left.

cially useful for identifying meshes, slings, and implants (Ahmad et al., 2015). Translabial ultrasound, also known as transperineal and introital ultrasound, can show the relationships between the pelvic organs located between the pubic symphysis and the coccyx at rest and under deformation (Wieczorek et al., 2011). Three dimensional (3D) translabial imaging allows the axial plane to be visualized, on which the PVM can be assessed and measured (Fig. 1.5) (Dietz et al., 2005, 2008). Four dimensional (4D) ultrasound can record motion, such as a pelvic floor contraction, in real time allowing LA function to be assessed (Ahmad et al., 2015). Advantages of ultrasound imaging include relatively low cost, a wide range of probe types, a fast frame rate, and good toleration by nearly all patients (Bourcier et al., 2004; Wieczorek et al., 2011). Disadvantages of ultrasound include some operator dependence on interpretation, the possibility of artifacts, and low resolution at lower frequencies (Wieczorek et al., 2011).

1.1.5 Elastic Imaging and Elastography

The use of imaging techniques to measure strain and other mechanical properties of materials is known as strain imaging or elasticity imaging (Gao et al., 1996). Elastography is the field of elastic imaging in which the biomechanical properties of tissue are measured (Gao et al., 1996). This field covers a wide array of techniques using different imaging modalities including ultrasound, X-ray, MRI, and optical tracking to measure an array of local tissue properties including Young's modulus, shear modulus, Poisson's ratio, and viscosity (Gao et al., 1996; Parker et al., 2011). Types of elastography include magnetic resonance elastography (MRE), where the tissue is imaged using MRI, and sonoelasticity, where the tissue is imaged using ultrasound (Gao et al., 1996; Parker et al., 2011).

The most common imaging modality for soft tissue elastography is ultrasound which can provide accurate and precise estimates of strain more quickly and for lower cost than MRE (Wells and Liang, 2011). Early methods of sonoelastography include Doppler velocity measurements to measure velocity of vibration in tissues related to the elastic modulus, image inspection to make relative estimations of stiffness, and cross-correlation techniques (Ophir et al., 1991). The first to use a correlation-based method to measure *in vivo* human tissue motion was Dickinson and Hill (1982), who calculated the correlation coefficient between ultrasonic A-scans to measure liver motion. They found that the correlation coefficient was basically proportional to the size of displacement for very small displacements (Dickinson and Hill, 1982).

Ophir et al. (1991) introduced compression elastography using an external compressive force (Parker et al., 2011). They calculated the cross-correlation between segments from A-scans before and after a compression to find the location at which the correlation was maximum, estimating the shift between the signals in the two segments (Ophir et al., 1991). The strain was calculated by differentiating the displacement field, and the local elastic

modulus was estimated by dividing the pressure of the tissue compression by the strain (Ophir et al., 1991). This method, known as the maximum likelihood strategy, is useful for displacement estimations of varied sizes and can be used for many types of images (Insana et al., 2000).

One issue that lowers the quality of these correlation-based methods is decorrelation of the ultrasonic signal due to displacement and strain (Insana et al., 2000). Image processing before calculating the maximum likelihood, such as warping, can be used to increase coherence between the images and applying compressions incrementally can prevent decorrelation of the ultrasound signal (Insana et al., 2000). The value of the normalized correlation at the maximum likelihood can be considered an indicator of displacement estimation accuracy (Zahiri-Azar and Salcudean, 2006). Another method to improve results is to put the likelihood function into a Bayesian framework to bias the displacement towards a certain size and/or direction (Clocksin et al., 2002; Byram et al., 2013a).

MRE can measure elastic properties in 3D with high accuracy and precision (Parker et al., 2011). It can estimate tissue shear modulus by allowing shear waves to be visualized and their wavelengths estimated (Suga et al., 2003). MRE has many applications including to assess the stiffness of skeletal muscle (Mariappan et al., 2010), but because shear waves of a single frequency must be generated in the imaged muscle with an external stimulator, it would likely be difficult to apply MRE to the pelvic floor muscles due to their location deep within the body. Furthermore, MRI is significantly more expensive than ultrasound and most other imaging modalities, and 3D MRE has a prohibitively long acquisition time (Parker et al., 2011; Mariappan et al., 2010).

The field of strain imaging is not limited to medical applications or to medical imaging modalities. For example, Clocksin et al. (2002) used a Bayesian maximum likelihood method to measure surface strain of antlers and of aluminum alloy using the images of an optical microscope.

1.2 Research Objectives, Hypotheses, and Specific Aims

This dissertation seeks to address the lack of data on the biomechanical properties of the levator ani, particularly at strains less than 10% seen in daily activities by investigating the below central hypotheses (A, B, and C) with the specific aims associated with them listed below each hypothesis.

A. The low strain *in vitro* passive levator ani biomechanical properties can be modeled with a constitutive equation.

   Specific aim 1: Measure passive levator ani biomechanical properties.

   [i.] Perform uniaxial biomechanical testing on cadaveric levator ani samples.

   [ii.] Fit constitutive models from the literature to the stress-strain data to determine which provides the most accurate description of the levator ani behavior at low strains.

B. A correlation-based texture tracking algorithm in volumetric ultrasound images measures regional strain of *ex vivo* muscles accurately compared to strain measured independently by sonomicrometry.

   Specific aim 2: Validate and optimize texture correlation algorithm for calculation of regional muscle strain.

   [i.] Conduct experiments in an *in vitro* model of the pubovisceral muscle using bovine skeletal muscle.

   [ii.] Make independent displacement measurements with a sonomicrometry system for comparison to algorithm displacements and use displacements to compute strain.

   [iii.] Assess statistical significance between algorithm and sonomicrometry using a paired $t-$test.

   [iv.] Optimize algorithm parameters including sub-volume length and correlation argument.

[v.] Compare accuracy of algorithm to levels of decorrelation in the complex ultrasound signals.

[vi.] Compare experimental decorrelation measurements to analytical decorrelation calculations.

C. The *in vivo* stiffness as measured by normalizing the intra-abdominal pressure by level of strain of the pubovisceral muscles is higher in women with diagnosed pelvic floor disorders than in non-sympotmatic women.

Specific aim 3: Measure strain in the pubovisceral muscle *in vivo* in women with and without pelvic floor disorders.

[i.] Apply and measure stress to the pelvic floor *in vivo* with a transvaginal balloon catheter.

[ii.] Record volumetric ultrasound images and pressure levels at controlled stages of balloon expansion.

[iii.] Use images as inputs to the texture correlation algorithm to find displacements in the PVM, and use displacements to calculate strain measurements.

[iv.] Compute strains in several regions of the PVM.

[v.] Calculate a measure of stiffness by dividing the intra-abdominal stress by the strain.

[vi.] Compare the stiffness measurements between different regions of the muscle with paired $t-$tests and between the two groups (women with and without diagnosed pelvic floor disorders) using an unpaired $t-$test.

Although there is some literature focused on the passive biomechanics of the cadaveric LA, previous studies have focused on larger strains. In Specific Aim 1, we performed biomechanical tests of cadaveric tissue at low strains. There have been a number of studies investigating deformation of the PVM using ultrasound imaging, but all measurements of strain

were for large deformations (maximum contraction and maximum Valsalva) and measured strain for the PVM as a whole rather than on a regional basis. We propose using techniques from the field of strain imaging to measure regional strain in the PVM. In Specific Aim 2, we developed a correlation-based, maximum likelihood texture tracking algorithm and validated it in an *ex vivo* model of the PVM. We also investigated the relationship between the size of displacement, echo decorrelation, and accuracy of the texture tracking algorithm. In Specific Aim 3, we developed a protocol to obtain 3D ultrasound images of the PVM under incremental deformations while measuring intra-abdominal pressure. By applying the texture tracking algorithm from Specific Aim 2 to these images from Specific Aim 3, we were able to measure strain in the PVM and calculate an estimation of the stiffness that could be compared between different individuals. We compared the results of Specific Aim 1 to Specific Aim 3 to identify differences between the *ex vivo* and *in vivo* mechanical properties.

1.3 Thesis Organization

This dissertation has a total of five chapters including this introduction (Chapter 1). Chapter 2 focuses on Hypothesis A, in which the passive biomechanical properties of the levator ani were measured. Chapter 3 concentrates on Hypothesis B where an *ex vivo* model of the pubovisceral muscle was used to validate a correlation-based texture tracking algorithm. Chapter 4 makes progress towards Hypothesis C by developing a method to measure the *in vivo* biomechanical properties. The final chapter summarizes the entire series of studies, discusses its limitations and future directions, and highlights applications of this research to other clinical problems.

Chapter II

Passive Biomechanical Properties of Human Cadaveric Levator Ani Muscle at Low Strains

2.1 Introduction

Pelvic floor disorders (PFD), including incontinence and pelvic organ prolapse, are described as a hidden epidemic affecting 37% of the adult female population (DeLancey, 2005; Lawrence et al., 2008). It is believed that PFD develop from damage and weakening of the pelvic floor support structures, particularly the levator ani (LA) muscle, often from childbirth and the aging process (Ashton-Miller and DeLancey, 2009). Biomechanical differences even at small strains in the LA have been shown to correlate with prolapse (Thyer et al., 2008).

A number of teams have constructed finite element models (FEM) of the LA during birth (Li et al., 2010a; Jing et al., 2012; Lien et al., 2004; Parente et al., 2008). Chen et al. (2006) and Chen et al. (2009a) created a model of pelvic organ prolapse that highlighted the importance of both the PVM biomechanics as well as ligament support structures. One factor limiting such studies is the lack of a suitable constitutive model of the LA. Until 2010, these studies used biomechanical parameters based on the passive properties of other muscles (Li et al., 2010b). More recently, some groups have used parameters obtained through *in*

vitro mechanical testing of LA by Jing (2010), but have noted that their choice of constitutive model was based on ease of implementation in ABAQUS rather than best approximating the LA's properties accurately (Jing, 2010; Li et al., 2010b). Janda (2006) performed uniaxial and biaxial mechanical testing of human LA samples; however, the donors had been deceased less than a day before the testing and thus the stress-strain measurements in the fiber direction was likely to be affected by rigor mortis. Jing (2010) performed uniaxial and biaxial mechanical testing of human LA samples to derive constitutive parameters for the muscle. He noted that the chosen neo-Hookean model did not satisfactorily model the tissue at low stresses. Li et al. (2010a) used data from Jing (2010) with both linear and exponential models to represent two extreme cases for extrapolation of large deformation. While large strains are seen during childbirth, FEM for other pelvic floor functions will require a model suitable for smaller strains.

The aim of this study was to measure the passive biomechanical properties of the LA in the fiber direction and to find a constitutive model reflecting these properties at low strains, because the properties at low strains may be of high importance to understand the mechanics of incontinence and prolapse. It is assumed that the LA has its highest stress component in the fiber direction, as has been shown for the diaphragm (Margulies et al., 1994). Biomechanical properties of the LA in the fiber direction are the most important contributor to the magnitude and location of the principal muscle stretch (Li et al., 2011). It is important to quantify LA biomechanical properties at the moderate deformation rates seen *in vivo* in daily life, such as the 0.5–2 mm/s deformation rates observed during voluntary pelvic floor contractions (Constantinou and Omata, 2007).

Here, five constitutive models were fit to measured stress-strain curves for cadaveric LA specimens. The models investigated were a linear model and an exponential model based on the strain energy models used to describe the LA by Li et al. (2010b), a hybrid linear-exponential model used to describe collagen by Fung (1993), a combined linear-exponential

model (Eq. 2.9) proposed by (Holzapfel et al., 2001) based on the model used to describe the LA by Jing et al. (2012), and a power-law model (Eq. 2.10) based on the low-strain portion of the model proposed by Sokolis et al. (2002) to describe small strains in aortic tissue. The power-law model proposed by Sokolis et al. (2002) most accurately described LA properties. These data may be useful for future FEM of the pelvic floor in the context of PFD and for comparison to image-based measurements of *in vivo* LA biomechanics (Nagle et al., 2013; Thyer et al., 2008).

2.2 Methods

Nine fresh-frozen post-menopausal female cadavers were obtained for dissection and biomechanical analysis from the University of Cincinnati Body Donation program. The cadavers had been thawed for three days, so rigor mortis was no longer active (Van Ee et al., 2000; Goff, 2009). Institutional Review Board (IRB) protocol approval was not required because no identifying information of the donors was disclosed. A list of the ages, causes of death, and number of harvested samples successfully analyzed for each of the nine cadavers is shown in Table 2.1. No other data were available about the health history of the cadavers due to privacy concerns.

A midline or Pfannenstiel incision was made on the skin of the cadavers and carried down to the fascia. The retropubic space was entered by moving the bladder and urethra downward off the pubic bone. Paravaginal defects were created and fat was dissected off the vagina and pelvic sidewalls to expose the arcus tendineus levator ani (ATLA). Muscle fibers were identified medial to the ATLA, lateral to the vaginal walls, anterior to the ischial spines, and posterior to the pubic ramus. These muscle fibers typically ran parallel with the vaginal wall toward the coccyx. A segment of muscle fiber consistent with the ileococcygeus location as seen in Fig. 1.2 was excised bilaterally in cadavers whenever possible, however in

Table 2.1: Ages and causes of death for the cadavers providing levator ani specimens analyzed in this study. The # samples indicates the number of samples from each cadaver that was used in the results.

Cadaver #	Age (years)	Cause of death	# samples
1	54	Breast cancer	0
2	64	Renal carcinoma	1
3	77	Metastatic lung cancer	1
4	80	Congestive heart failure	2
5	81	Pneumonia	1
6	91	Pneumonia, gastroenteritis	2
7	91	Myocardial infarction	1
8	92	Cerebrovascular disease, atrial fibrillation	0
9	96	Congestive heart failure, coronary artery disease	1

some cases, the muscle was too atrophied on one side to extract. The muscle then was cut with an ASTM-D-638-5-IMP dog-bone shaped die (Fig. 2.1) in the direction of the fibers, resulting in a 1 inch by 1/8 inch gauge segment. This provided 14 total segments of LA for biomechanical testing, with 1–2 segments from each cadaver.

LA segments were soaked in saline and wrapped in gauze for transport to the testing facility, where mechanical testing was performed at room temperature (22 °C) within four hours of extraction. The samples were mounted in a single-column mechanical test system (100R, TestResources, Shakopee, MN) system using waveform grips designed for soft tissues (Fig. 2.1).

The tissue samples' width and thickness in the unloaded state were measured by digital caliper. Due to a non-uniform cross section, width and thickness were measured at three points along the length and an average taken to provide the cross-sectional area used in

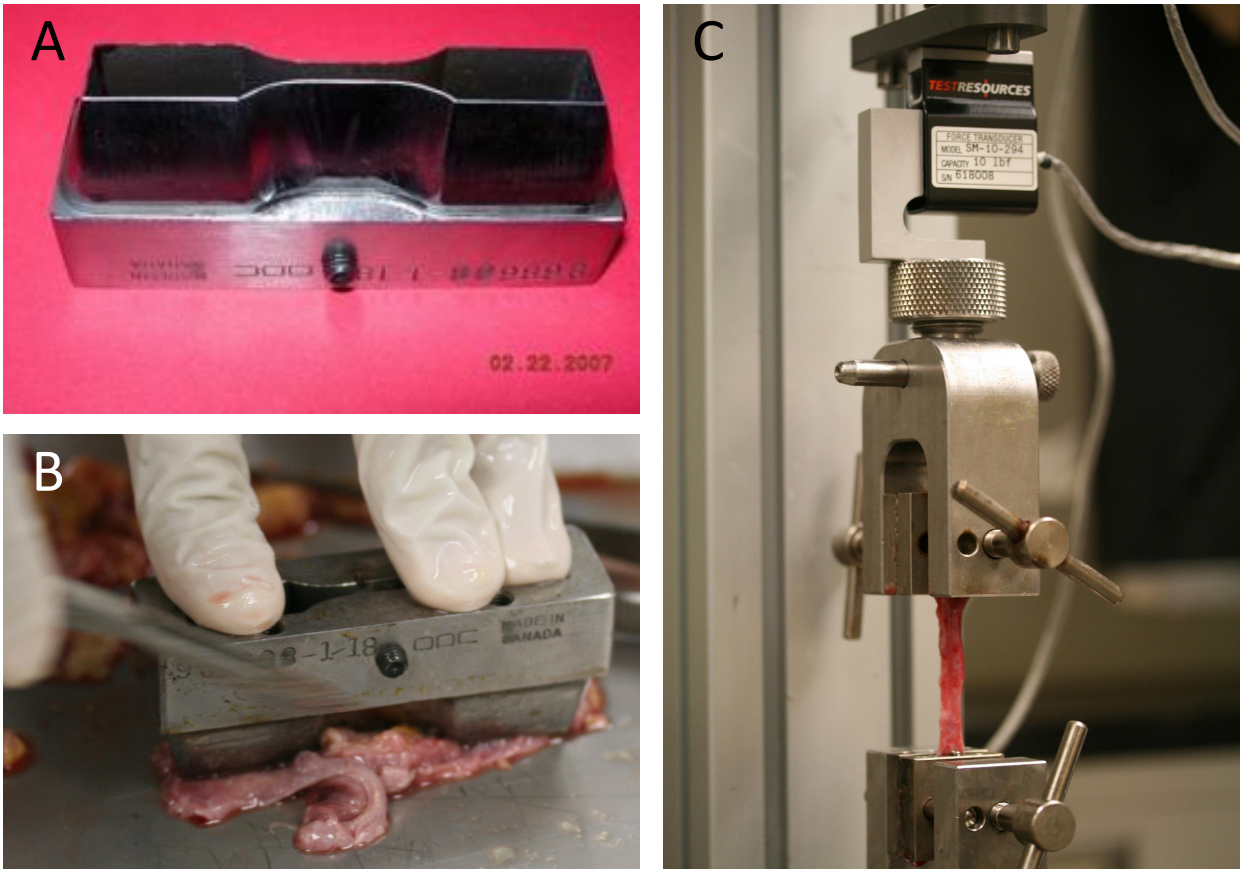

Figure 2.1: Equipment used in mechanical testing. (A) D-638-5-IMP die used in this study. Its total length is 63.5 mm and the middle section is 25.4 mm by 3.175 mm. (B) Die in use with a scalpel to cut a levator sample. (C) LA specimen in waveform grips during mechanical testing.

later calculations. The initial gauge length of the sample was measured by digital caliper as the distance along the tissue between the grips (Fig. 2.1 C). Load was measured by a 44.48 N load cell (E32593, TestResources) with 0.01 N precision. Each sample underwent preconditioning followed by monotonic uniaxial extension to failure at a deformation rate of 1 mm/s (Figs. 2.2 and 2.3). Preconditioning consisted of 10 cycles of sinusoidal stretch with amplitude 2.54 mm (10% of the expected gauge length). Load and position data were recorded at a sampling rate of 30 Hz. Between preconditioning and uniaxial extension, the muscle was allowed to rest briefly, with the load remaining below 0.01 N for at least 1.9 s in

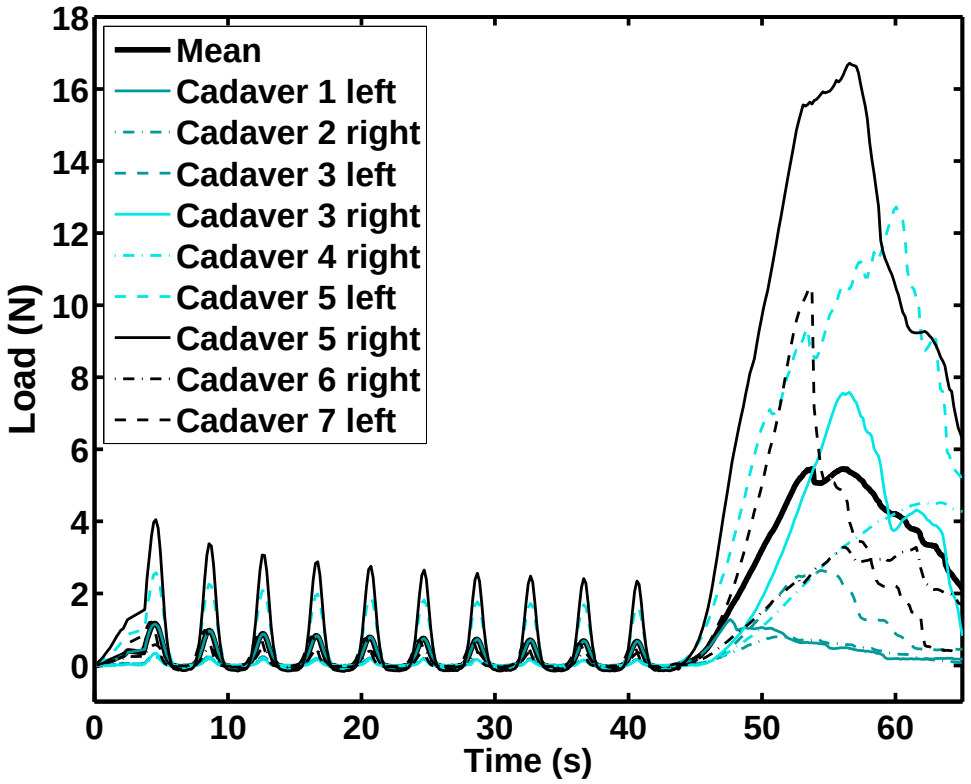

Figure 2.2: Load vs. time graph for all data sets over the entire mechanical testing protocol. The bold line indicates their average.

all cases.

Data measured after preconditioning during the failure test were used to calculate the stretch ratio λ (current length/original length), the non-linear Green-St. Venant strain $E = (\lambda^2 - 1)/2$ (Sokolis et al., 2002), and the true stress σ (force/original area $\times\lambda$) (Boresi et al., 2010). Stress data were smoothed with an 11 point moving average. Data were truncated after $E = 0.10$, corresponding to the strain range of the preconditioning, before constitutive models were fit to the data.

The yield strain E_{y}, corresponding to the first sign of tissue failure, was determined from the stress-strain plot for the uniaxial extension test of each sample. E_{y} was defined as the strain at the earliest decrease of slope in the stress-strain curve. For all samples analyzed,

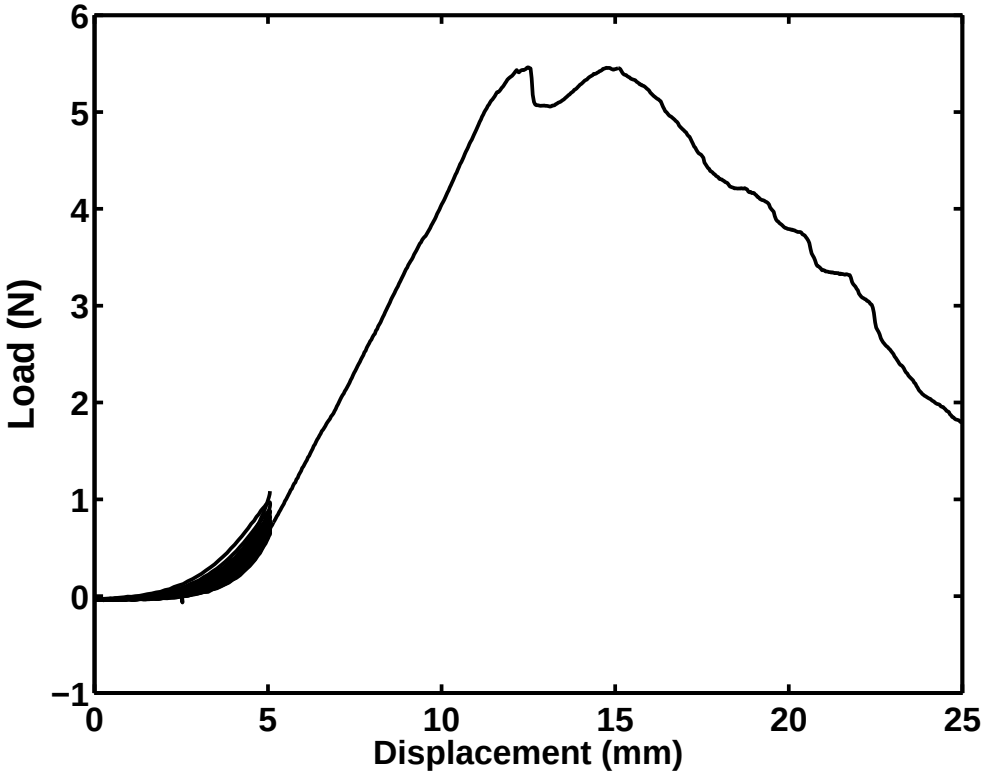

Figure 2.3: Load vs. displacement graph for the average of all nine data sets from the beginning of the first full cycle of pre-conditioning to the end of the uniaxial extension.

the yield strain was greater than $E = 0.10$.

The LA was assumed to be transversely isotropic about the fiber direction, hyperelastic, and incompressible (Fung, 1993). The effects of viscoelasticity and temperature were not modeled, but are not expected to significantly change results, as will be addressed in the Discussion section of this chapter. An incompressible material undergoing uniaxial extension has the deformation gradient

$$F = \begin{bmatrix} \lambda & 0 & 0 \\ 0 & \frac{1}{\sqrt{\lambda}} & 0 \\ 0 & 0 & \frac{1}{\sqrt{\lambda}} \end{bmatrix}, \tag{2.1}$$

which describes the state of strain in all directions. The right Cauchy strain tensor is

$$C = F^T F = \begin{bmatrix} \lambda^2 & 0 & 0 \\ 0 & \frac{1}{\lambda} & 0 \\ 0 & 0 & \frac{1}{\lambda} \end{bmatrix}. \tag{2.2}$$

The first invariant of the strain tensor is

$$I_1 = \text{trace}(C) = \lambda^2 + \frac{2}{\lambda}. \tag{2.3}$$

Note that when there is no strain, $\lambda = 1$ and $I_1 = 3$ (Boresi et al., 2010; Holzapfel, 2000).

Five models were fit using a least-squares Nelder-Mead minimization method in MATLAB (Mathworks, Natick, MA, USA) to the test data to identify constitutive parameters. The first constitutive model tested fit to the data was a linear model based on one of the strain energy models used by Li et al. (2010b). The strain energy function of this model is

$$W = C(I_1 - 3), \tag{2.4}$$

where C is analogous to the elastic modulus and has units of stress. When differentiated with respect to λ, the stress strain relationship is written as

$$\sigma = 2C\left(\lambda - \frac{1}{\lambda^2}\right). \tag{2.5}$$

The second constitutive model was an exponential model also based on a strain energy model used by Li et al. (2010b):

$$W = B_1(e^{B_2(I_1-3)} - 1), \tag{2.6}$$

where B_1 is a parameter with units of stress and B_2 is a dimensionless parameter of nonlinearity. When differentiated with respect to λ, this becomes

$$\sigma = 2B_1B_2e^{B_2(\lambda^2+\frac{2}{\lambda}-3)}\left(\lambda - \frac{1}{\lambda^2}\right). \tag{2.7}$$

The third constitutive model was a hybrid of the first two models used by Fung (1993) consisting of Eq. 2.7 for $\lambda \leq \lambda_T$ and Eq. 2.5 for $\lambda \geq \lambda_T$ where λ_T is the end toe stretch. For the hybrid linear-exponential model, the initial guess for the end toe stretch chosen was $\lambda_T = 1.05$ and the actual λ_T was determined through error minimization to preserve continuity of the slope of the fitted curve.

The fourth constitutive model was a combined linear-exponential model proposed by Holzapfel et al. (2001) based on the model used by Jing et al. (2012) with strain energy

$$W = C(I_1 - 3) + \frac{k_1}{2k_2}[e^{(\lambda^2-1)^2}], \tag{2.8}$$

where the first term represents the mechanics of the isotropic ground substance with a modulus of C with units of pressure and the second term represents the contribution of the

muscle fibers with k_1 having units of pressure and k_2 being dimensionless. Differentiated with respect to λ, this becomes

$$\sigma = C\left(2\lambda - \frac{2}{\lambda^2}\right) + 2k_1\lambda e^{k_2(\lambda^2-1)^2(\lambda^2-1)}. \tag{2.9}$$

The final constitutive model was a power-law model based on the low-strain portion of the model proposed by Sokolis et al. (2002). In this case, the model was not expressed in a strain energy form, but rather was presented in the stress-strain form

$$\sigma = (k(1-q)E)^{\frac{1}{1-q}}, \tag{2.10}$$

where k has units of stress and q is a unitless measure of non-linearity.

To compare goodness of fit, a normalized root-mean-square (RMS) error was calculated for each stress-strain data set, defined as the RMS stress error divided by the mean stress.

The preconditioning data were used to determine which samples to include in the final analysis. Samples were excluded if grip slippage was detected by appreciable discontinuities in the preconditioning load data. In addition, to verify that all samples analyzed had been adequately preconditioned, each loading cycle during the preconditioning was separately fit to the power-law model and samples were excluded if the parameters k and q varied by more than 10% within the last three cycles. Three specimens were excluded due to grip slippage and two were excluded because of failure to fully precondition, leaving nine specimens from seven of the original nine cadavers. Of the samples where grip slippage was detected, the parameters k and q were found to vary more than 10% as well. Examples of preconditioning data can be seen in Fig. 2.4.

Pearson's linear correlation coefficient was calculated between cadaver age and parameters k and q to test the null hypothesis that the parameters do not correlate with age.

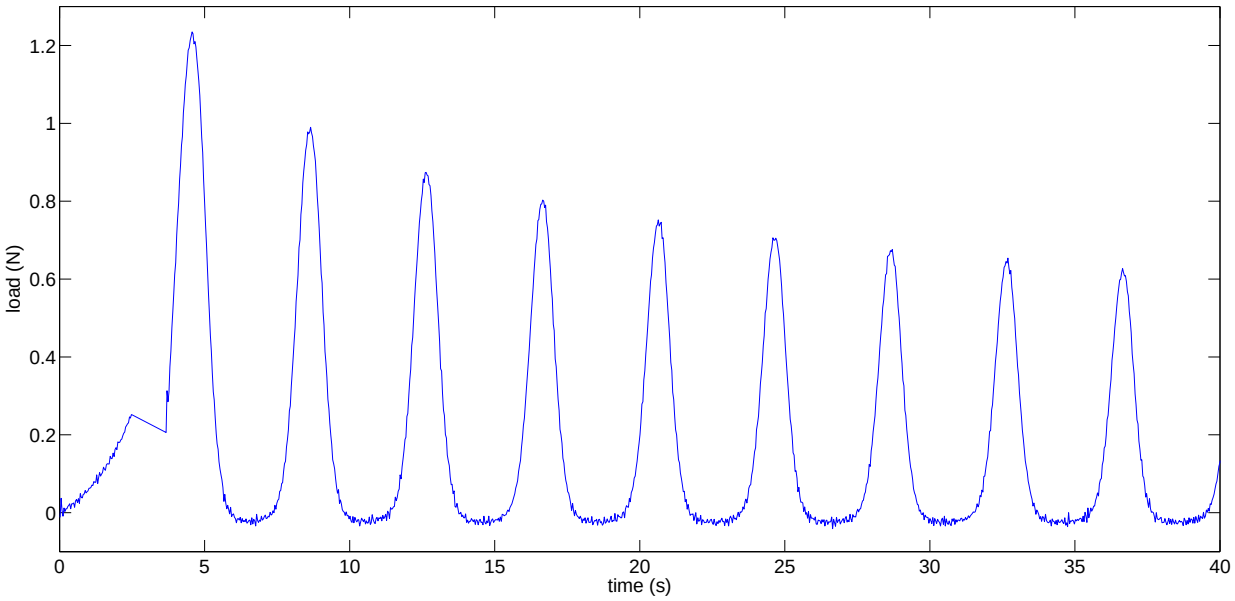

(a)

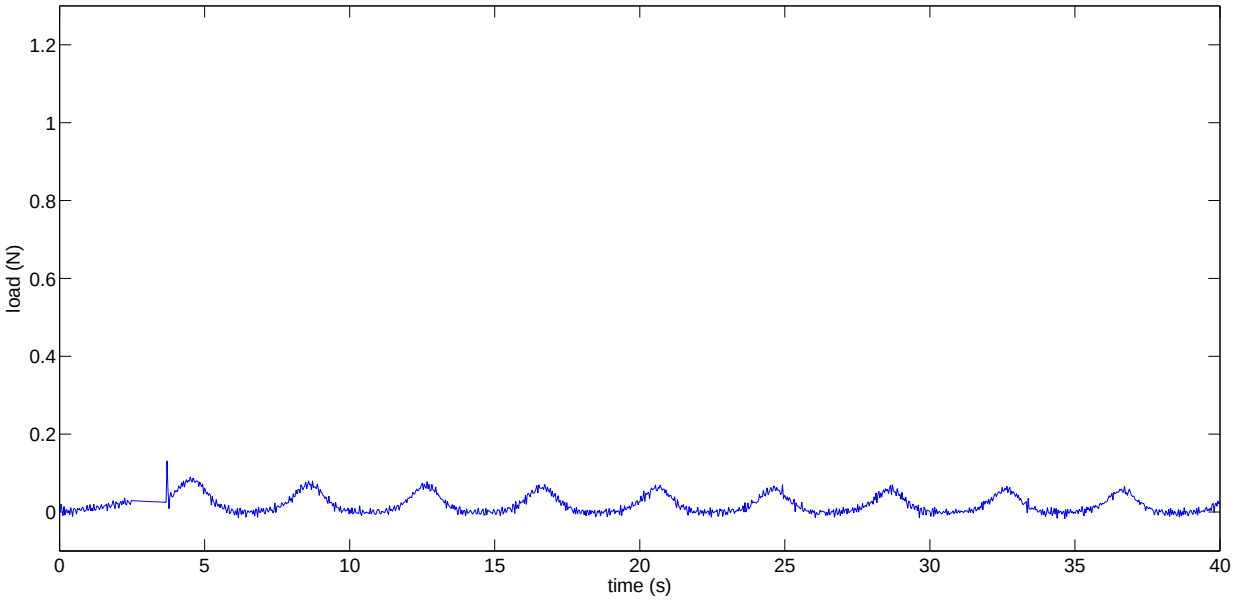

(b)

Figure 2.4: Preconditioning for two samples from cadaver 9. In (a), the preconditioning worked correctly with no sign of slippage and with the last three cycles having power-law parameters k and q vary less than 10%. In (b), there is evidence that the grips were not tight enough, because there is a large discontinuity at the beginning of the first cycle indicating slippage and the parameters fit to the last three cycles varied by more than 10%.

To test the usefulness of the power-law model for higher strains, models fit using data truncated at $E = 0.10$ were extrapolated to higher strains and normalized RMS errors were calculated. The strain at which the error exceeded 10% was considered the maximum strain measurable by this model, $E_{\max}$. $E_{\max}$ was compared to the observed E_{y} as defined above.

2.3 Results

The mean width, thickness, and initial length of the nine specimens analyzed were 3.00 ± 0.80, 7.55 ± 1.16, and 39.58 ± 10.51 mm (Table 2.2). The mean and standard deviation of the normalized RMS error between measured and modeled stress were 0.349 ± 0.074 for the linear model (Eq. 2.5), 0.080 ± 0.025 for the exponential model (Eq. 2.7), 0.035 ± 0.017 for the hybrid linear-exponential model (Eqs. 2.7 and 2.5), 0.083 ± 0.017 for the combined linear-exponential model (Eq. 2.9), and 0.024 ± 0.010 for the power-law model (Eq. 2.10). Plots of each model fit to the stress-strain curve of the specimens can be seen in Figs. 2.5–2.9. The mean and standard deviation of the fit parameters were $C = 0.144 \pm 0.105$ MPa for the linear model, $B_1 = 0.0042 \pm 0.0023$ MPa, $B_2 = 23.53 \pm 7.98$ for the exponential model, $C = 1.42 \pm 1.10$ MPa, $\lambda_{toe} = 1.05 \pm 0.01$, $B_1 = 0.00045 \pm 0.00034$ MPa, $B_2 = 103.4 \pm 13.1$ for the hybrid linear-exponential model, $C = 9.05 \times 10^{-10} \pm 1.59 \times 10^{-9}$ MPa, $k_1 = 0.1078 \pm 0.079$ MPa, $k_2 = 16.6 \pm 5.94$ for the combined linear-exponential model, and $k = 4.69 \pm 2.81 MPa$ and $q = 0.44 \pm 0.08$ for the power-law model. For all models, the fitted parameters did not change to a large degree if a different initial guess was used except for parameter B_1 from the exponential model and parameters C and k_2 from the combined linear-exponential model.

The power-law parameters k and q fit to each of the nine stress-strain curves are listed in Table 2. The stress-strain curves from each trial, power-law fits to each measurement, and a stress-strain curve based on the average parameters are shown in Figure 2.9. Correlation coefficients between the fit power-law parameters and donor age were not statistically

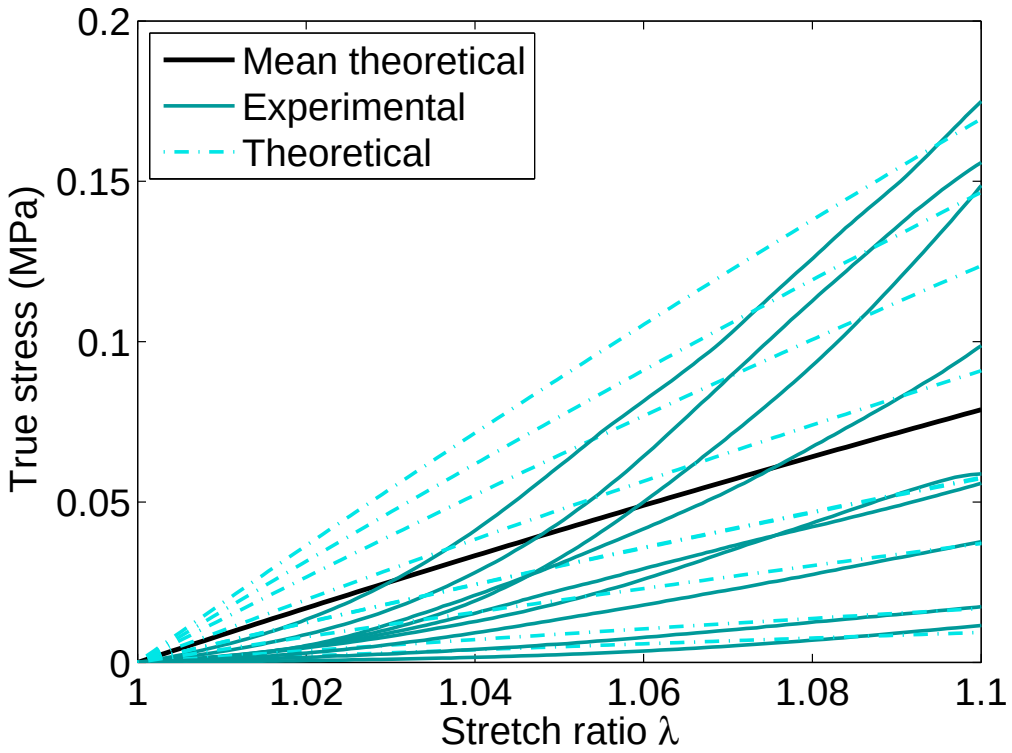

Figure 2.5: Stress-strain measurements from the end of pre-conditioning until $E = 0.10$. The solid blue lines are the experimental data and the dashed cyan line the fitted curve based on the linear model (Eqn 2.5). The bold black line is the stress-strain curve for the average fit parameter $C = 0.144$ MPa.

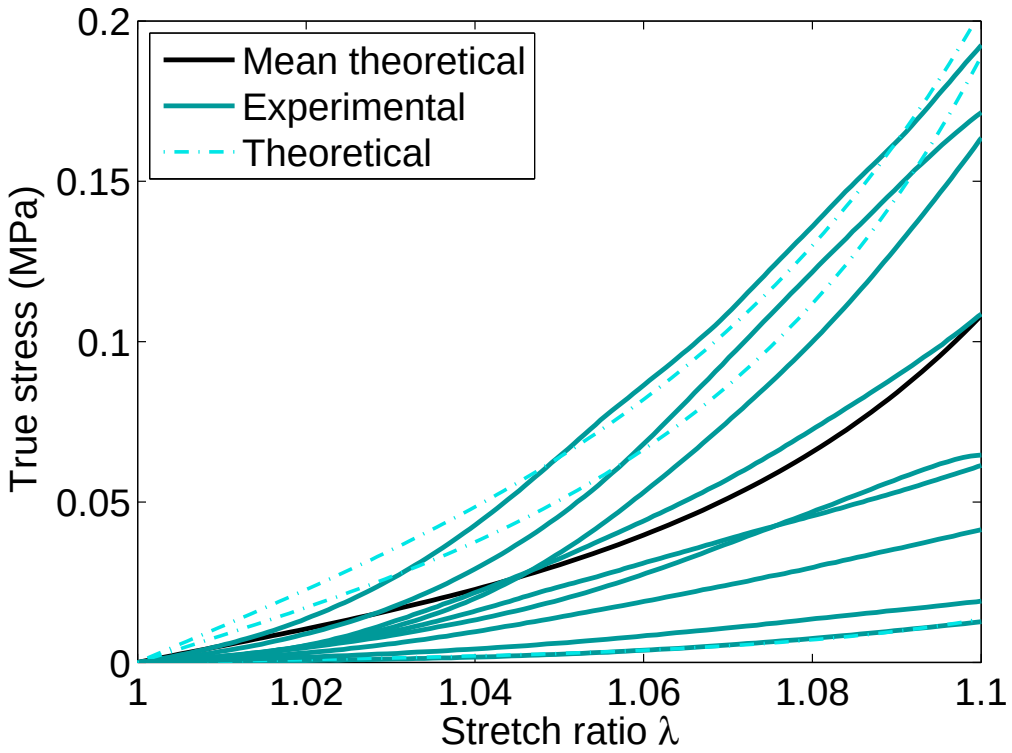

Figure 2.6: Stress-strain measurements from the end of pre-conditioning until $E = 0.10$. The solid blue lines are the experimental data and the dashed cyan line the fitted curve based on the exponential model (Eqn 2.7). The bold black line is the stress-strain curve for the average fit parameters $B_1 = 0.0042$ MPa and $B_2 = 23.53$.

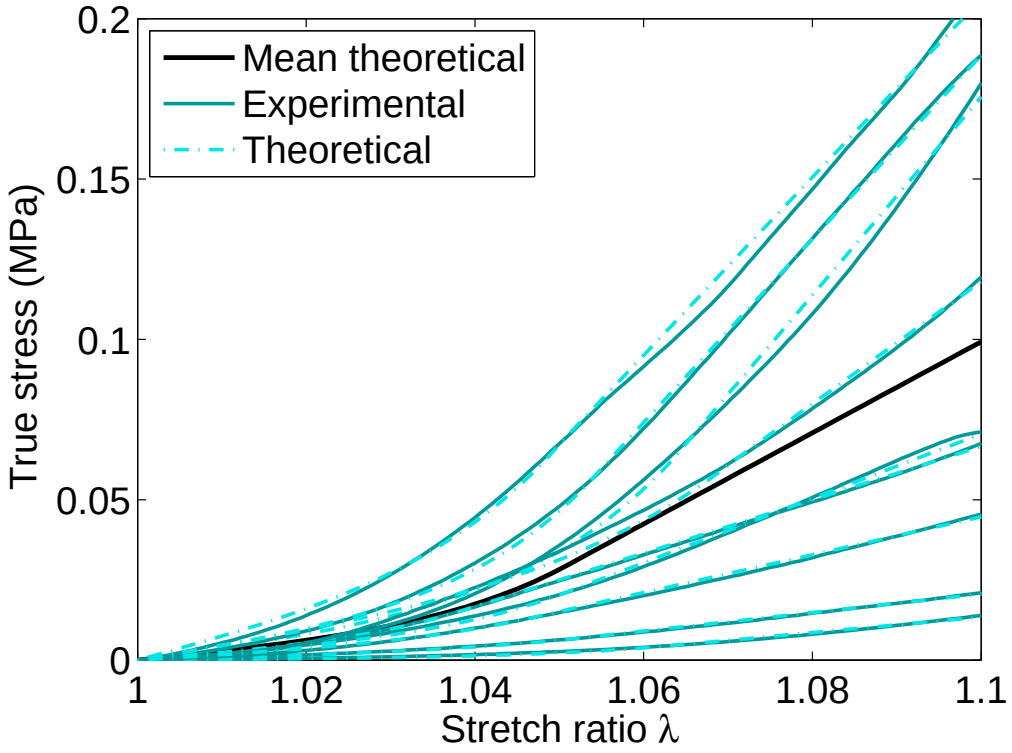

Figure 2.7: Stress-strain measurements from the end of pre-conditioning until $E = 0.10$. The solid blue lines are the experimental data and the dashed cyan line the fitted curve based on the hybrid linear-exponential model (Eq. 2.7 for $\lambda \leq \lambda_T$ and Eq. 2.5 for $\lambda \geq \lambda_T$ where λ_T is the end toe stretch). The bold black line is the stress-strain curve for the average fit parameters $C = 1.42$ MPa, $B_1 = 0.00045$ MPa, and $B_2 = 103.41$.

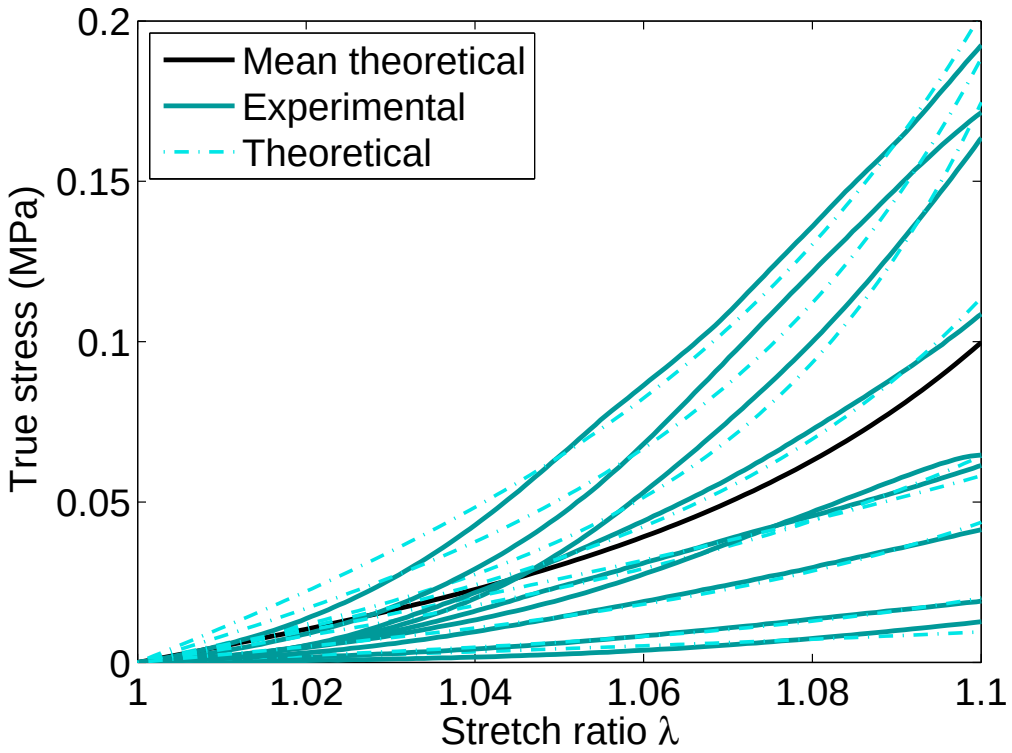

Figure 2.8: Stress-strain measurements from the end of pre-conditioning until $E = 0.10$. The solid blue lines are the experimental data and the dashed cyan line the fitted curve based on the combination linear-exponential model (Eqn 2.9). The bold black line is the stress-strain curve for the average fit parameters $C = 9.05 \times 10^{-11}$ MPa, $k_1 = 0.108$ MPa, and $k_2 = 16.6$.

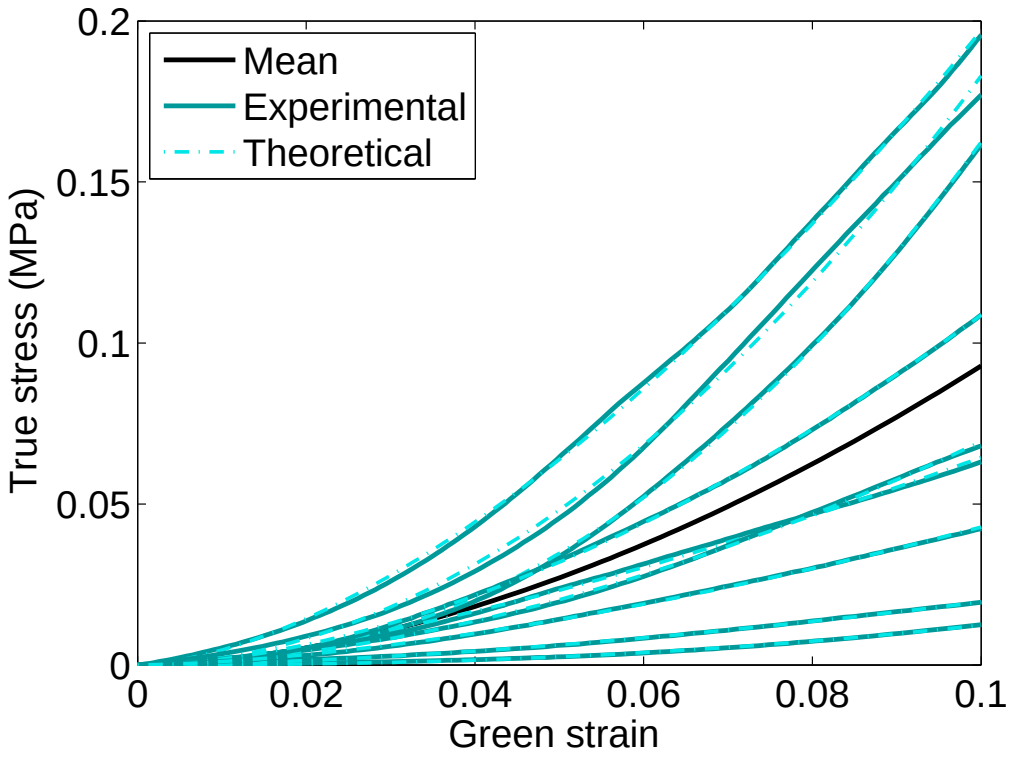

Figure 2.9: Stress-strain measurements from the end of pre-conditioning until $E = 0.10$. The solid blue lines are the experimental data and the dashed cyan lines the fitted curve based on the power-law mode (Eqn. 2.10). The bold black line is the stress-strain curve for the average fit parameters $k = 4.68$ MPa and $q = 0.44$.

Table 2.2: Specimen dimensions and power-law fit parameters with the mean and standard deviation (st. dev.) for each quantity. Specimens are identified by cadaver number (corresponding to those in Table 2.1) and the side from which the specimen was extracted. The normalized RMS error for each fit is the root-mean-square difference between measured and fit stress divided by the mean stress. The yield strain E_{y} is the strain at which the slope of the stress-strain curve began to decrease. The strain up to which the power-law model using the listed parameters can be extrapolated with acceptable error is $E_{\max}$.

Cadaver number	Side	Width (mm)	Thickness (mm)	Length (mm)	k (MPa)	q	Normalized RMS error	E_{y}	$E_{\max}$
2	left	8.54	2.18	33.59	4.13	0.45	2.13×10^{-2}	0.10	0.11
3	right	5.67	2.65	24.72	1.52	0.39	2.42×10^{-2}	0.18	0.14
4	left	7.54	4.20	29.26	3.34	0.56	3.82×10^{-2}	0.13	0.11
4	right	6.62	2.39	42.72	5.03	0.43	1.20×10^{-2}	0.18	0.16
5	right	6.47	2.72	34.25	2.25	0.38	1.58×10^{-2}	0.20	0.17
6	left	9.24	2.92	48.69	6.12	0.40	1.64×10^{-2}	0.20	0.16
6	right	8.37	4.26	37.99	8.35	0.50	3.30×10^{-2}	0.19	0.19
7	right	7.22	3.44	58.12	2.29	0.32	3.41×10^{-2}	0.32	0.29
9	left	8.30	2.20	46.85	10.00	0.56	1.71×10^{-2}	0.29	0.27
Mean		7.55	3.00	39.58	4.78	0.44	$2.36 * 10^{-2}$	0.20	0.18
st. dev.		1.16	0.80	10.51	2.91	0.08	$9.40 * 10^{-3}$	0.07	0.06

significant for k ($r = 0.57,\ p = 0.11$) or q ($r = 0.08,\ p = 0.84$).

On average among the 9 specimens analyzed, the power-law model with parameters k and q fit to data for $E \leq 0.10$ could be extrapolated to a strain $E_{max} = 0.18 \pm 0.07$, an average 92% of the yield strain E_{y}, for a normalized RMS error of 10%. Table 2 lists $E_{\max}$ and E_{y} for each sample.

2.4 Discussion

The power-law constitutive model (Eq. 2.9) provided a more accurate fit than other models utilized in the literature. The hybrid linear-exponential model was close in accuracy, but was more cumbersome to implement as it contained a total of four parameters to fit (C, B_1, B_2, and λ_T) compared to just two parameters (k and q) for the power-law model. We suggest that the power-law model is appropriate for future FEM of the LA at low strains relevant to mechanisms of PFD, particularly in the daily life of post-menopausal women. As this model only requires two parameters, this model should have higher mathematical stability than alternative constitutive models with more material parameters.

The parameter k was somewhat variable among the nine samples analyzed (coefficient of variation 61%), while the parameter q was less variable (coefficient of variation 19%). Sources of variation include different birth and health histories of the donors, as well as possible variation in post-mortem handling of the cadavers.

Donor age was not significantly correlated with the parameters k and q. This is expected, because all of the cadavers were post-menopausal. It has been shown that while menopausal status is a significant predictor of PFD, age is usually not a significant predictor when normalized for confounding factors such as obesity and parity (Lawrence et al., 2008). The modest positive correlation between age and k may be related to the stiffening of collagen fibers with age (Gao et al., 2008).

The data measured here do not fully replicate the *in vivo* stress-strain response, because specimens were tested at room temperature rather than body temperature and only passive properties were measured. Based on previous skeletal-muscle measurements, the passive stiffness at 40 °C is likely to be 85-90% of that at 25 °C (Noonan et al., 1993). It is important to understand the passive biomechanics as an initial step to modeling the LA. Since PFD can be caused by loss of muscle activation (Ashton-Miller and DeLancey, 2007),

an understanding of the passive biomechanical properties of the LA is significant. When comparing to *in vivo* biomechanical measurements, measured passive parameters may also be used to estimate the contribution of active effects to the muscle's properties. Based on previous measurements, the active stiffness is likely 50-60% of the passive stiffness (Noonan et al., 1993).

The deformation rate of 1 mm/s represents a strain rate of approximately 4% s^{-1}. This rate is clinically relevant, being similar to the deformation rate in a voluntary pelvic floor contraction (Constantinou and Omata, 2007). This rate is also sufficiently small to characterize rate-independent properties of the levator. Slower deformation rates have been shown to lower measured stiffness only slightly (Taylor et al., 1990). Fung (1994) has shown that preconditioned biological materials have largely repeatable stress-strain responses that are not very sensitive to strain rate.

Li et al. (2010a) set the exponential parameter B_2 to 0.5 and fit Eq. 2.7 to data obtained by Jing (2010) to obtain an optimum value of $B_1 = 0.0221$ MPa. These are both quite different than the mean parameters in this study of $B_2 = 29.6$ and $B_1 = 0.0029$. $B_2 = 0.5$ was chosen because a highly non-linear model was desired, not because it would provide the fit. The best fit of the linear model was $C = 0.0161$ MPa, which is significantly smaller than the $C = 0.144$ MPa found in this study. The LA samples in Jing (2010) were also from fresh cadavers of elderly women, so the large difference in parameters is likely do to the difference in the range of strains covered as they covered strains up to 0.8.

For more accurate FEM of the pelvic floor, further data are needed to fully understand the stress-strain properties of the LA. Future studies are needed to examine the mechanical response of the LA at higher strains, in the non-fiber direction, the influence of muscle activation, and its viscoelastic properties. However, as a starting point, the data reported here is useful in quantifying its passive biomechanical properties at low strains and strain rates in the fiber direction.

Chapter III

Validation and Optimization of Three-Dimensional Strain Tracking by Volumetric Ultrasound Image Correlation in a Pubovisceral Muscle Model

3.1 Introduction

In the United States, 300,000-400,000 women undergo surgery for pelvic floor disorders (PFD) annually (DeLancey, 2005). Despite the high prevalence of PFD, little is known about the biomechanical changes, typically related to childbirth injury and aging, that lead to these disorders (Ashton-Miller and DeLancey, 2009). The levator ani (LA) is a critical source of support to the pelvic organs. Damage to the LA, most commonly in its pubovisceral portion, is correlated to stress urinary incontinence (DeLancey et al., 2003) and defects in the LA are also associated with pelvic organ prolapse, though in some cases prolapse patients have no visible defect on MRI (DeLancey et al., 2007). Accurate measurement of deformation in the LA is the first step to estimating its biomechanical properties, but few have tracked LA motion *in situ* until recently (Thyer et al., 2008; Derpapas et al., 2012; Siafarikas et al., 2015). Measurement of the *in vivo* biomechanics of the pubovisceral muscle (PVM) has many potential applications including early detection of conditions likely to lead to stress

urinary incontinence or pelvic organ prolapse (Ashton-Miller and DeLancey, 2009), inputs to finite element models of the pelvic floor, and surgical planning.

Ultrasound imaging has been widely used with correlation techniques to measure regional displacement and strain in soft tissues (Parker et al., 2011). Early efforts used correlation between one-dimensional ultrasound A-scans to measure displacements in the direction of the ultrasound transducer (Dickinson and Hill, 1982). These techniques were later extended to two and then three dimensions under many different types of deformation (Wells and Liang, 2011).

Some groups have improved the accuracy and speed of correlation-based displacement estimates in ultrasound images by using a biased displacement estimator (Chen et al., 2009b), where a cross-correlation likelihood was combined with a prior function based on displacements already measured. Clocksin et al. (2002) combined an exponential sum likelihood with a prior which biased the argument towards small displacements. This was used by Nageswaran (2008) to measure 2D displacement and strain in soft tissues using both ultrasound and MRI images. Such Bayesian speckle tracking algorithms can combine other types of prior and likelihood functions to improve accuracy and computational costs (Byram et al., 2013b).

This chapter investigates the use of a texture correlation algorithm based on a likelihood function proposed by Clocksin et al. (2002) to track regional deformation and strain in three dimensional (3D) B-mode ultrasound images of an *ex vivo* PVM model and compares its accuracy to the more commonly used Pearson correlation coefficient. This was done both with and without a prior term that biases the algorithm towards small displacements. The goals of this study were to validate this algorithm in a PVM model and to determine its optimum parameters for best accuracy. It also investigates how increasing amounts of displacement and strain affect decorrelation of the echo signal and accuracy of the texture tracking algorithm. This algorithm may then be used in future *in vivo* experiments to

measure strain in the PVM in order to estimate its biomechanical properties, as will be seen in the next chapter.

3.2 Materials and Methods

3.2.1 Pubovisceral Muscle Model

To measure strains in a range of magnitudes and directions consistent with the PVM *in vivo*, a model was created using bovine skeletal muscle as shown in Fig. 3.3 (Nagle et al., 2013; Hooi et al., 2015). The muscle was cut along the fiber direction to achieve size and geometry similar to previous PVM measurements, in which the axial diameter was 7.3 ± 1.6 mm and the coronal diameter was 13.3 ± 5.5 mm in 38 women (Dietz et al., 2005). The ends of the muscle segment were clamped to the edges of a 1% saline-filled tank so that they would remain stationary. A soft, hemispherical indenter was positioned above the middle of the muscle and was attached to a stepping positioner system (Velmex, Bloomfield, NY, USA) that was used to displace it into the muscle, simulating intra-abdominal pressure from the pelvic organs on the PVM.

In order to construct a gelatin indenter with similar speed of sound and mechanical properties to the soft tissue it replaces in the PVM model, a series of indenters were made with different proportions of water, gelatin, n-propanol, and formalin based on methods from Hall et al. (1997). The contents of the indenters can be seen in Table 3.1. Each sample was sliced in half so that one portion could undergo mechanical testing while the other was used to determine speed of sound. Mechanical testing consisted of five cycles of sinusoidal preconditioning followed by a compressive, uniaxial test up to 10% strain using a 44.48 N load cell (E32593, TestResources) once a week for three weeks to determine if its mechanical properties would be stable. The samples showed a near-linear stress-strain response and an elastic modulus was fit to the mechanical data. The elastic modulus tended to rise

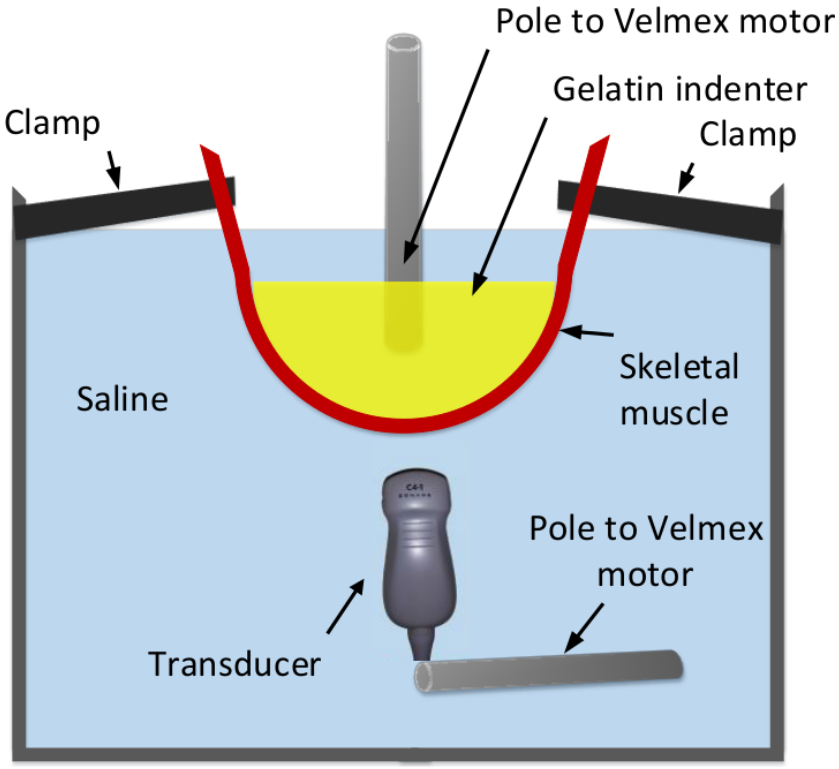

(a)

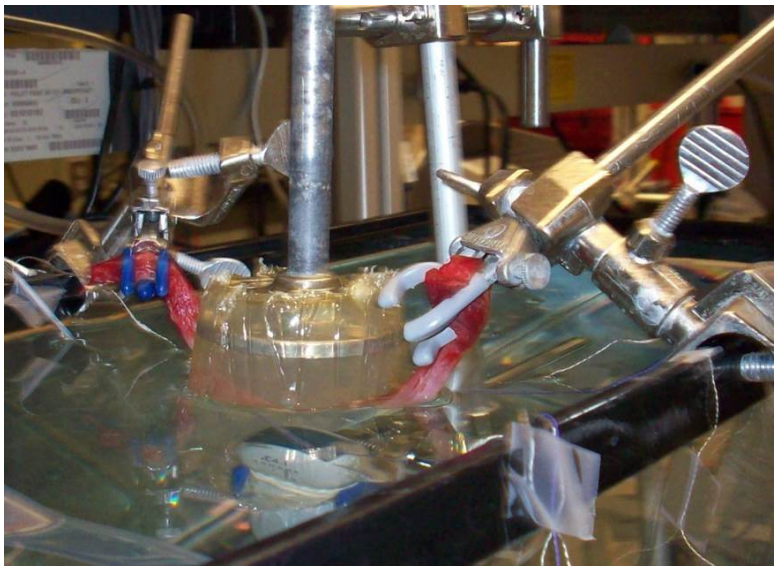

(b)

Figure 3.1: Diagram (a) and photo (b) of experimental setup showing the indenter, bovine skeletal muscle, mounting apparatus, and imaging transducer position.

Table 3.1: Amount of n-propanol and formalin in indenter samples made for mechanical and acoustic testing. Each indenter also contained 42 g gelatin and 460 g hot water.

Sample number	N-propanol (g)	Formalin (g)
1	63	1.5
2	54	1.5
3	45	1.5
4	36	1.5
5	36	6
6	36	4.5
7	36	3.0
8	36	1.5

with time, with increased formalin content, and with decreased n-propanol content (Fig. 3.3). The contents of samples 3, 4, and 8 gave elastic modulus closest to the target of 0.01 MPa. To calculate speed of sound, images were taken using a 8 MHz linear-array transducer (ZONARE Medical Systems, Mountain View, CA) of a bright reflector in a water bath with and without a section of indenter between the transducer and the reflector. By comparing the apparent distance from the transducer to the reflector, the offset of the indenter's speed of sound from that of water (1482 m/s) was calculated. Speed of sound tended to rise with increased formalin and decreased n-propanol content. Samples 4 and 8, which had equivalent content, were measured to have speed of sound closest to the target of 1540 m/s. For each experiment, a fresh indenter was constructed with 7.6% gelatin, 6.5% n-propanol, and 0.3% formaldehyde within a week of testing. This formulation had a speed of sound of 1543 ± 4 m/s and elastic modulus of 15 ± 4 MPa.

A 4 MHz curved-linear-array ultrasound transducer (ZONARE Medical Systems, Mountain View, CA) was held 3-6 cm below the muscle while attached by a rod to the Velmex

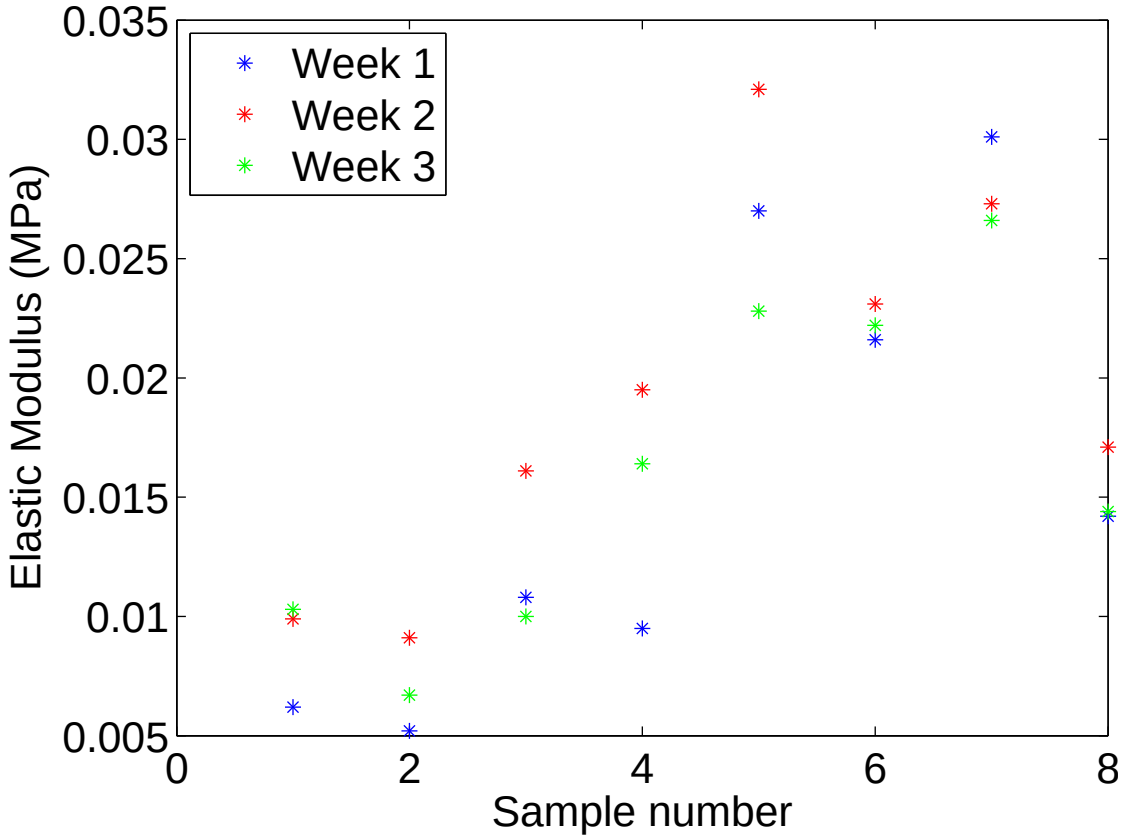

Figure 3.2: Elastic modulus of the indenter material samples of Table 3.1 over three weeks.

positioner system. A series of parallel 2D B-mode images, nominally aligned with the muscle fiber direction, was obtained by translating the array in increments of 0.4 mm in the elevation direction. Range and azimuthal pixel lengths were either 0.1923 mm or 0.2299 mm, depending on the image depth. After an initial volume of images was obtained, the indenter was lowered 0.2 mm into the muscle in the range direction and another set of 2D images spanning the muscle was obtained. This process was repeated for a series of indentations to build a volume of images of the muscle under incremental indentations. The indentation-imaging procedure was repeated until there were signs of muscle slippage from the grips or 25 indentations were reached. After the first experiment, it was noted that the rod connecting the indenter to the Velmex system caused a large reverberation artifact in the ultrasonic images. To avoid this in the subsequent experiments, the muscle was positioned slightly off center on the indenter so that the rod would not be directly over it and the artifact would not be present in the images.

These images were then exported in BMP format and imported to MATLAB (version R2011a, Mathworks, Natick, MA, USA) where all further image processing and calculations were performed. The images were scaled such that all pixel values fell between 0 and 1, and combined to create a 3D volume of the muscle at each indentation. In order to increase the elevational resolution and achieve a near-isotropic voxel size, the volumetric images were interpolated in the elevation direction, yielding a final 3D image with 0.2 mm between its elevational planes. For the first ten indentations, ten in-phase/quadrature (IQ) images were obtained from the middle of the muscle. In one experiment, ten IQ images were obtained at all twenty indentations of the experiment.

3.2.2 Sonomicrometry Measurements

To provide an independent measure of strain, a sonomicrometry system (Sonometrics, London, ON, Canada) was used. The system measures distances based on time-of-flight for

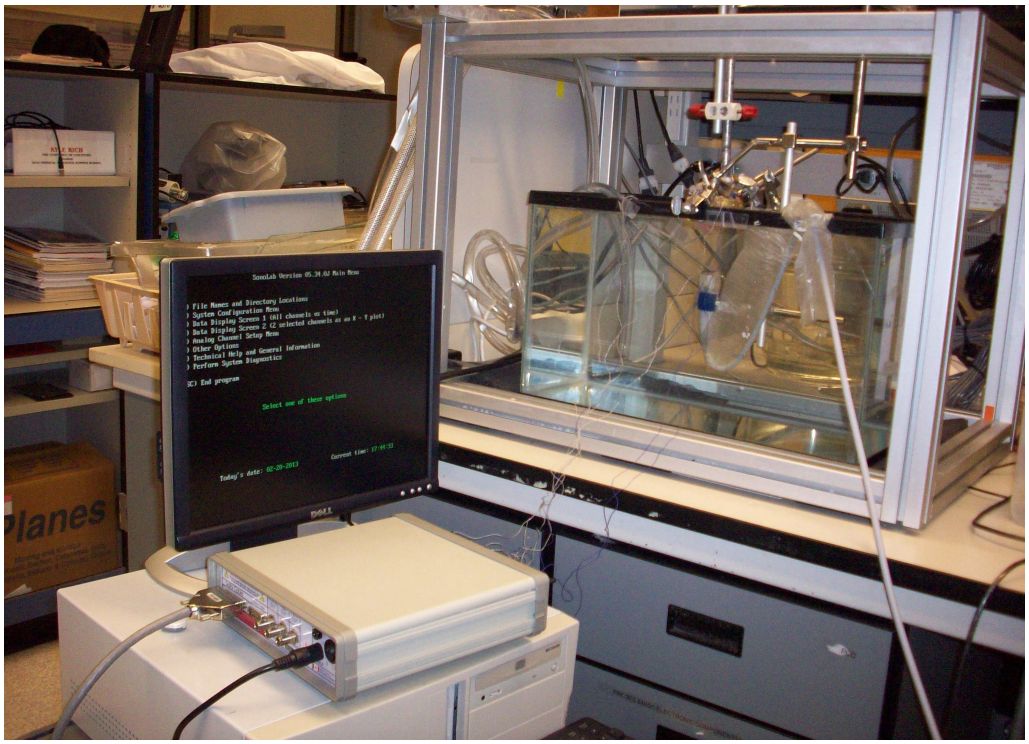

(a)

(b)

Figure 3.3: Photos of experimental setup. (a) Sonomicrometry system on the left and mounting apparatus on the right. (b) Full setup including the ultrasound system on the right and the laptop controlling the motor system and the ultrasound system in the middle.

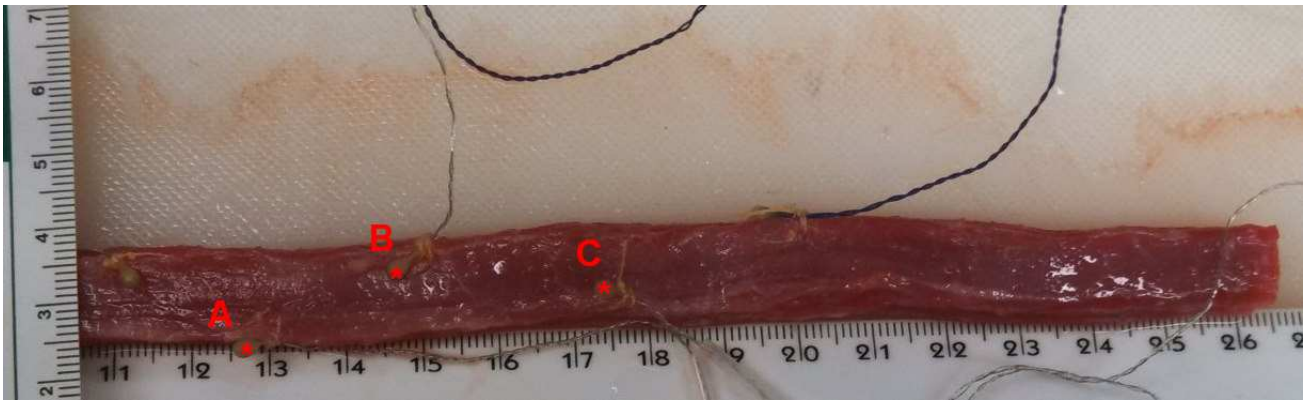

Figure 3.4: Photo of the muscle specimen with the sonomicrometry sensors sutured onto it before being placed in the sling position. The three sensors that were used to compute strain in this study are denoted with a star and a letter label.

a 1.2 MHz ultrasonic pulse from each of several piezoelectric sensors to the others, with a sampling period of 0.003 to 0.004 s and resolution of 0.012 mm. Five sensors were sutured onto the muscle as seen in Fig. 3.4, with three evenly spaced along one edge of the muscle 3–4 cm apart and the other two on the opposite edge, between the other three. Sensor positions were manually measured for an *a priori* estimate of initial distances between them. The three sensors in the middle of the muscle (those labeled A, B, and C in Fig. 3.4) were used to compute strain, while the other two were used for consistency checks.

During each experiment, the sonomicrometry system was active for the duration of each indentation, then disabled while each volumetric image was obtained. An example of the output from measuring distance between crystals during an intentation is in Fig. 3.5. Distance measurements from the sonomicrometry system were exported and analyzed in MATLAB. Median distances between the three central sensors were calculated for the first 100 data points measured in the initial configuration and the last 100 data points measured after the indentation sequence. If a calculated distance had a 10% or larger difference from the *a priori* distance measured before indentation, the experiment was excluded from analysis.

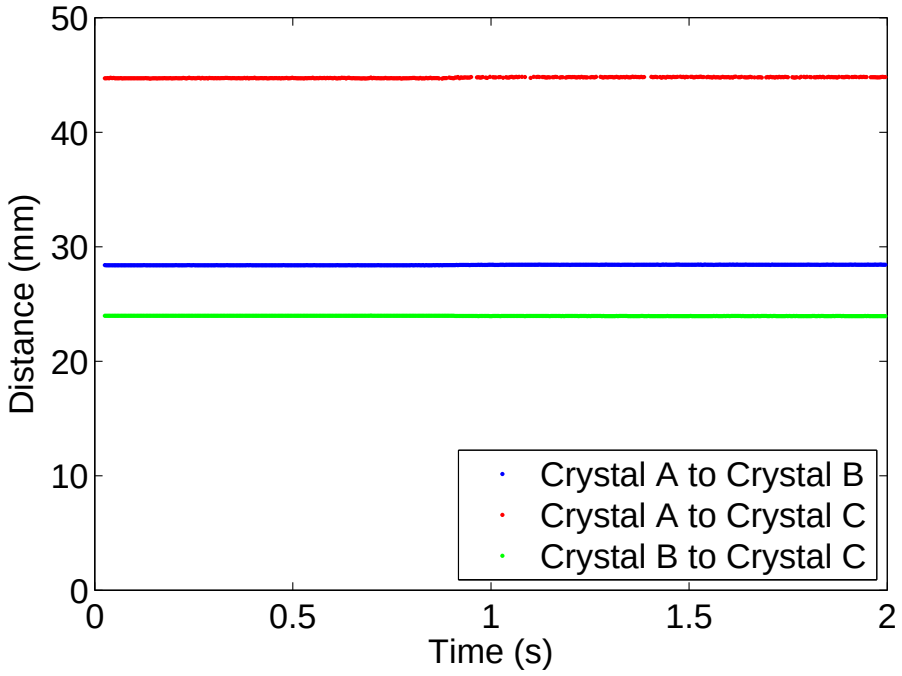

(a)

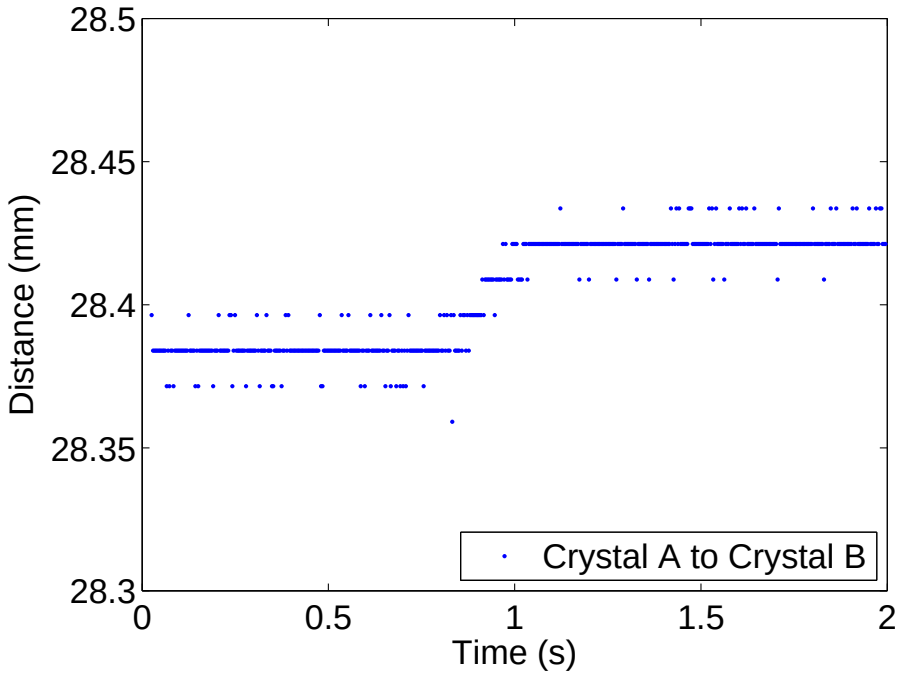

(b)

Figure 3.5: Plots of the distance signal from the sonomicrometry system for the final indentation of the third experiment. In (a), all three distances are shown. In (b), the plot is zoomed in to better see the signal from Crystal A to Crystal B.

Table 3.2: Size of the search radius for the texture tracking algorithm was determined by multiplying the size of the sub-volume by the magnification factor corresponding to the table.

Sub-volume side length (mm)	2.0	2.5	3.0	3.5	4.0	4.5	≥ 5
Magnification factor	1.5	1.4	1.4	1.3	1.3	1.3	1.2
Search region side length (mm)	3.0	3.5	4.2	4.55	5.2	5.85	≥ 6

3.2.3 Texture Correlation

Volumetric ultrasound images were used as inputs for a texture tracking algorithm which estimates local displacements by finding a cube-shaped image sub-volume, within a search region in the deformed image, having highest similarity to a sub-volume in the undeformed image (Nageswaran, 2008). For each sub-volume size investigated, a cube-shaped search region was specified with the minimum size required for consistent displacement estimates across all the experiments. These search regions were 1.2–1.5 times the size of the tracked sub-volumes with values in Table 3.2; further increases in search region size did not change displacement estimates, but only increased computation time.

Two different likelihood functions were investigated for quantifying the similarity between sub-volumes in the undeformed and deformed images. In one version, the likelihood used was a 3D extension of an exponential sum function proposed by Clocksin et al. (2002) [Eq. (3.1)], and in a second version, the Pearson correlation coefficient was used [Eq. (3.2)]:

$$\hat{\theta} = \text{argmax}\left[\frac{\sum e^{-(i_2-i_1)^2/\alpha}}{\text{maxlike}}\right], \tag{3.1}$$

and

$$\hat{\theta} = \text{argmax}\left[\frac{\sum(i_1-\bar{i_1})(i_2-\bar{i_2})}{\sqrt{\sum(i_1-\bar{i_1})^2\sum(i_2-\bar{i_2})^2}}\right]. \tag{3.2}$$

In Eqs. (3.1) and (3.2), $\hat{\theta}$ is the estimated position of the displaced sub-volume, i_1 and

i_2 are the respective sub-volumes of the undeformed and deformed images with mean values $\bar{i_1}$ and $\bar{i_2}$, "maxlike" is a normalization factor equal to the exponential sum term for $i_2 = i_1$, and α is a user-defined parameter that can be increased to smooth the likelihood map, thus lowering the influence of outliers. The effect of the α parameter was investigated by setting it to 0.1 to increase the peakedness of the likelihood map, to 1 to represent a standard version of the likelihood map, and to 100 to smooth the likelihood map. Examples of the likelihood maps for each correlation type can be seen in Fig. 3.6.

When Clocksin et al. (2002) proposed the exponential sum likelihood, it was paired with a prior function that was designed to bias the algorithm towards small displacements. To test if adding the prior would improve accuracy, it was added to the likelihood functions as shown in Eq. 3.3:

$$\hat{\theta} = \text{argmax}\left[\log\left(\cos\left(\frac{\sqrt{u^2+v^2+w^2}}{\pi s}\right)\right) + R\right], \tag{3.3}$$

where u, v, and w are displacements in the x, y, and z directions respectively, s is the maximum radius of the search region, and R is either the Clocksin or Pearson likelihood has defined in Eqs. 3.1 and 3.2. The prior yields a map where the location of zero displacement in the undeformed image has a value of 0 added to the likelihood while locations further away have negative numbers added to the likelihood with increasing magnitude with increasing displacement. Examples of the prior map and of likelihood maps added to the prior can be seen in Fig. 3.7.

For each sub-volume in the undeformed image, the likelihood or likelihood plus prior is calculated for all sub-volumes within the search region in the deformed image, and the location with the maximum argument is identified as the new location of the sub-volume in the deformed image. Large 3D deformations are tracked as the sum of smaller displacements by repeating this process for a sequence of volumetric images.

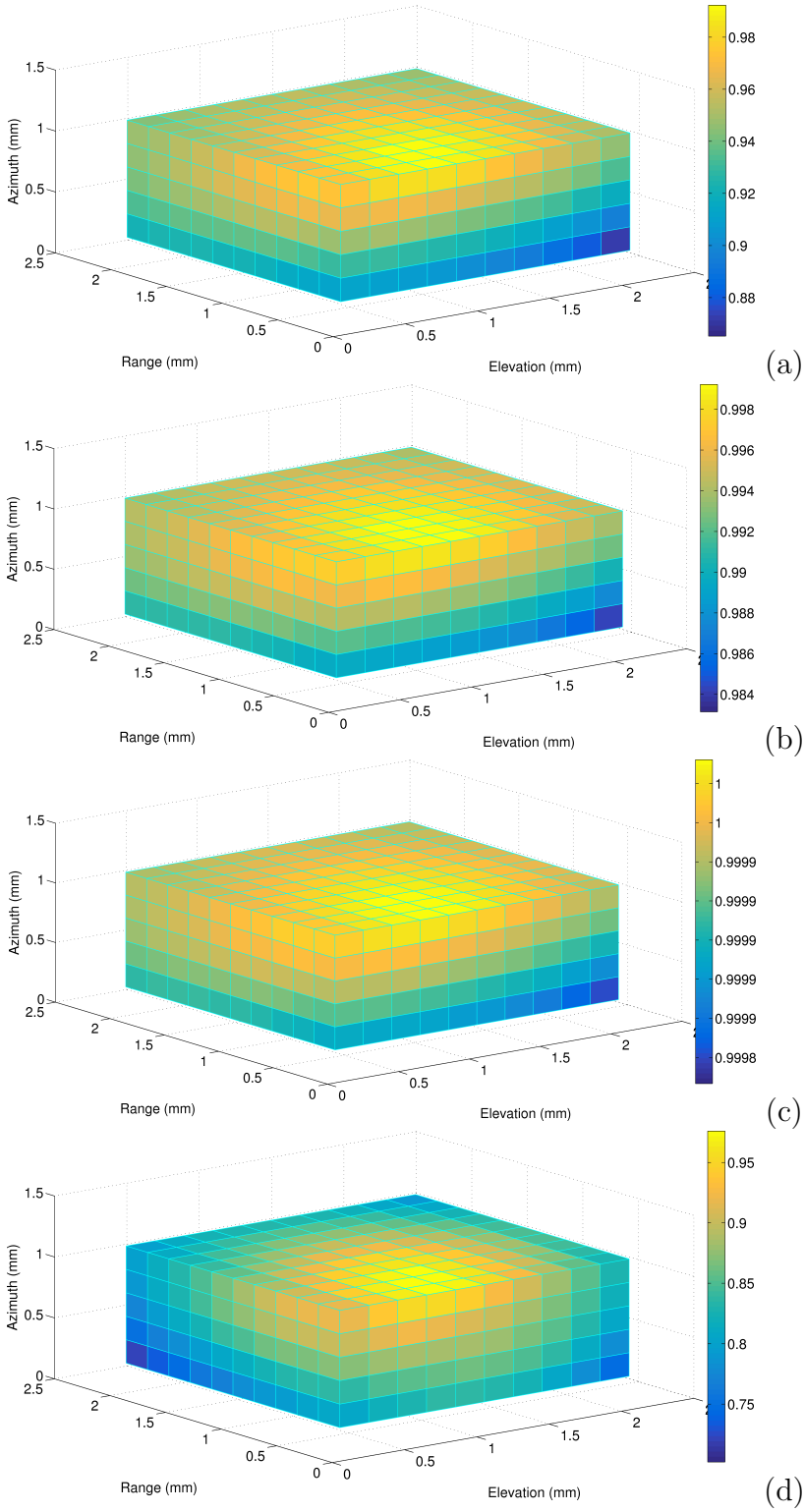

Figure 3.6: Middle cross section of the likelihood map showing similarity between the undeformed and deformed image using the Clocksin exponential sum likelihood with α set to 0.1 in (a), 1 in (b), 100 in (c), and with the Pearson likelihood in (d).

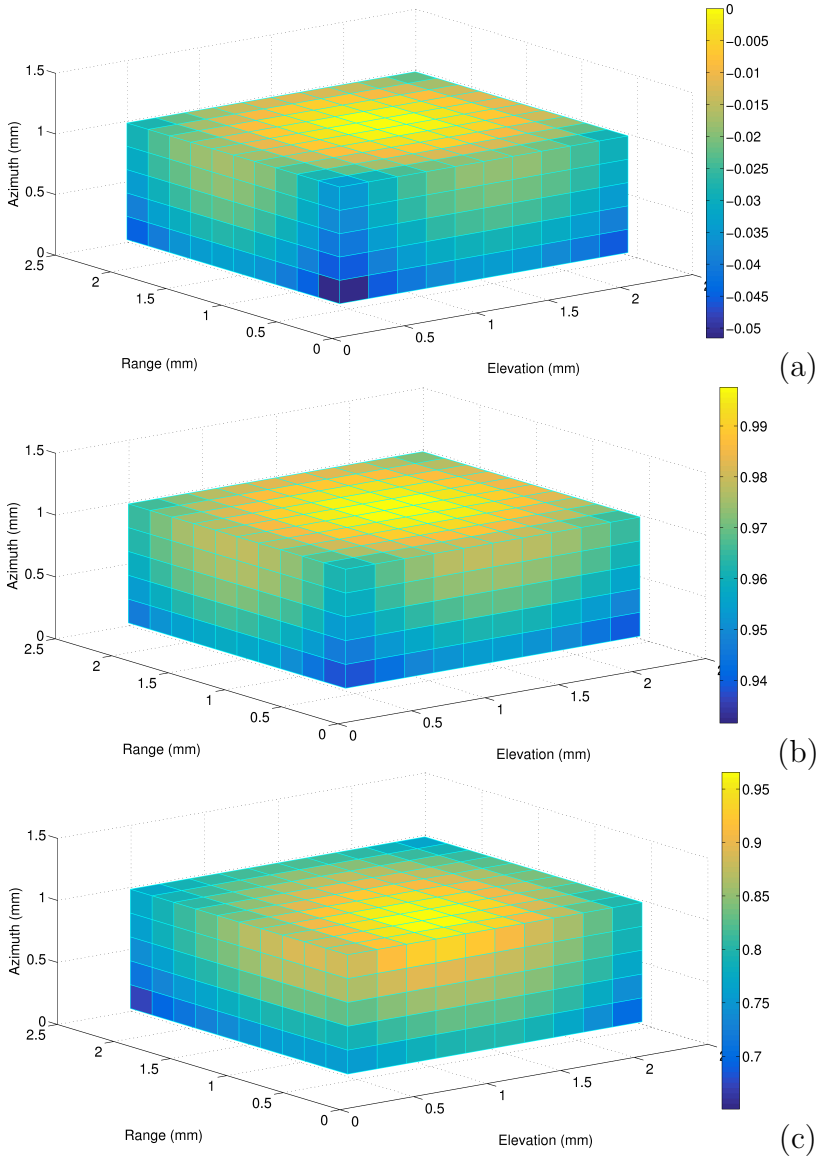

Figure 3.7: Middle cross section of the prior map showing the prior alone in (a), the combined prior and Clocksin likelihood map with α set to 1 in (b), and with the combined prior and Pearson likelihood map in (c). Compare to Fig. 3.6 to see the likelihood maps without the influence of the prior.

Three points in the initial volumetric image of each experiment were chosen inside the muscle near each of the three central sonomicrometry sensors. Tracked locations were required to be at least 3 mm from the edge of the image, so that sub-volumes surrounding the initial points remained fully within the bounds of the image. At each of these tracked locations, a cluster of five points was specified, consisting of the original point plus four surrounding points forming a square with edge length four voxels. After each point was tracked individually, displacements estimated for the five points within the same cluster were averaged to represent the displacement for the muscle at that sensor location, as seen in Fig.s 3.8 and 3.9.

To optimize sub-volume size for the texture tracking algorithm, the sub-volume side length was varied from 2 to 5.5 times the characteristic correlation length (CL) of the volumetric image speckle, in steps of one-half CL. To determine the CL, a region of interest was selected from the first volumetric image of each experiment, including the portion of the muscle between the three central sonomicrometry sensors. For each direction (azimuth, range, and elevation), the normalized autocorrelation function for each line of B-mode image data in this ROI was measured, and CL for that line was defined as the distance corresponding to an autocorrelation $r^2 = 0.25$. The mean CL for all lines in a given direction was defined as the CL for that direction. The representative CL of the muscle sample was then defined as the geometric mean of the elevation, azimuth, and range CLs.

To assess the effect of ultrasound signal decorrelation on strain mapping accuracy, displacements were also computed for volumetric image sequences with larger, regularly spaced indentation steps. These additional sequences were derived from the full volumetric image sequence by selecting image volumes separated by indentations of 0.4-1.2 mm instead of the original 0.2 mm steps.

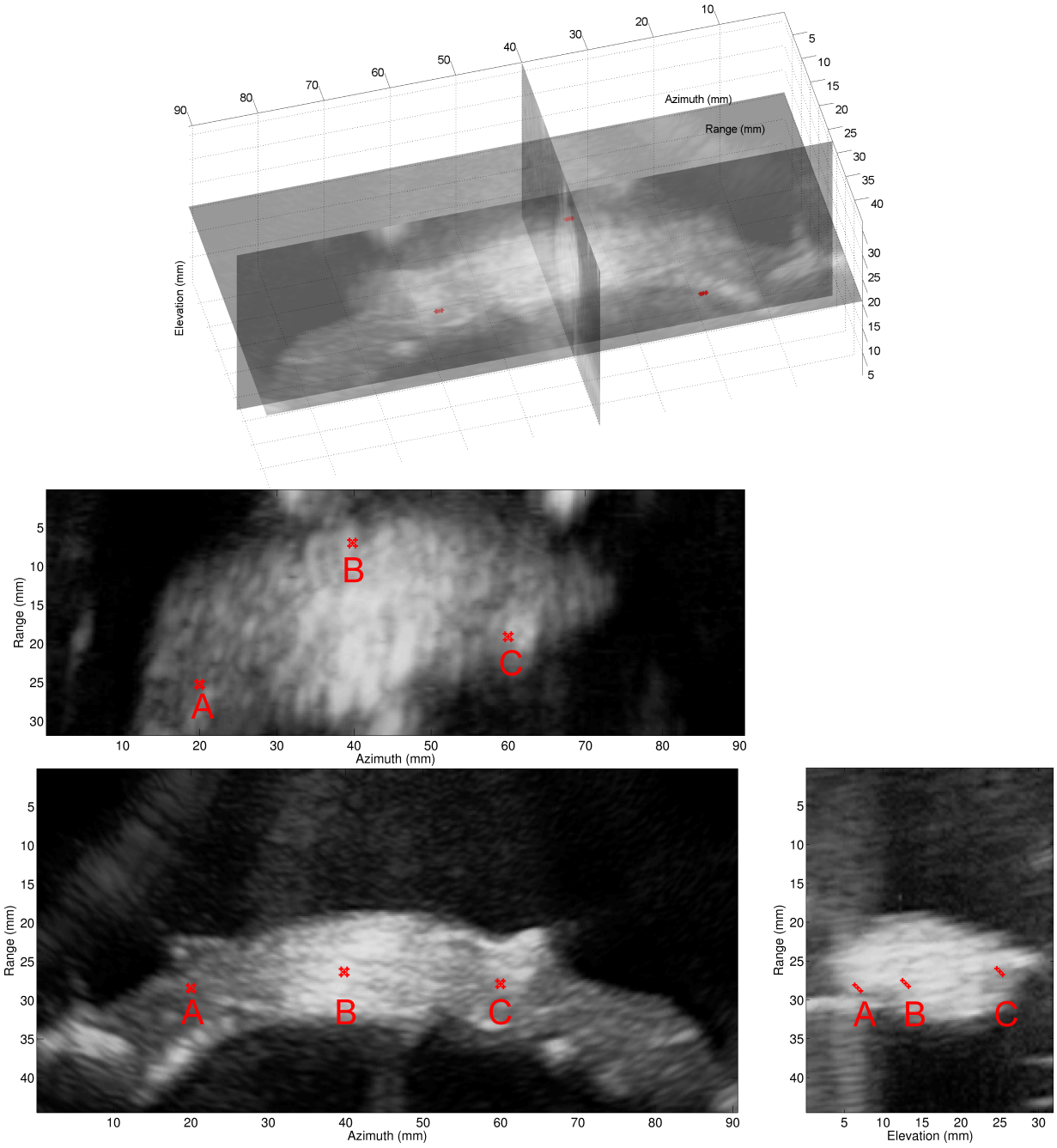

Figure 3.8: Cross-sectional planes through the image volume at the beginning of the indentation sequence. The upper left panel is a plane of the 3D image in the elevation-range direction, the lower left panel is in the azimuth-range direction, the lower right is in the elevation-azimuth direction, and the upper right panel shows these planes plotted together. The crosses indicate locations of the 15 points that were tracked clustered at the three locations labeled A, B, and C in the undeformed image.

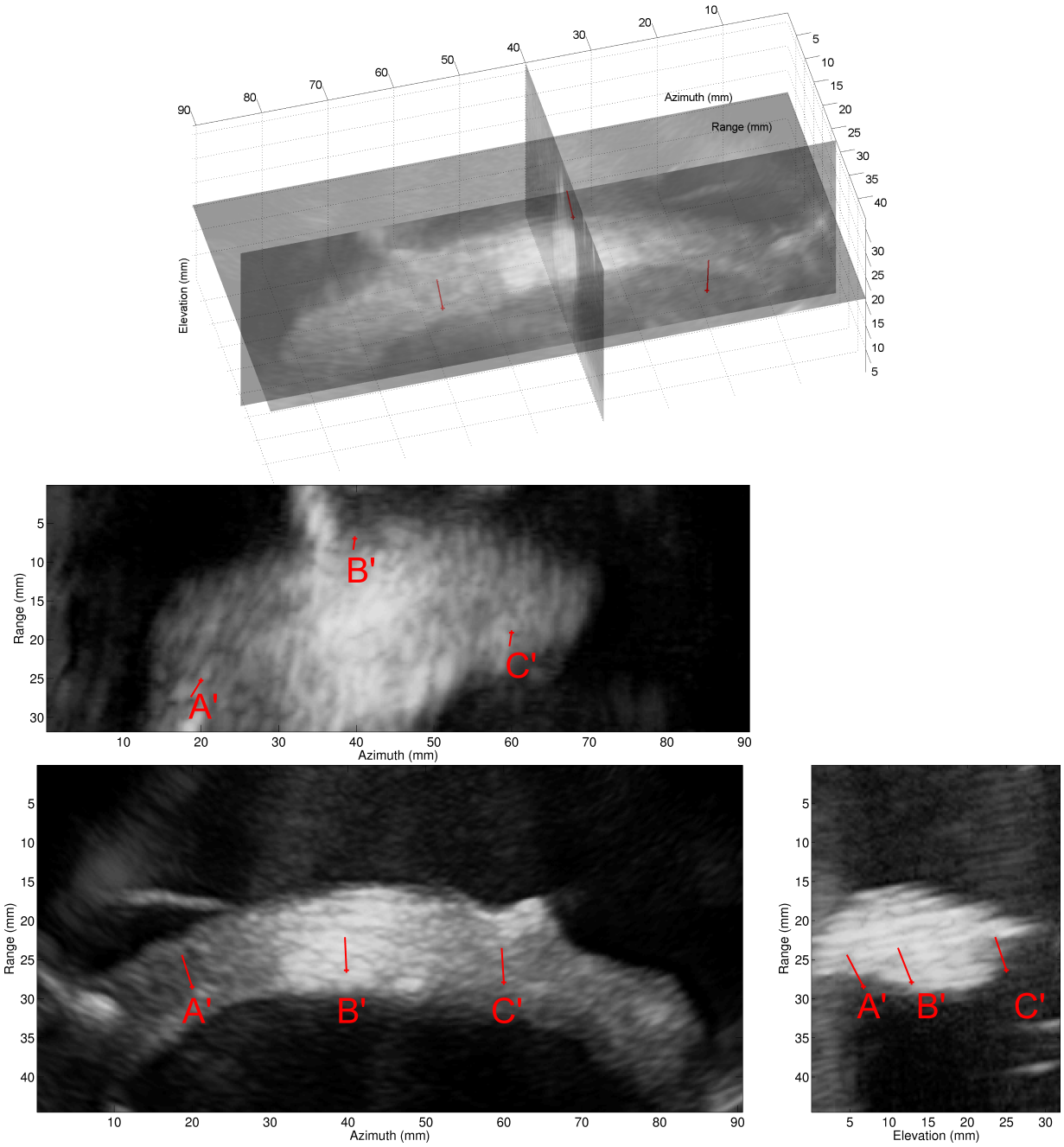

Figure 3.9: Cross-sectional planes through the image volume at the end (bottom four images) of the indentation sequence. In each set of four, the upper left panel is a plane of the 3D image in the elevation-range direction, the lower left panel is in the azimuth-range direction, the lower right is in the elevation-azimuth direction, and the upper right panel shows these planes plotted together. Locations A', B', and C' in the deformed image indicate the initial location of the tracked clusters of points. The arrows indicate the displacement of those points after being averaged together.

3.2.4 Decorrelation Calculation

Echo decorrelation imaging is a pulse-echo technique quantifying the position-dependent level of change between two image frames (Mast et al., 2008). The echo decorrelation imaging approach used here was developed to monitor thermal ablation (Mast et al., 2008; Hooi et al., 2015). Local decorrelation was computed for each image sequence, using an echo decorrelation definition and data processing method described in Hooi et al. (2015). Echo decorrelation is analyzed here using previously developed theory of scattering from weakly inhomogeneous tissue (Waag et al., 1992; Jansson et al., 1998) to determine the contributions of tissue motion, strain, electronic noise, and measurement system effects.

Echo decorrelation is analyzed as a representation of position-dependent changes between two ultrasound pulse-echo image frames $I_0(y,z)$ and $I_1(y,z)$, with y denoting the azimuth (array) direction and z denoting the range (depth) direction within the image plane. Following the notation of a previous simulation study (Mast, 2010), each image frame comprises a collection of complex pulse-echo signals with real and imaginary parts in baseband-demodulated (IQ) form. The starting point for echo decorrelation analysis is a position-dependent, zero-lag, windowed spatial cross-correlation between the two complex image frames, defined here as

$$\begin{aligned} R_{01}(y,z) &= \iint w(y-y',z-z')\, I_0(y',z')^*\, I_1(y',z')\, dy'dz' \\ &\equiv \langle I_0(y,z)^* I_1(y,z) \rangle \,, \end{aligned} \tag{3.4}$$

where the star denotes complex conjugation and the angle brackets denote convolution with a windowing function w centered at the (azimuth, range) location (y,z). Similarly, image autocorrelations are defined as $R_{00}(y,z) = \langle |I_0(y,z)|^2 \rangle$ and $R_{11}(y,z) = \langle |I_1(y,z)|^2 \rangle$, which can be regarded as maps of spatially integrated backscattered energy (Mast et al., 2008).

An echo decorrelation image, representing a position-dependent map of echo signal changes

between the two image frames, is then given by a normalized correlation coefficient subtracted from unity:

$$\Delta(y,z) = 1 - \frac{|R_{01}(y,z)|^2}{R_{00}(y,z)\,R_{11}(y,z)}. \tag{3.5}$$

The echo decorrelation map defined by Eq. (3.5) is analyzed using an approximate representation of pulse-echo ultrasound images, derived previously (Mast, 2010). This representation is based on scattering theory for a three-dimensional, linear, weakly scattering inhomogeneous medium (Morse and Ingard, 1968) subjected to a narrow-band incident waveform of the form $a(t)\,e^{-i2\pi f_0 t}$, incorporating the effects of transmit and receive aperture beam patterns (Jansson et al., 1998). Under these assumptions, a complex image frame can be defined, within multiplicative constants, as

$$I_0(y,z) = \int_{V_0} \gamma(\mathbf{r}_0)\,e^{-2ik_0 z_0}\,\Lambda(\mathbf{r}_0,y,z)\,dV_0 + n(y,z), \tag{3.6}$$

where $\mathbf{r}_0$ is a coordinate within the 3D scattering volume, γ is the position-dependent tissue reflectivity, k_0 is the wavenumber ω_0/c for the pulse radial center frequency ω_0 and the sound speed c, the additive term $n(y,z)$ represents uncorrelated, spatially varying electronic noise, and Λ is a slowly-varying, position-dependent "system function" incorporating the influence of transmit and receive beam patterns and waveforms (Waag et al., 1992; Jansson et al., 1998):

$$\Lambda(\mathbf{r}_0,y,z) \equiv p_E(x_0,y-y_0,z_0)\,p_D(x_0,y-y_0,z_0)\,a\left(\frac{2(z-z_0)}{c}\right)e^{2ik_0 z_0}. \tag{3.7}$$

In Eq. (3.7), p_E and p_D are complex beam patterns of the transmitting and receiving apertures, evaluated using Rayleigh integrals at the center frequency f_0 of the imaging pulse, and $a(t)$ is the complex envelope of the imaging pulse (Mast, 2010). The system function Λ can be regarded as a generalized point-spread function that is also dependent on the pixel location (y,z) within the pulse-echo image plane. The pulse-echo image model of Eqs. (3.6)

and (3.7) thus incorporates diffraction effects more accurately than models based on convolutions of a position-independent point-spread function with the scattering medium (Mast, 2010).

Following previous theory for scattering from soft tissue (Waag et al., 1992), we take the tissue reflectivity γ to be a wide-sense stationary, delta-correlated random variable. The scattering medium $\gamma(\mathbf{r}_0)$, comprising the tissue reflectivity imaged by frames I_0 and I_1, is assumed to be unchanged except for any translational motion and deformation. The spatial autocorrelation of the tissue reflectivity, $R_{\gamma_{01}}$, is assumed to depend only on the spatial lag $\mathbf{r}' = |\mathbf{r}_1 - \mathbf{r}_0|$ and on the image coordinates (y, z), and is assumed small except near a peak at the position $\mathbf{r}' = \delta\mathbf{r} = (\delta x, \delta y, \delta z)$, corresponding to translational displacement of the tissue, relative to the imaging array, between the two frames. The other quantities considered, including the beam functions, transmit waveform shape, and electronic noise level, are assumed to vary negligibly between the frames I_0 and I_1. Under these assumptions, an expected value of the cross-correlation function from Eq. (3.4) can be written using Eq. (3.6) as

$$\begin{aligned} E\left[R_{01}(y,z)\right] &\approx \left\langle \int_{V_0}\int_{V'} R_{\gamma_{01}}(\mathbf{r}', y, z)\, e^{2ik_0 z'}\, \Lambda(\mathbf{r}_0, y, z)^* \Lambda(\mathbf{r}_0 + \mathbf{r}', y, z)\, dV_0\, dV' \right\rangle \\ &\approx \langle S_{\gamma_{01}}(2k_0\mathbf{e}_z, y, z)\rangle\, R_\Lambda(\delta\mathbf{r}, y, z), \end{aligned} \tag{3.8}$$

where $E[\cdot]$ represents the expected value or ensemble average and R_Λ is the spatial autocorrelation of the system function Λ. The latter approximation in Eq. (3.8) assumes that the system function autocorrelation $R_\Lambda(\delta\mathbf{r}, y, z)$ is slowly varying with respect to the pixel location (y, z), meaning that measurement system effects within a spatial window $w(y, z)$ are adequately described by a single pulse-echo point-spread function.

In Eq. (3.8), $S_{\gamma_{01}}(\mathbf{k}, y, z)$ is the position-dependent cross-spectrum of the two scattering medium realizations, equal by the Wiener-Khinchin theorem to the 3D spatial-frequency

Fourier transform of the position-dependent cross-correlation $R_{\gamma_{01}}(\mathbf{r}', y, z)$ between the two scattering medium realizations γ_0 and γ_1. Similar to previously derived Fourier relationships for tissue scattering (Lerner and Waag, 1988), this cross-spectrum is evaluated at the vector spatial frequency $\mathbf{k} = 2k_0\mathbf{e}_z$, where $\mathbf{e}_z$ is the unit vector in the axial or range direction. Thus, the windowed cross-correlation of the two images is equivalent to a product of the cross-spectrum of the tissue reflectivity functions γ_0 and γ_1, evaluated at a spatial frequency determined by the imaging pulse, with a deterministic autocorrelation function of the system function Λ, which depends only on the transmit and receive beams, pulse waveform, and tissue displacement.

Similarly, the autocorrelation of the complex image $I_0(y, z)$ can be written in terms of the spatial-frequency autospectrum of the tissue reflectivity as

$$\begin{aligned} E\left[R_{00}(y,z)\right] &\approx \left\langle S_{\gamma_{00}}(2k_0\mathbf{e}_z, y, z)\right\rangle R_\Lambda(0,y,z)\left(1+\mathrm{SNR}(y,z)^{-1}\right), \text{ where} \\ \mathrm{SNR}(y,z) &\equiv \frac{E\left[R_{00}(y,z)\right]}{E\left[\langle |n(y,z)|^2\rangle\right]}, \end{aligned} \tag{3.9}$$

and likewise for the image $I_1(y, z)$.

For a statistically homogeneous scattering medium, $\Delta(y, z) \ll 1$, the image autocorrelation (spatially smoothed integrated backscatter) functions R_{00} and R_{11} are nearly constant. Under this assumption, the expected value of the echo decorrelation image from Eq. (3.5) can be written in terms of the scattering medium's power spectra, the system function Λ, the tissue displacement $\delta\mathbf{r}$, and the signal-to-noise ratio SNR as

$$E[\Delta(y,z)] \approx 1 - \rho(\delta\mathbf{r}, y, z)\ \frac{\left\langle S_{\gamma_{01}}(2k_0\mathbf{e}_z, y, z)\right\rangle^2}{\left\langle S_{\gamma_{00}}(2k_0\mathbf{e}_z, y, z)\right\rangle \left\langle S_{\gamma_{11}}(2k_0\mathbf{e}_z, y, z)\right\rangle}, \tag{3.10}$$

where

$$\rho(\delta\mathbf{r}, y, z) = \left| \frac{R_\Lambda(\delta\mathbf{r}, y, z)}{R_\Lambda(0, y, z)} \frac{\mathrm{SNR}(y,z)}{1+\mathrm{SNR}(y,z)} \right|^2 \tag{3.11}$$

is the normalized position-dependent autocorrelation of the system function Λ, multiplied by a term comprising the influence of electronic noise.

If the tissue medium is unchanged and all decorrelation is due to translational tissue motion, Eq. (3.11) is equivalent to previous analyses of motion-induced echo decorrelation, in which the echo signal correlation is equal to a spatial correlation of the imaging system's point-spread function (O'Donnell and Silverstein, 1987; Chen et al., 1997; Walker, 2001; Ng et al., 2006), weighted by a correlation coefficient associated with electronic noise (Insana et al., 2000). By incorporating the position-dependent system function of Eq. (3.7), Eq. (3.11) is equivalent to previous expressions derived for echo decorrelation, as a function of tissue or aperture translation, employing shift-variant point-spread functions (Walker, 2001; Ng et al., 2006).

Decorrelation associated with tissue strain or deformation can be incorporated into Eq. (3.11), given the assumption that the tissue reflectivity power spectrum S_γ varies slowly with spatial frequency, by applying the scaling theorem for Fourier transforms to the cross-spectrum term $\langle S_{\gamma_{01}}(2k_0\mathbf{e}_z, y, z)\rangle^2$. The result for small strains is equivalent to a multiplicative scale factor in the term $\rho(\delta\mathbf{r}, y, z)$, which becomes

$$\rho(\delta\mathbf{r}, y, z) = \left| \frac{R_\Lambda(\delta\mathbf{r}, y, z)}{R_\Lambda(0, y, z)} \frac{\mathrm{SNR}(y, z)}{1 + \mathrm{SNR}(y, z)} \frac{1}{1 + \epsilon(y, z)} \right|^2 \tag{3.12}$$

where $\epsilon(y, z)$ is the local strain. For small strains, this agrees with a previous theory relating echo signal decorrelation with tissue strain (Varghese and Ophir, 1996; Alam and Ophir, 1997; Varghese and Ophir, 1998). For large strains exceeding several percent, previous simulation results have shown a highly variable relationship between decorrelation and strain (Varghese and Ophir, 1996; Alam and Ophir, 1997). Decorrelation caused by motion and strain is calculated as

$$\Delta_\rho = 1 - \rho(y, z) \tag{3.13}$$

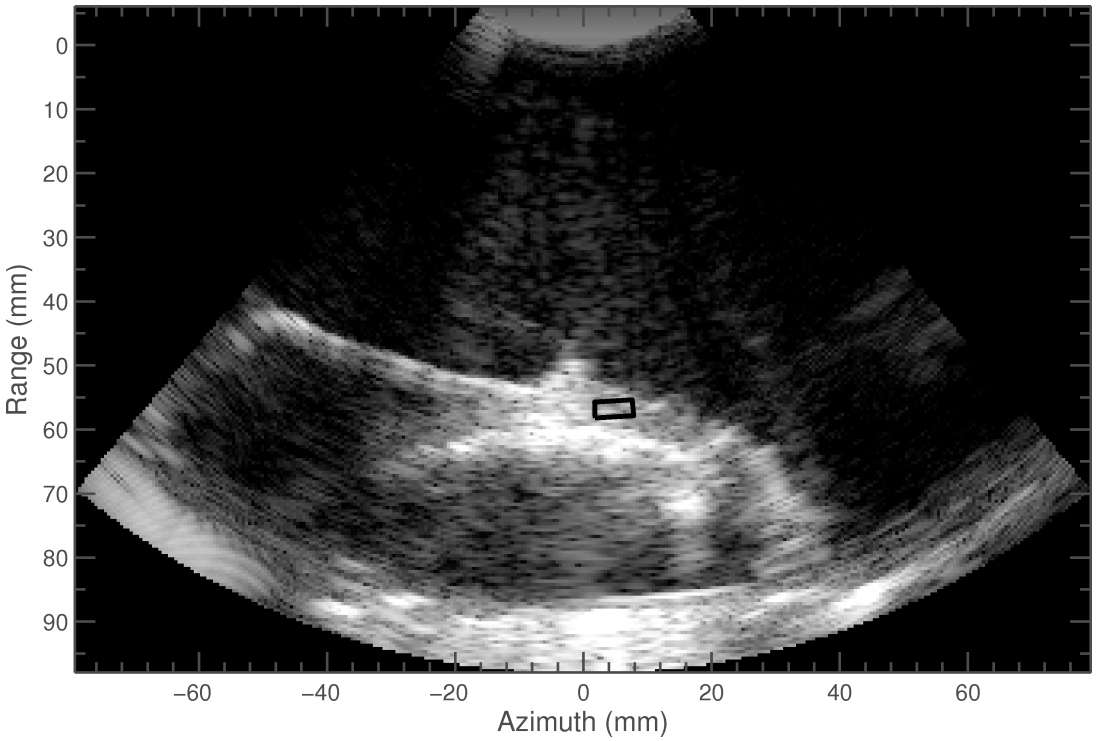

Figure 3.10: A representative cross-sectional B-scan from the acquired volumetric image of the PVM model. The ROI used for echo decorrelation computations is shown by a superimposed rectangle.

with $\rho(y, z)$ specified by Eq. (3.11) or by Eq. (3.12) to incorporate strain.

Echo decorrelation was analyzed in a region of interest (ROI) within the muscle in the IQ images, chosen as close to the muscle midline as possible. Care was taken in segmenting the ROI to avoid bright areas associated with reflections from any wires near the tissue and reverberations from the indenter mounting rod. A representative B-scan image is shown in Fig. 3.10 with the analyzed ROI marked by a superimposed rectangle.

Echo decorrelation images of the muscle specimen were computed using Eq. (3.5), spatially averaged within the ROI, and ensemble averaged. For analysis of echo decorrelation as a function of range (indentation direction) displacement, averages were taken over all pairs of image planes matching a range displacement δz from the first six indentation positions. For the experiment with IQ images from all twenty indentation positions, averages were

taken over all pairs of image planes with matching range displacement for the first twelve indentation positions. The spatial windowing of Eq. (3.4) was performed using the Gaussian window

$$w(y, z) = e^{-(y^2+z^2)/(2\sigma^2)} \tag{3.14}$$

with $\sigma = 2$ mm, sufficient in size to spatially smooth stochastic fluctuations while maintaining acceptable spatial resolution.

Experimental decorrelation values were compared to theoretical values caused by tissue motion, computed using Eq. (3.12), with the measurement system function Λ computed using the Fresnel approximation (Mast, 2007). Transmit and receive beams were computed with a continuous f-number of 2 for a transducer elevation width of 15 mm and elevation focal depth of 80 mm, approximated as a linear aperture for simplicity. The pulse center frequency and the temporal width of the Gaussian transmit pulse were estimated by fit to a pulse-echo signal from the first image of each experiment. The average engineering strain at each indentation step as calculated by the texture tracking algorithm with the optimum sub-volume size for each indentation step was used in Eq. (3.12) to compute the corresponding theoretical decorrelation.

3.2.5 Strain Calculation and Comparison

Distances between the sonomicrometry sensors and between the tracked image points were used to calculate strain for each sub-volume length and likelihood type, following methods described in Boresi et al. (2010). Individual engineering strain (ϵ) measurements were computed for each of the three pairs of points as

$$\epsilon = \frac{\acute{A}\acute{B}}{AB} - 1, \tag{3.15}$$

where AB represents the distance from one tracked location (A) to another (B) in the initial undeformed configuration and $\acute{A}\acute{B}$ represents this distance in the final deformed configuration.

These three distances were also used to compute the deformation tensor (F) for the region (Sun et al., 2005),

$$F = \begin{bmatrix} \acute{A}\acute{B}_x & \acute{A}\acute{C}_x \\ \acute{A}\acute{B}_y & \acute{A}\acute{C}_y \end{bmatrix} \begin{bmatrix} AB_x AC_x \\ AB_y AC_y \end{bmatrix}^{-1}, \tag{3.16}$$

where AB_x and AC_x are the x components and AB_y and AC_y the y components of vectors between undeformed points in their local coordinate system. The corresponding vector components for the deformed configuration are denoted with apostrophes. The deformation tensor from Eq. (3.16) was then used to compute the 2D Green deformation tensor (E)

$$E = \frac{F^T F - I}{2} \tag{3.17}$$

where I is the 2D identity matrix.

Eigenvectors V_s and eigenvalues E_s for the Green strain tensor from the sonomicrometry-measured distances were calculated. It was assumed that the larger of the two eigenvalues represented the strain in the fiber direction, while the smaller eigenvalue represented the strain perpendicular to the fiber direction for muscle between the three sensor locations. In the resulting coordinate system, shear strain of muscle in this region was zero by definition. The rotations specified by these eigenvectors were confirmed by visually comparing them to the angles between the crystals used as the x axis and the fiber direction in images of the muscle laid flat, such as Fig. 3.4. For comparison with sonomicrometry measurements, the Green strain E_i obtained from the texture tracking algorithm was rotated into the same

coordinate system,

$$E_r = V_s^{-1} E_i V_s. \tag{3.18}$$

Errors in strain estimation were defined as the difference between strains measured by the sonomicrometry system and by the texture correlation algorithm. For the engineering strain, each experiment's three sonomicrometry strain measurements were paired with the corresponding strains measured using the texture correlation algorithm. For the Green strain, the two normal components of E_r were compared to the corresponding normal components of E_s, while the shear component of E_r was compared to zero shear strain. Absolute root-mean-square (RMS) errors for texture correlation were computed for each strain type as the RMS difference from the corresponding sonomicrometry-measured strains. Normalized RMS strain errors were also computed, dividing the absolute RMS strain error by the RMS value of the corresponding sonomicrometry-measured strain, except for the Green strain in the shear direction. Two-tailed paired t-tests were used to determine whether strains measured using the texture correlation algorithm were biased compared to the sonomicrometry-measured strains for the data obtained using the full image sequence, and thus the smallest indentation size of 0.2 mm.

In the statistical package R (R Core Team, 2013), a series of statistical tests were performed on the data to assess the dependence of strain estimation error on sub-volume size for strains estimated from measurements using the smallest indentation step size. A Kolmogorov-Smirnov test was first used to determine whether strain errors were normally distributed. For data following a normal distribution, an ANOVA test would be used to assess whether the mean errors for different sub-volume lengths were significantly different, and a Bartlett test would be used to determine whether the variances of these errors were significantly different. If the strain errors were determined not to follow a normal distribution, a Kruskal-Wallis test would be used instead of ANOVA, and a Brown-Forsythe Levene

test would be used instead of the Bartlett test. For the sub-volume length with the lowest normalized RMS error, a t-test was used to compare strains estimated by the texture correlation algorithm using the four different likelihood functions, to determine whether any was significantly different from the others. Correlation coefficients between strain error and indentation step size and between strain error and mean decorrelation were calculated in MATLAB for strains estimated by the Clocksin likelihood with $\alpha = 1$. For all statistical tests, $p < 0.05$ was considered significant.

3.3 Results

A total of six experiments were performed. Individual details for these experiments are summarized in Table 3.3. One experiment was excluded from analysis because one sonomicrometry sensor was less than 3 mm from the image volume edges, while a second experiment was excluded because two of the three sonomicrometry distance measurements had greater than 10% error relative to the *a priori* manual distance measurement. The mean and standard deviation thickness, width, and length of the muscle samples used in the remaining four experiments were 7.75 ± 1.26 mm, 12.0 ± 2.2 mm, and 195 ± 17.3 mm. The mean engineering strain measured by the sonomicrometry system was 0.021 ± 0.019 for the four experiments. The mean Green strain was 0.069 ± 0.037 parallel to the estimated fiber direction and -0.011 ± 0.013 perpendicular to the fiber direction. The mean CL of the volumetric ultrasound images was 1.30 ± 0.14 mm.

Absolute and normalized RMS strain errors for the four analyzed experiments are plotted as a function of sub-volume length in Fig. 3.11 for each of the four displacement estimators. Error tended to be lowest for sub-volumes with side lengths of 3–4 CL. The minimum absolute RMS error for all sub-volume sizes for the engineering strain was 0.0055 (19.6% normalized to the RMS sonomicrometry-measured strain). The minimum absolute RMS error for the

Table 3.3: Information on the six experiments conducted including the date, the thickness (thick.) of the sample, the width of the sample, the length of the sample, the resolution (res.) of the B-mode images, the measured correlation length (CL), the mean engineering strain ($\bar{\epsilon}$), the estimated strain in the fiber direction (E_{fiber}), and any reasons to exclude the data. The fiber strain is the maximum eigenvalue of the Green strain tensor at the end of the experiment as measured by sonomicrometry. The exclusion criteria lists include having a sonomicrometry sensor too close to an edge or greater than 10% error between the sonomicrometry distances and *a priori* distance measurements. The mean and standard deviation (std) in the last two rows are only for the four experiments with no reasons for exclusion.

Experiment date	Thick. (mm)	Width (mm)	Length (cm)	Res. (mm)	CL (mm)	$\bar{\epsilon}$	E_{fiber}	Exclusion criteria
02/20/2013	8	10	18	0.2299	1.25	0.0319	0.0672	None
01/23/2014	7	12	18	0.2299	1.33	NA	NA	Edge
01/24/2014	8	12	22	0.1923	1.55	0.0076	0.0433	None
04/08/2014	10	12	19	0.2299	1.57	0.0289	0.0497	$>10\%$ error
04/09/2014	5	17	19	0.1923	1.27	0.0257	0.0433	None
04/10/2014	9	12	19	0.1923	1.12	0.0203	0.1207	None
Mean	7.8	12.0	195	0.2017	1.30	0.021	0.069	
Std	1.3	2.2	17	0.0188	0.14	0.019	0.037	

Green strain was 0.0237 (29.6% normalized) in the direction parallel to the fibers, 0.0147 (80.6% normalized) in the direction perpendicular to the fibers, and 0.0128 in the shear direction. The t-tests showed no significant difference in means between the engineering strains or the Green strain components calculated from the sonomicrometry measurements and those measured by the texture tracking algorithm, for any of the four likelihood versions at any of the eight sub-volume lengths.

When the prior was added to the likelihood functions as in Eq. 3.3, the error was close to 100% in most cases as the displacements and strains were 0 in all but a few steps. Because of this, the plots and statistical analysis are only presented for the results where the prior was not used.

For all types of strain, the distribution of errors was not normal as measured by the Kolmogorov-Smirnov test ($p < 10^{-15}$ for the engineering strain and $p < 10^{-6}$ for the Green strain components). Table 3.4 shows the p values from the Kruskal-Wallis (third column) and Levene (fourth column) tests, with significant values shown in bold text. The Kruskal-Wallis test showed significant differences in mean errors among different sub-volume lengths for the engineering strain measured using the Clocksin likelihood with all three values of α, but not for the Pearson likelihood, nor for any of the Green strain components. The Levene test showed that there were significant differences between variances of the errors among different sub-volume lengths for the Green strain component perpendicular to the fiber direction with all four likelihood versions, but not for the engineering strain, nor for the other Green strain components.

At the sub-volume length with smallest RMS error, 4 CL, the series of t-tests showed that no significant difference between engineering strains estimated using the Clocksin likelihood with the three different values of α ($0.437 \leq p \leq 0.577$). However, marginally significant differences were observed between all engineering strains measured using the Clocksin likelihood functions and those measured using the Pearson likelihood ($0.041 \leq p \leq 0.051$). Green

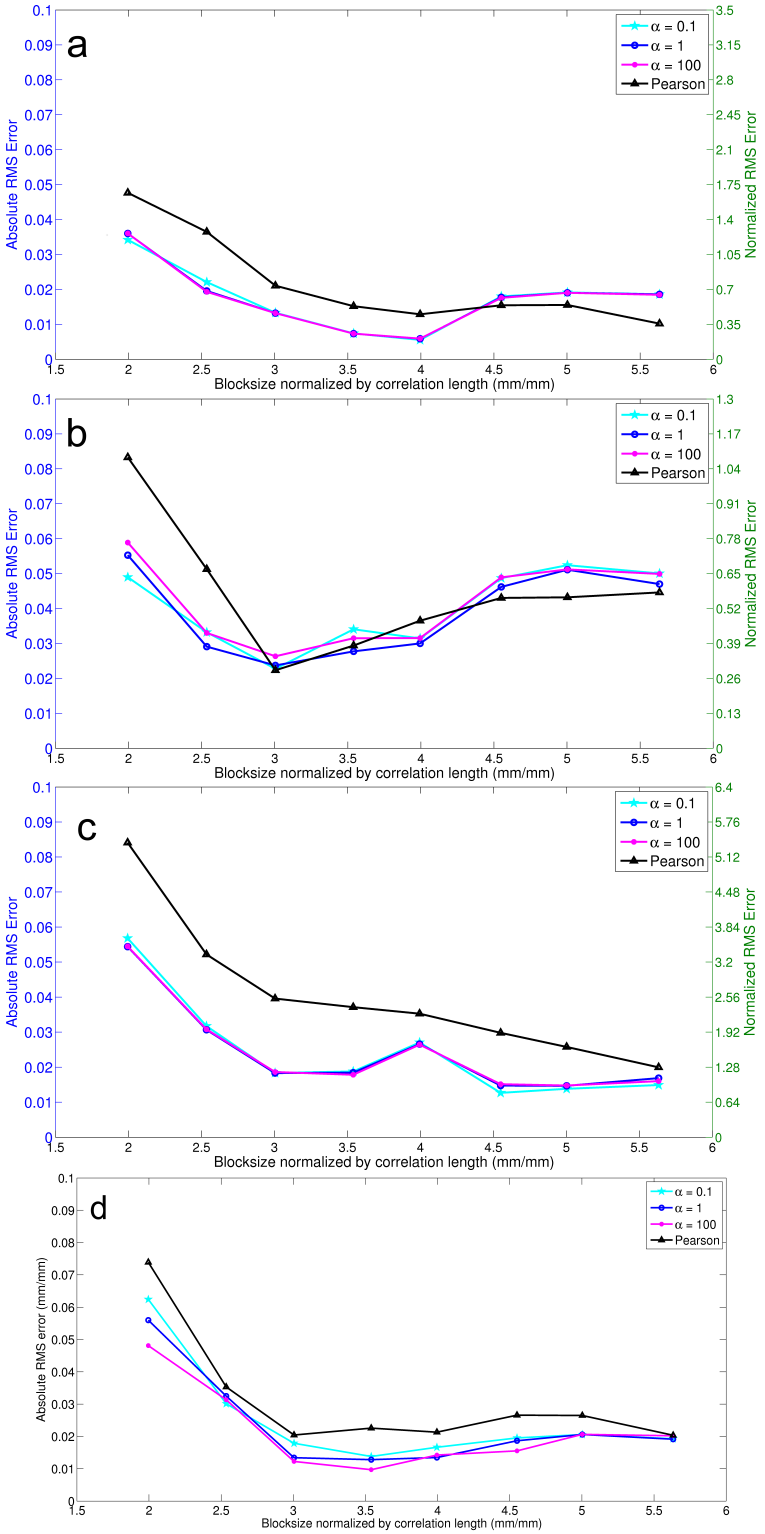

Figure 3.11: Plots of the RMS error as a function of the side length of sub-volume using the engineering strain (a), the component of the Green strain parallel to the fiber direction (b), perpendicular to the fiber direction (c), and in the shear direction (d). When possible, both the absolute RMS and the normalized RMS error are shown on the same plot.

Table 3.4: Levene and Kruskal-Wallis p values comparing mean and variance of strain errors from texture tracking using different sub-volume lengths

Strain type, direction	Correlation type	Kruskal	Levene
Engineering	Clocksin, $\alpha = 0.1$	**0.002**	0.146
Engineering	Clocksin, $\alpha = 1$	**0.004**	0.221
Engineering	Clocksin, $\alpha = 100$	**0.002**	0.218
Engineering	Pearson	0.355	0.467
Green, parallel	Clocksin, $\alpha = 0.1$	0.058	0.989
Green, parallel	Clocksin, $\alpha = 1$	0.073	0.803
Green, parallel	Clocksin, $\alpha = 100$	0.190	0.825
Green, parallel	Pearson	0.562	0.706
Green, perpendicular	Clocksin, $\alpha = 0.1$	0.932	**0.001**
Green, perpendicular	Clocksin, $\alpha = 1$	0.911	**0.005**
Green, perpendicular	Clocksin, $\alpha = 100$	0.779	**0.014**
Green, perpendicular	Pearson	0.841	**<0.001**
Green, shear	Clocksin, $\alpha = 0.1$	0.824	0.122
Green, shear	Clocksin, $\alpha = 1$	0.847	0.142
Green, shear	Clocksin, $\alpha = 100$	0.446	0.138
Green, shear	Pearson	0.768	0.161

strains computed using these estimators were not significantly different after correction for multiple comparisons. Scatter plots of strains calculated using the four likelihood functions for this sub-volume size are shown as a function of the sonomicrometry strains in Fig. 3.12.

At the sub-volume length with the least error for the engineering strain, 4 CL, a t-test confirmed that there was no significant difference between the means of the engineering strains calculated using the Clocksin likelihood no matter which value of α was used, though there was a significant difference between the strains calculated with the Clocksin likelihood compared to those calculated by the Pearson likelihood ($p = 0.044$ with $\alpha = 1$ and $p = 0.041$ with $\alpha = 100$) and a near-significant difference with $\alpha = 0.1$ ($p = 0.0505$). The Green strain in the parallel direction showed a significant difference between the Clocksin likelihood with $\alpha = 1$ and with $\alpha = 0.1$ ($p = 0.031$), while the Green strain in the shear direction showed a significant difference between the Clocksin likelihood with $\alpha = 0.1$ and the Pearson likelihood ($p = 0.034$).

The decorrelation measurements for the first experiment are shown in Fig. 3.13 (a) for both the first ten indentations and for all twenty indentations. The decorrelations had a very similar dependence on the indenter displacement, so it was assumed that using decorrelation from only the first ten indentation steps was sufficient to characterize decorrelation as a function of displacement for the entire experiment. The decorrelations, obtained using the first ten indentation steps from each experiment, for all four experiments are shown in Fig. 3.13 (b) along with the theoretical decorrelations obtained analytically.

Fig. 3.14 shows engineering strain error for the different sub-volume lengths for indentations ranging from 0.2 to 1.2 mm step sizes. At optimum sub-volume lengths (3–4 CL), accuracy in the engineering strain measurement was best for smaller indentation sizes and errors tended to increase with larger indentation sizes and larger amounts of decorrelation. At the smallest sub-volume size of 2 CL, normalized RMS strain errors ranged from 100% to 170% with no discernible pattern between error and indentation size. At the sub-volume

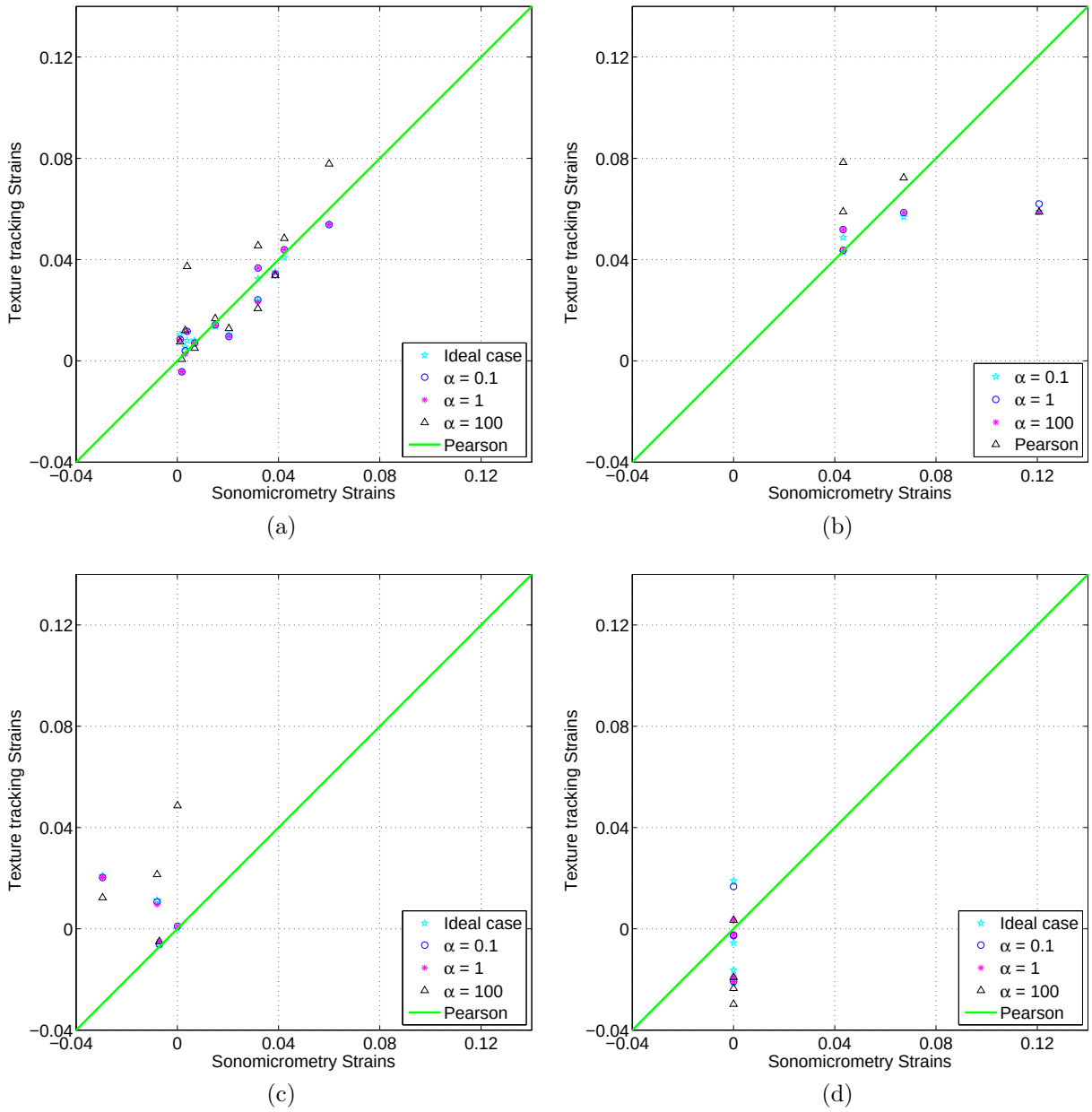

Figure 3.12: Scatter plots of estimated strains using a sub-volume length of 4 CL as a function of sonomicrometry strains using the engineering strain (a), the component of the Green strain parallel to the fiber direction (b), perpendicular to the fiber direction (c), and in the shear direction (d). The line of equal strain is plotted as the green diagonal in each panel.

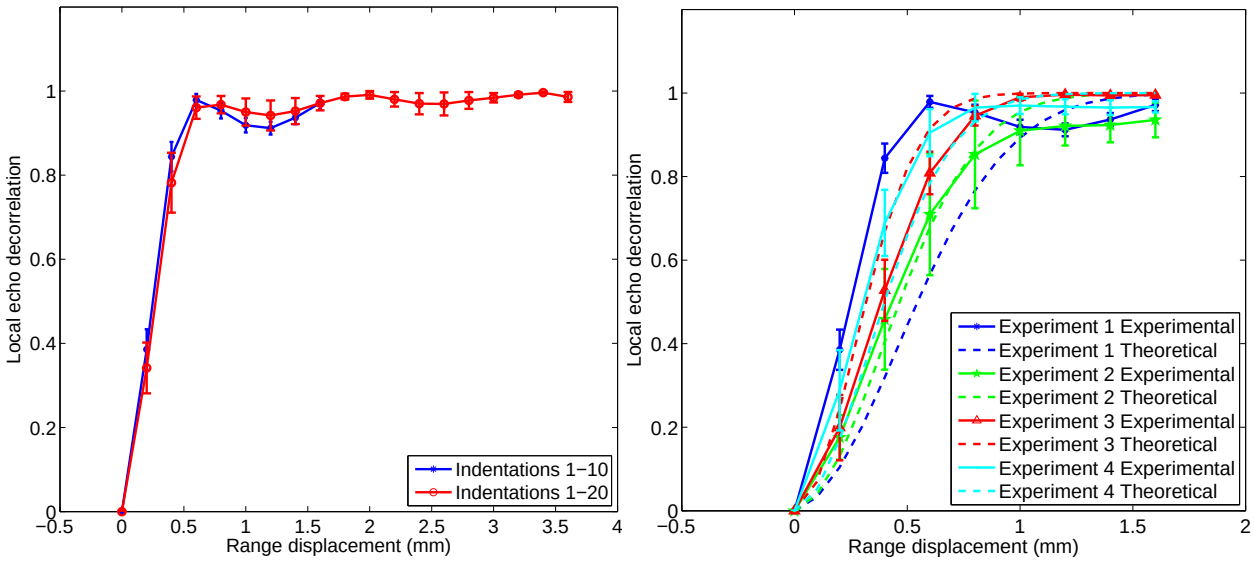

(a) (b)

Figure 3.13: Decorrelation measured as a function of displacement in the range direction. Panel a shows experimentally measured decorrelation for the first experiment in which the blue line is for data only from the first ten indentations while the red is for data from the entire experiment of twenty indentations. Panel b shows experimentally measured decorrelation for all four experiments for data from the first ten indentations with the theoretically calculated decorrelation plotted as dashed lines.

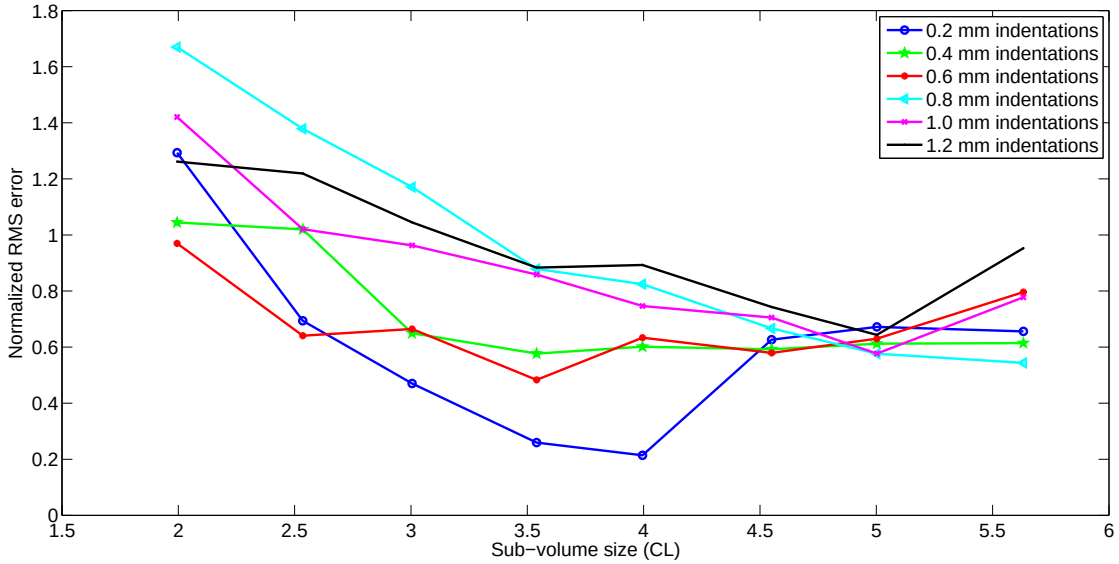

(a)

Figure 3.14: Plots of the normalized RMS strain error as a function of the side length of sub-volume using the engineering strain for indentations of 0.2, 0.4, 0.8, and 1 mm for α of 1 using the Clocksin likelihood.

size just above optimum, 5 CL, all indentations yielded nearly equivalent amounts of strain error with all results in the range of 60% to 70% again with no discernible pattern.

Fig. 3.15 shows the normalized RMS error for engineering strain with a sub-volume size of 4 CL for the three values of α used in the Clocksin likelihood and the Pearson likelihood as a function of indentation step size and decorrelation. At the optimum sub-volume size with the smallest indentation step size, the Clocksin likelihood performed best, but at slightly larger indentation steps, both likelihood functions gave very similar results, and at large indentation step sizes, the Pearson likelihood performed best. Fig. 3.16 shows the normalized RMS error as measured from the three measurements of engineering strain from each of the four experiments plotted separately, as decorrelation varied significantly between the different experiments. Decorrelation and indentation step size had a significant, positive correlation with each other ($r = 0.8745$, $p = 0.0226$). Strain error had a higher positive correlation with decorrelation ($r = 0.6744, p = 0.1418$) than with displacement ($r = 0.4190, p = 0.4083$),

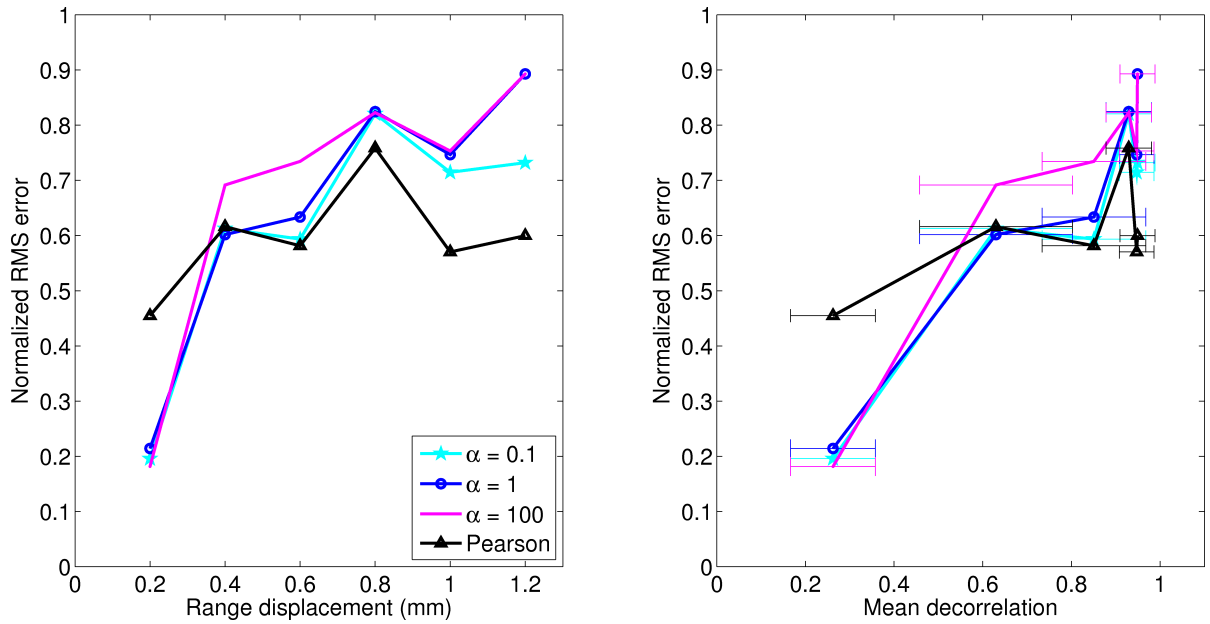

(a) (b)

Figure 3.15: Plots of the normalized RMS error with a sub-volume size of 4 CL as a function of (a) indentation size in terms of range displacement and (b) decorrelation. The decorrelation is averaged between the four experiments with horizontal error bars showing the standard deviation of those four values.

though neither was statistically significant.

3.4 Discussion

The goal of this work was to validate and optimize a texture tracking algorithm to measure strain in the PVM. Several versions of the texture tracking algorithm were implemented to estimate strains in 3D ultrasound images of an *ex vivo* PVM model, while sonomicrometry sensors provided an independent strain measurement. Strains measured in the PVM model were within the range of strains estimated for human PVM *in vivo* in the literature. In a study by Thyer et al. (2008), strain as measured by change in the urogenital hiatus circumference of women with PFD was found to have mean and standard deviation of -0.159 ± 0.084 during contraction and 0.227 ± 0.213 during Valsalva. A study by Siafarikas et al. (2015)

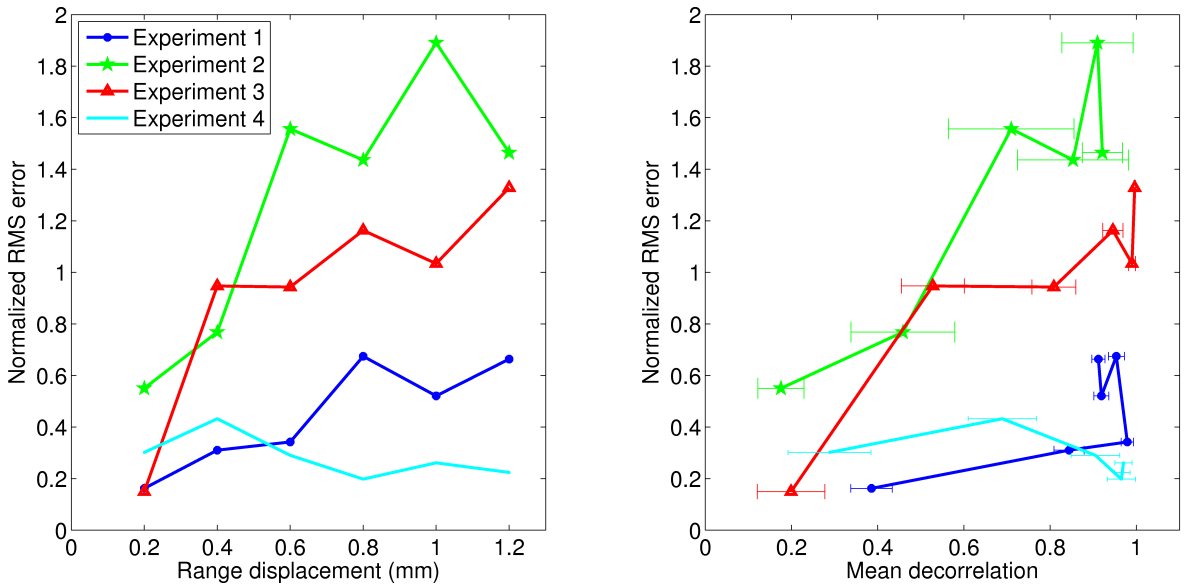

Figure 3.16: Plots of the normalized RMS error with a sub-volume size of 4 CL and α of 1 for all four experiments as a function of (a) indentation size in terms of range displacement and (b) decorrelation. The decorrelation is averaged between all possible combinations of image frames in each of the four experiments with horizontal error bars showing the standard deviation of those values.

used a similar method to find that levator ani strain in pregnant women at 21 weeks gestation had mean and standard deviation -0.1833 ± 0.0812 during contraction and 0.2081 ± 0.1806 during Valsalva for women who would go on to give birth without suffering a major LA injury. These somewhat exceeded the maximum strains seen in the present study. The Green strain measured in the PVM model in the fiber direction was similar to the magnitude of strain measured under contraction in women with a modified Oxford grade of 0 (no noticeable LA contraction under palpation), which was 0.088 ± 0.027 (Thyer et al., 2008).

The strains from maximum contraction and maximum Valsalva are expected to be larger than the strains seen in daily life. In a study by Weir et al. (2006), intra-abdominal pressure in women performing daily activities ranging from lifting an 8 lb weight from a counter to lifting a 35 lb weight from the floor showed a range of median pressures from 47.7 to 149.3 cm of H_2O which corresponds to an average strain of 0.0046 to 0.0348 in our study of cadaveric LA passively stretched in the fiber direction (Nagle et al., 2014) from chapter 2, which is lower than the strains seen in the PVM model used in this study. However, the women in the Weir et al. (2006) study would have been activating their levator ani muscles rather than allowing them to passively stretch.

To assess whether the texture tracking algorithm is sufficiently accurate to be clinically useful, strain data from Thyer et al. (2008) were compared for women with different scores on the modified Oxford grade scale, which quantifies strength of LA contractions. The mean PVM strain measured in women with a modified Oxford grade of four (those with the strongest LA contraction under palpation) was -0.25 under contraction and 0.14 under Valsalva, while with a modified Oxford grade of three (those with a moderate LA contraction under palpation), the mean PVM strain was -0.18 under contraction and 0.21 under Valsalva (Thyer et al., 2008). Thus, there was an absolute strain difference of 0.07 (28% normalized to the modified Oxford grade 4 strain) under contraction and 0.07 (50% normalized) under Valsalva between these two groups. At optimum settings, the texture tracking algorithm

measured engineering strain with absolute RMS error 0.006 (20% normalized), sufficiently accurate to differentiate between strains seen in these two groups of women.

The Clocksin exponential-sum likelihood was tested here with three values of the smoothing parameter α, 0.1, 1, and 100. In all the experiments analyzed, changing the value of the α parameter made little difference in the tracked displacements and strains. The function of this parameter is to smooth the likelihood map to lower the impact of outliers, but in these experiments, the likelihood maps were already fairly smooth and few outliers were seen. At the smallest indentation size (0.2 mm), in the first of the four experiments, the Pearson correlation yielded distinctly higher errors than the Clocksin likelihood with any value of α, though in the other three experiments, strain errors were similar. At the largest indentation size (1.2 mm), in two of the experiments, there were distinctly lower strain errors when the Pearson correlation was used, in one experiment, using the Pearson correlation resulted in higher strain errors, and one experiment showed nearly the same level of error no matter which correlation estimator was used.

The largest errors in strain estimation occurred for the smallest sub-volume sizes (2–2.5 CL). These sub-volumes may have not contained enough image information to be effectively tracked. Larger sub-volume sizes (4.5–5.5 CL) yielded slightly higher errors than optimally sized sub-volumes. This likely results from the assumption that the sub-volume moves as a rigid body, which breaks down for larger sub-volume sizes, resulting in decorrelation of the undeformed and deformed sub-volumes. In particular, sub-volumes in that size range would be large enough to include the edges of the muscle which is expected to be a large source of decorrelation when under strain. Errors in the smaller sub-volume sizes tended to be overestimates of strain, while errors in the larger sub-volume sizes tended to be underestimates of strain. In a future *in vivo* study, we expect that 3 CL may be the minimum size for a sub-volume to contain sufficient information to track and that the largest useful sub-volume would have dimensions just fitting within the muscle. Ophir et al. (1991) also found that

segments sized 4 mm resulted in the most reasonable images when measuring the elastic modulus of foam phantom materials and bacon.

When Clocksin et al. (2002) proposed the likelihood function used in this chapter, it was joined with a prior function that biased the displacement estimation towards small displacements to create a Bayesian strain estimator. However, when this prior function was added to the Clocksin likelihood function in this study, the prior term dominated, causing nearly all estimated displacements to be zero. While the Bayesian prior decreases the mapping parameter on the scale of only 5% of the maximum likelihood, the difference between the minimum likelihood in the search region and the maximum possible likelihood was only on the scale of 15% when α was 0.1, 2% when α was 1, less than 0.1% when α was 100, and 40% when the Pearson correlation was used. Attempts were made to scale the prior, but when the scale factor was low, the prior did not contribute at all to where the algorithm mapped the displacements and when the scale factor was high enough to allow the prior to contribute, the prior dominated the algorithm. Future work to optimize the prior would be beneficial. Use of a prior to bias displacement estimates based on the initial displacement sizes (Byram et al., 2013b) could prove effective in improving accuracy.

A limitation of this method of displacement calculation is that only displacements within a certain range can be precisely measured, consistent with previous observations on ultrasound elastography (Varghese and Ophir, 1997). In this method, displacements smaller than the voxel size cannot be calculated. To partially overcome this quantization issue here, a set of five points were tracked and their displacements averaged. In addition, images were interpolated in the elevational direction to enable smaller displacements to be tracked in that direction. Further interpolation in all directions could be used to track even smaller displacements, within limits imposed by finite spatial resolution. Céspedes et al. (1995) used parabolic and cosine interpolation of the likelihood map itself to improve the resolution of the displacements without the need to interpolate the images themselves.

A related issue is that large displacements are difficult to calculate due to decorrelation of the ultrasound signal (Hooi et al., 2015). Here, the large overall displacement was broken into a series of much smaller displacements as is commonly done (Gao et al., 1996). Larger step sizes were seen to result in increasingly higher errors. In an *in vivo* study, a series of incremental strains could be achieved by using a transvaginal balloon to provide small strains to the levator ani (Haridas et al., 2005). Alternatively, 4D ultrasound imaging of a patient performing a pelvic floor contraction or Valsalva maneuver could provide a sufficiently high frame rate that displacements between sequential image volumes remain small. Interestingly, the experiment with the highest amount of decorrelation at the minimum indentation size, experiment 1 in Fig. 3.16, did not have the largest error when the Clocksin likelihood was used, but did have the largest error when the Pearson likelihood was used.

Eq. 3.12 to calculate the theoretical decorrelation is only valid for small strains. The average tissue engineering strain at the end of the first ten indentations ranged from 0.01–0.03 which is expected to be sufficiently small for the equation to be valid, but the Green strain component in the fiber direction at the end of ten indentations ranged from 0.03–0.06. The experiment with the highest Green strain component in the fiber direction was also the experiment where the theoretically calculated decorrelation was significantly lower than the experimentally measured decorrelation (experiment 1 in Fig. 3.13). In the other three experiments, the Green strain in the fiber direction ranged from 0.03–0.05 and the theoretical decorrelation fell within the error bars of the experimental decorrelation. It may be that the assumption of small strains is only valid when the maximum strain in any direction is 0.05 or less.

Notably, the absolute RMS error in each direction had minima on the order of 0.01–0.02. This may correspond to the image resolution of approximately 0.2 mm, which is close to 1% of the distance between tracked locations. This error may have been a major contributor to the normalized RMS error of the Green strain in the cross-fiber and shear directions,

where strains were small. Nonetheless, normalized RMS errors were within acceptable levels for the engineering strain and for the Green strain in the fiber direction. When this algorithm is applied to *in vivo* studies, image-based measurements of strain along the fiber direction are expected to be the most meaningful. The imaged muscle geometry may be straightforwardly used to choose tracking locations appropriate to measure strain along the fiber direction. The algorithm is now considered validated and suitable for future *in vivo* image-based measurements of pelvic floor biomechanics, as will be presented in the next chapter.

Chapter IV

In Vivo Biomechanical Properties of the Pubovisceral Muscle in Asymptomatic Women and Women with Pelvic Floor Disorders

4.1 Introduction

40% of American women aged 60-79 and 54% of women 80 years old and older suffer from at least one pelvic floor disorder (PFD), which include urinary incontinence, fecal incontinence, and pelvic organ prolapse (Wu et al., 2014). The portion of the levator ani that arises from the pubic bone and attaches to the walls of the pelvic organs and the perineal body is known as the pubovisceral muscle (PVM) (Ashton-Miller and DeLancey, 2007). Changes in the biomechanical properties of the PVM in women often lead to urinary incontinence and to pelvic organ prolapse, as the PVM is responsible for closing the urogenital hiatus through which the urethra and vagina pass (Ashton-Miller and DeLancey, 2007). Many surgeries to correct PFD are unsuccessful, which is thought to be due to poor diagnostics (DeLancey, 2005; Dietz, 2010). A method to non-invasively measure the biomechanical properties of the PVM *in vivo* could provide information to allow early detection of pelvic

floor disorders, provide needed biomechanical properties for FEM modeling and surgical planning, and improve assessments of efficacy for PFD treatments.

There has been significant work on methods to use medical imaging modalities, such as ultrasound, defecation proctography, and MRI, in order to better understand the mechanisms of PFD (Ahmad et al., 2015). Ultrasound imaging is particularly useful in assessing stress urinary incontinence and levator ani function as it can visualize motion of the pelvic anatomy (Wieczorek et al., 2011). Several groups have measured strain in the *in vivo* PVM during maximal contraction and Valsalva using 3D translabial ultrasound. Thyer et al. (2008) imaged women with PFD to measure strain in the PVM as the normalized change in the urogenital hiatal circumference. Derpapas et al. (2012) measured strain in women with PFD as the normalized change in diameter of the hiatus. Siafarikas et al. (2015) measured strain in pregnant women without PFD as the normalized change in circumference of the hiatus. No method has been published to measure PVM strain on a regional basis.

There have been many techniques developed to track regional strain in images, and correlation-based techniques are particularly useful to track displacements larger than a few pixels (Chu et al., 1985). Pre- and post- displacement images are compared to find the location in the post-displacement image that maximizes local image correlation with the pre-displacement image (Clocksin et al., 2002). Sometimes a prior probability factor is added to bias the correlation-based estimator (Clocksin et al., 2002; Byram et al., 2013a). Gao et al. (1996) coined the term elastography to describe measurement of a tissue's elastic properties using any imaging modality and sonoelastography to describe elastic property measurements using ultrasound. To avoid decorrelation of the ultrasound signal due to the compression applied to the tissue, a series of small compressions can be applied incrementally and accumulated (Insana et al., 2000). These methods analyze the estimated displacement field to compute the modulus or strain for a wide range of applications (Insana et al., 2000).

The goal of this study was to investigate the feasibility of a method to quantify re-

gional biomechanical properties of the PVM in women with and without diagnosed PFD. This method uses three dimensional (3D) ultrasound images of the PVM under incremental deformations as inputs into the texture correlation algorithm described in Chapter 3 to measure regional displacements of the muscle. These displacements are used to calculate strain which is then related to the stress measured during deformation to measure the stiffness of the muscle. The null hypothesis is that the *in vivo* intra-abdominal pressure normalized by PVM strain is the same in women with diagnosed PFD as in non-symptomatic women. This information will allow better understanding of the mechanisms of incontinence in general and could be used to improve PFD treatments. It will also be useful for determining the constitutive behavior of the PVM and could be combined with the passive characteristics described in Chapter 2 to develop a material model that describes the active and passive biomechanics of the levator ani.

4.2 Materials and Methods

4.2.1 Imaging procedure

Six *in vivo* imaging experiments were performed in collaboration with the FemCare division of Procter & Gamble (P&G) at their Feminine Care research and design facility with Institutional Review Board (IRB) approval. Women were selected from P&G's list of panelists to include three women with no sign of any PFD and three women with diagnosed and problematic urinary incontinence and pelvic organ prolapse. To maintain anonymity, the data were stored under code numbers rather than names, and these code numbers were changed to be consecutive and in age order for the purpose of this chapter. As the goal was to investigate feasibility of the imaging procedure and texture tracking algorithm rather than to provide statistically significant samples, the women were chosen with no attempt to age match between the symptomatic and asymptomatic groups. The ages, vaginal par-

Table 4.1: Information on the six panelists. The parity indicates the number of vaginal births of each panelist; none had any pregnancies that did not result in a vaginal birth. The pelvic floor disorder (PFD) status indicates whether panelists had been diagnosed with stress urinary incontinence (SUI), urge urinary incontinence (UUI), and/or pelvic organ prolapse (POP).

Panelist number	Age (years)	Parity	PFD status
1	25	0	none
2	29	1	none
3	32	0	none
4	42	2	SUI, UUI, and POP
5	56	6	SUI, UUI, and POP
6	64	3	UUI and POP

ity, and PFD status of the panelists are summarized in Table 4.1. The imaging procedure was a modified version of a previous protocol published in Haridas et al. (2005) in which a transvaginal balloon was used to apply strain to the vaginal wall.

At the beginning of each of the six experiments, a new cylindrical balloon catheter (Via Biomedical, Maple Grove, MN) with medical Tygon tubing, as shown in Fig. 4.1, was soaked in disinfectant and then rinsed in saline. The balloon was then preconditioned by slowly inflating it with saline from a volume of 30 mL to 70 mL five times. At the minimum volume used in the study (35 mL), the balloon diameter was approximately 33 mm, and at maximum volume (50 mL), its diameter was approximately 40 mm. The balloon was placed on the exam chair at the level it was to be placed in the panelist. Its baseline pressure values were recorded by an inline Gould-Statham Model P23-ID pressure transducer (Ventura, CA) connected to a DA100C Biopac pressure transducer amplifier (Goleta, CA) and an IPS100C Biopac signal isolator as it was inflated by an automated syringe from 35 mL to 50 mL in 2.5 mL increments. At the initial volume of 35 mL, the pressure was zeroed and then for

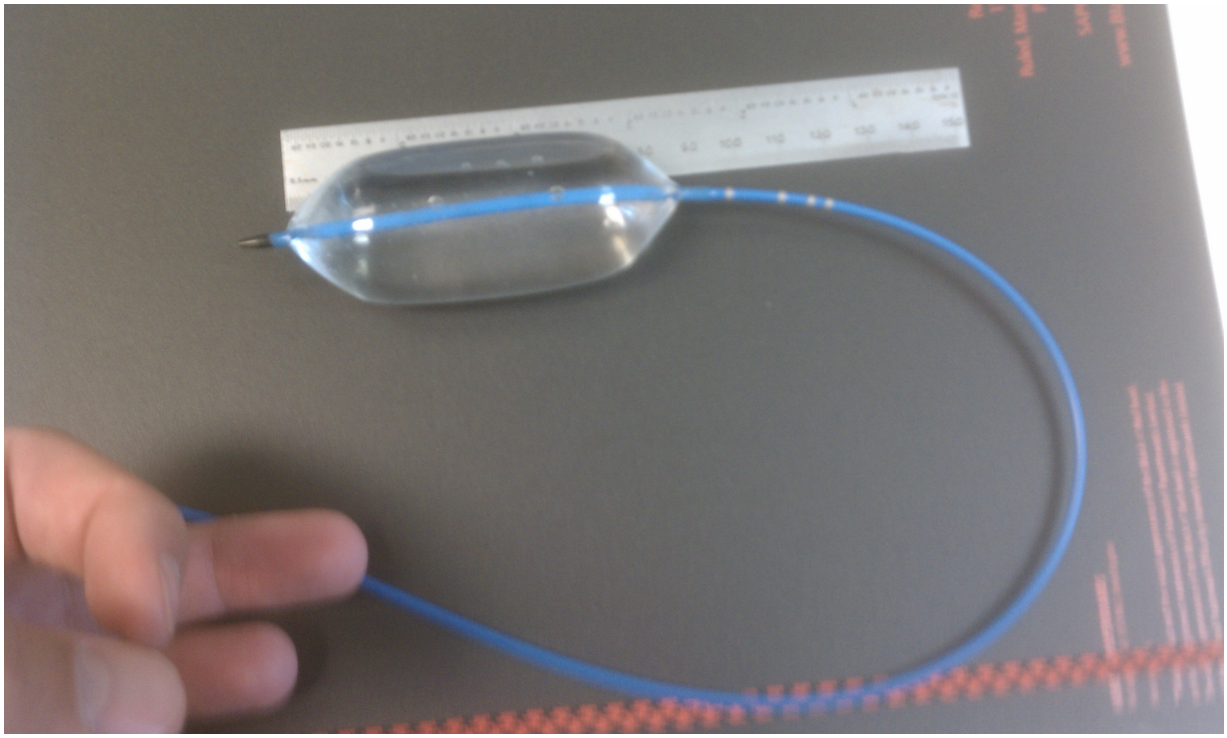

Figure 4.1: Balloon catheter used in the study.

each subsequent volume, pressure was recorded by an inline transducer after 30 seconds to allow any initial pressure fluctuations to dissipate.

With the balloon now ready for the procedure, the panelist voided and then lay in lithotomy position on the exam chair with the vagina parallel to the floor. The balloon, inflated to 35 mL, was placed within the vagina with its proximal end at the vaginal opening. The balloon's tubing was taped to the panelist's inner thigh to keep it in place during the procedure. A Voluson E8 system by GE Healthcare (Little Chalfont, Buckinghamshire, UK) was positioned next to the panelist. The transducer, in a mechanical positioning arm, was placed on the perineum and manually adjusted to allow a wide view of the pelvis (Fig. 4.2). Once in the desired location, the mechanical arm was tightened to keep the transducer stationary throughout the rest of the experiment. The pressure was zeroed and the balloon was inflated by automated syringe from 35 mL to 50 mL in 2.5 mL increments, as when it

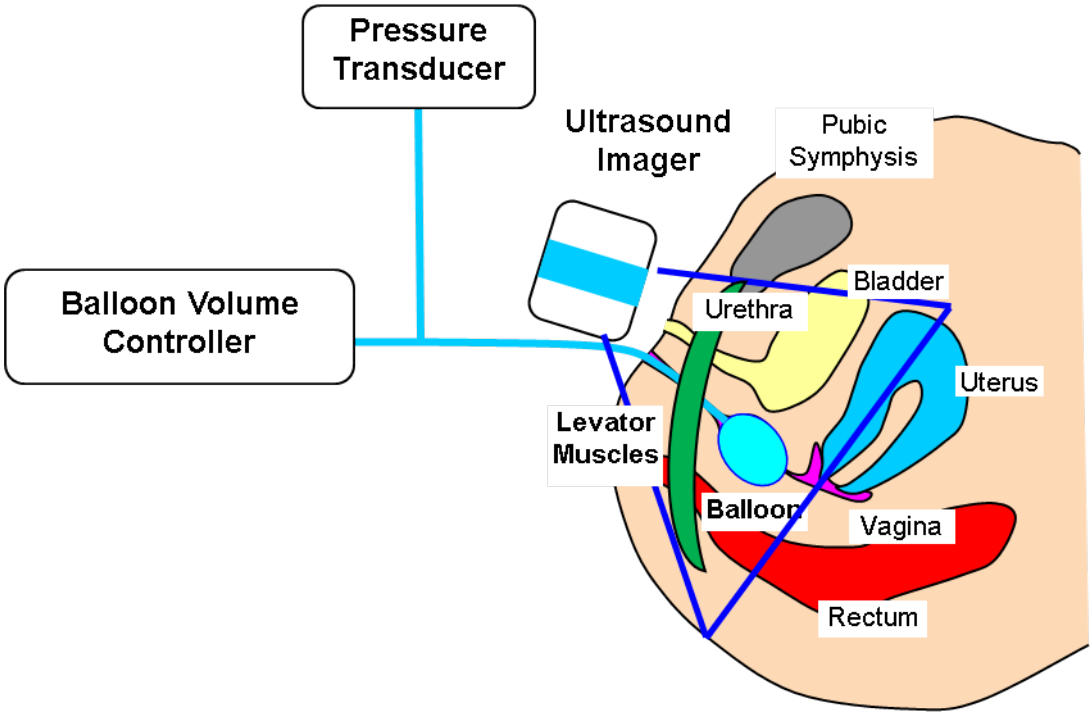

Figure 4.2: Diagram of *in vivo* set-up and cylindrical balloon catheter provided by Procter & Gamble.

had been outside the panelist. After each time the balloon was inflated to a new volume, the panelist breathed normally for thirty seconds, then held an exhale as a volumetric translabial ultrasound image was obtained using the Voluson scanner and the pressure was recorded. After recording an image at 50 mL, the balloon was returned to its initial pressure level. This procedure was then repeated twice to provide three runs of pressure and image data for each panelist.

4.2.2 Data analysis

The volumetric ultrasound images were saved in DICOM format, visualized using Avizo software (Visualization Sciences Group, Houston TX), and exported from Avizo as MATLAB-readable, volumetric data sets for deformation analysis with isotropic resolution in the range of 0.4–0.5 mm spanning a volume sized approximately 100 by 80 by 70 mm^3. The PVM was

located in the images in a manner described by Dietz et al. (2005). First, the mid-sagittal image plane was used to find the plane of minimal hiatal dimensions connecting the posterior aspect of the pubic symphysis and the anotectal muscularis, as seen in Fig. 4.3. The plane of maximal PVM thickness is usually 1–1.5 cm above this plane (Dietz et al., 2005). Axial planes in this area were used to measure the PVM thickness for simplicity and to align with the direction of balloon expansion. At every 1 mm over a span of 7 mm, the axial plane was visualized in Matlab and the width of the PVM at its midpoint on the right and left sides of the body was measured manually. The axial plane where the PVM was thickest was chosen as the initial location for the centers of sub-volumes to be tracked. Fig. 4.4 shows the mid-sagittal plane used to find the location of the PVM and Fig. 4.5 shows the axial plane where the PVM has maximum thickness.

To permit finer displacements to be calculated, the image was cropped to a volume sized approximately 60 by 30 by 70 mm^3 to exclude regions far from the PVM and interpolated in all directions using tesselation-based linear interpolation in MATLAB to increase the spatial resolution to a voxel size of 0.20–0.25 mm in each direction. This voxel size was similar to that of the *ex vivo* validation study described in Chapter 3. A cropped and interpolated axial plane is shown in Fig. 4.6.

The correlation length (CL) of the image in the region of the PVM was measured using the method described in section 3.2.3. The texture tracking algorithm, also described in section 3.2.3, was used with the Clocksin likelihood function with α set to 1 and a sub-volume size of 4 CL, as this had provided the best results in the *ex vivo* study. The search region was set to 1.8 times the size of the sub-volumes tracked. In the *ex vivo* study, smaller search regions were shown to be sufficient, but it was expected that displacements in the *in vivo* environment would likely be slightly larger. An example of a likelihood map can be seen in Fig. 4.7.

Five to eight points on each side of the PVM were chosen as trial sub-volume center

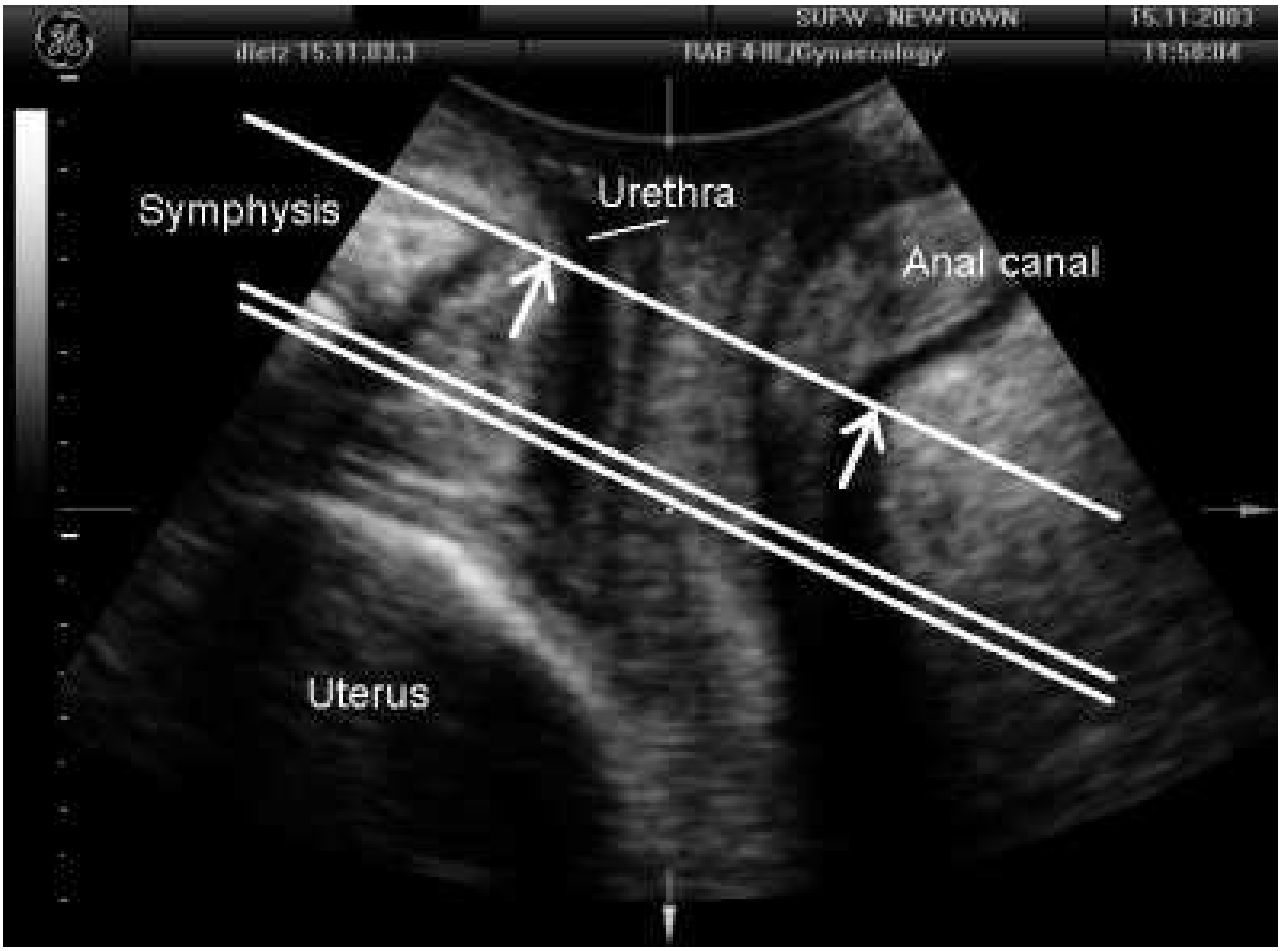

Figure 4.3: Mid-sagittal image from Dietz et al. (2005) demonstrating how to locate the PVM. The single white line represents the plane of minimal hiatal dimensions perpendicular to the plane shown. The double white line represents the plane at which the pubovisceral muscle has maximum thickness also perpendicular to the plane shown.

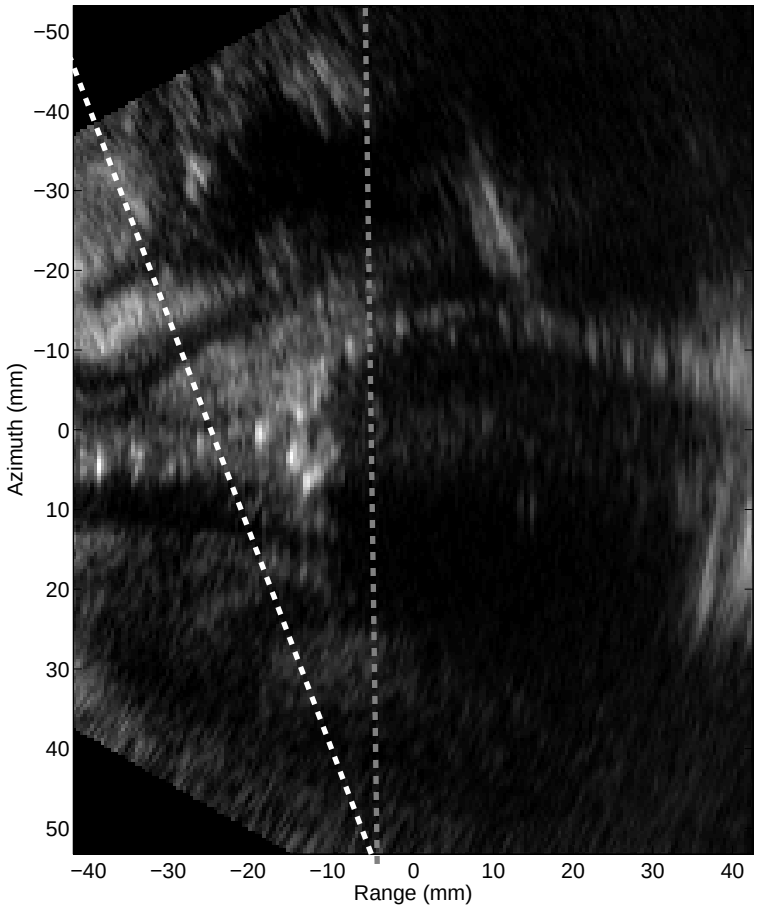

Figure 4.4: Mid-sagittal image from panelist 2. The white line represents the plane of minimal hiatal dimensions. The gray line represents the plane at which center points for the tracked sub-volumes were selected.

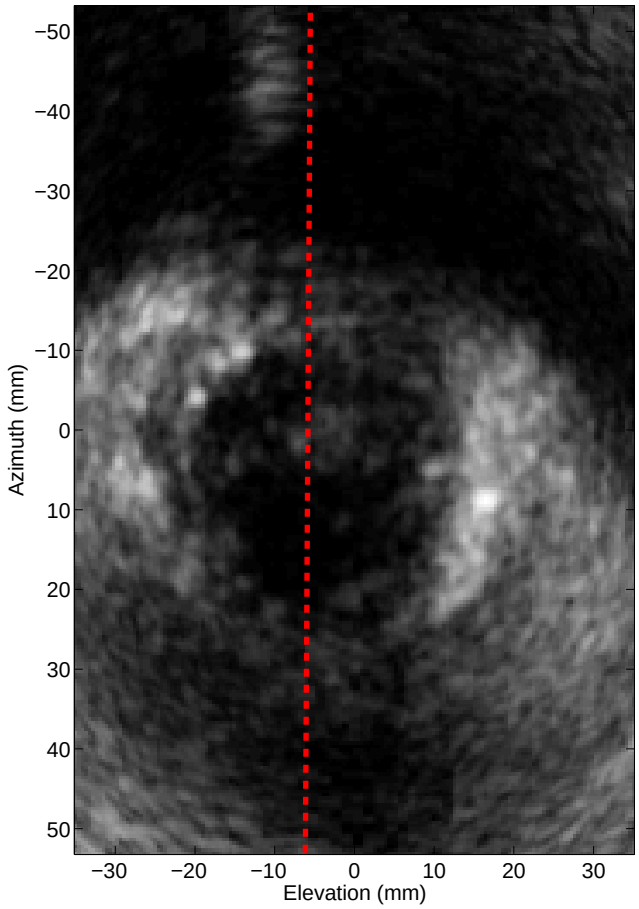

Figure 4.5: Axial image from panelist 2 corresponding to the gray line from Fig. 4.4. The red line represents the cross section shown in the previous image.

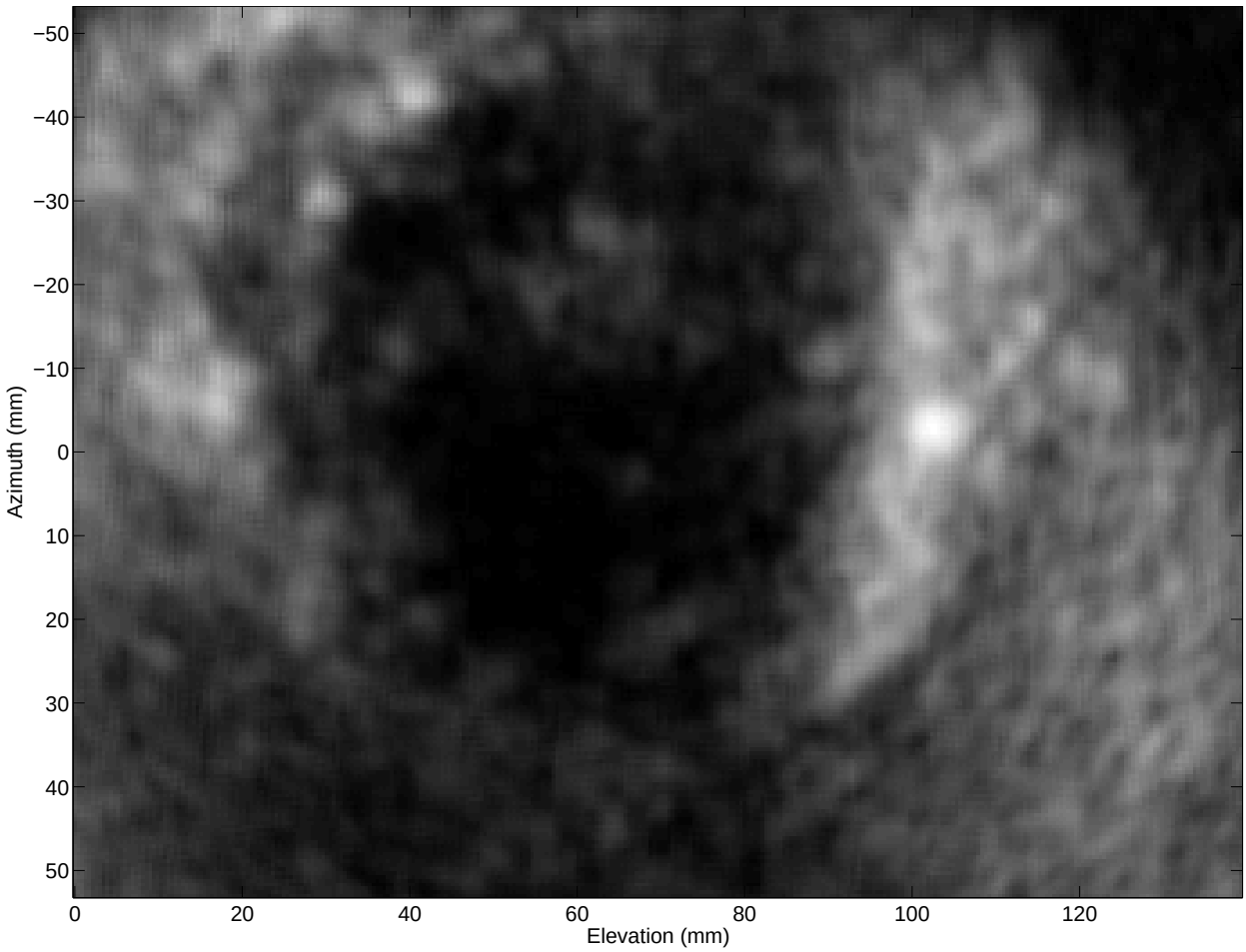

Figure 4.6: Axial image from panelist 2 corresponding to the gray line from Fig. 4.4 after being cropped and interpolated.

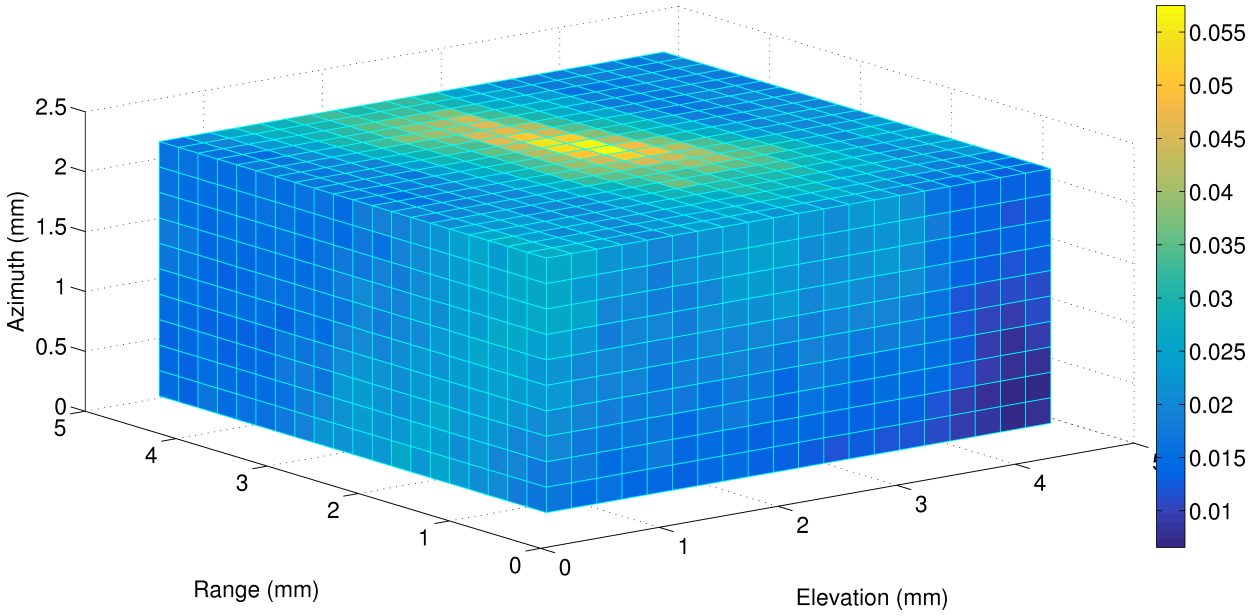

Figure 4.7: Middle cross section of a likelihood map using the Clocksin exponential sum likelihood with α set to 1 using volumetric images of panelist 1.

points to track in 3D, as seen in Fig. 4.8. The points were chosen 3 to 4 mm apart so that the sub-volumes around each point would not overlap, but the space between adjacent sub-volumes would be small. The output of the texture tracking, as seen in Fig. 4.9, was examined manually to select points on each side that moved in a direction consistent with the apparent direction of displacement as shown in Fig. 4.10. The displacements were examined in three dimensions, as seen in Fig. 4.11, to ensure that the out-of-plane components of the displacement were consistent with the other selected points. The out-of-plane displacement was expected to be small because the balloon expansion was nominally parallel to the elevation and azimuth directions. Points with out-of-plane displacements differing > 1 mm from the other points were removed from the strain calculations. The maximum likelihood was recorded for each displacement and examined to see if it would be useful as a filter for undesirable displacements.

Engineering strain, the normalized change in length between two points, was calculated two ways. First, strain was calculated in four regions of the PVM. The strain between

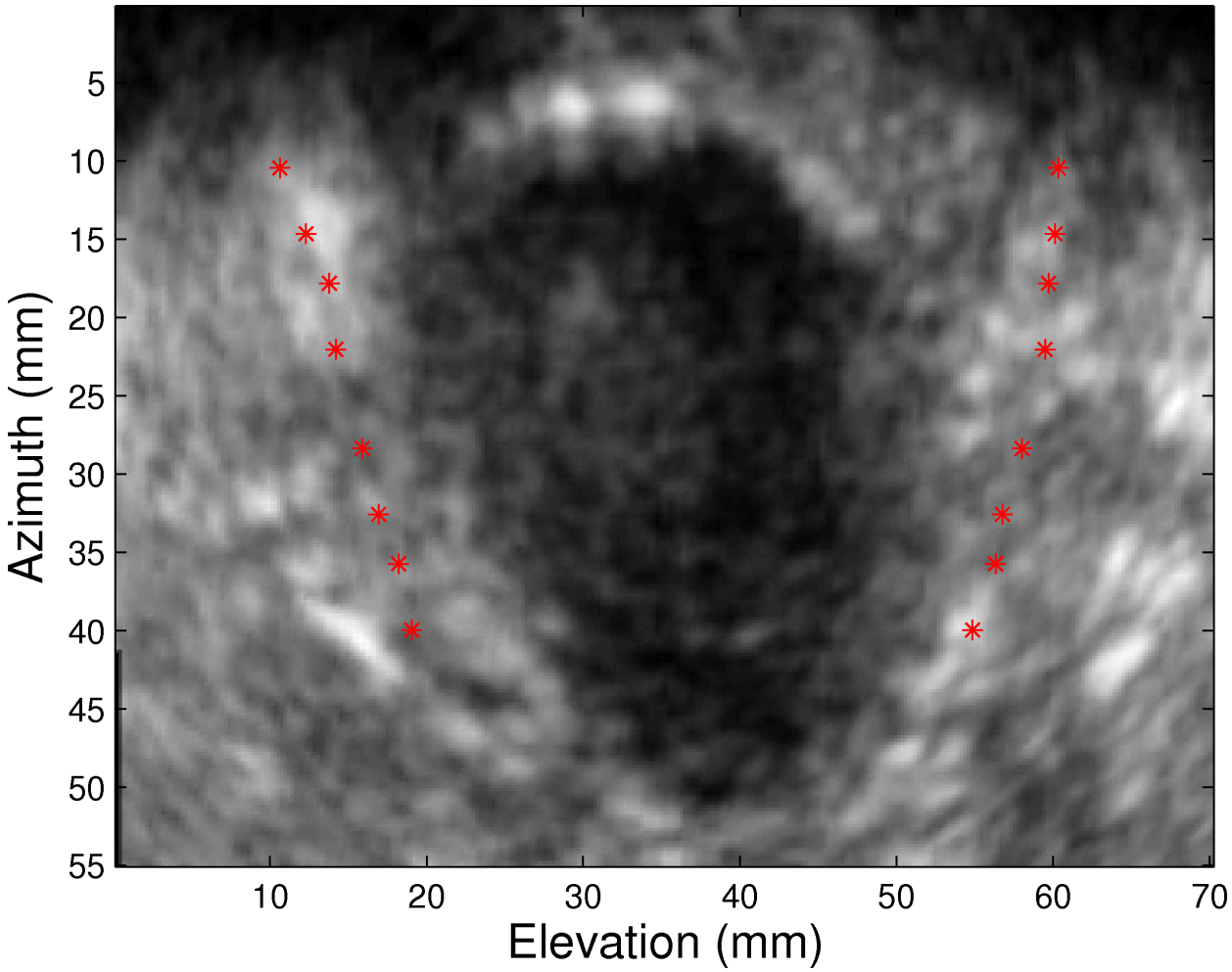

Figure 4.8: Initial axial image of panelist 4 with red points indicating center points of the sub-volumes to be tracked.

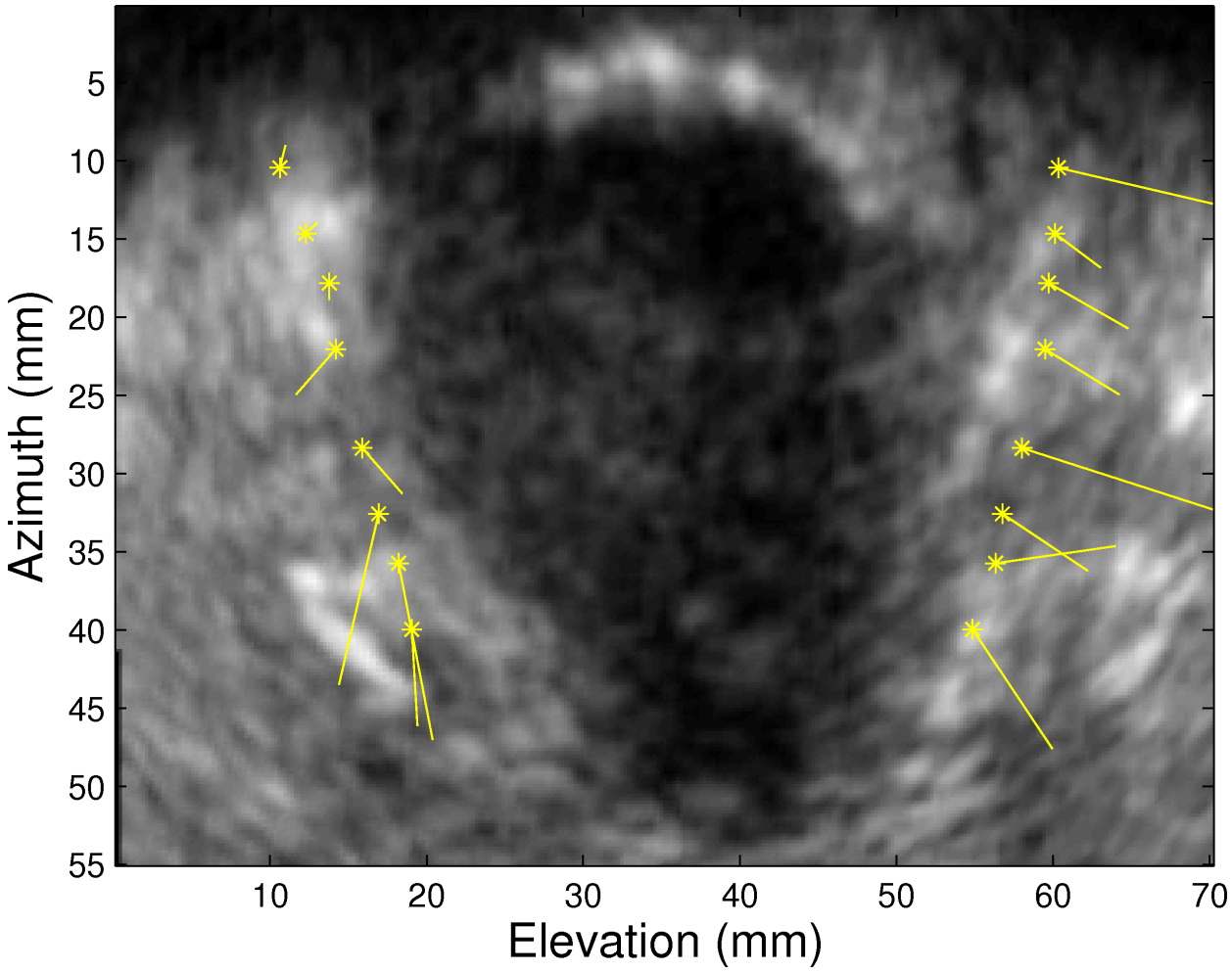

Figure 4.9: Final axial image of panelist 4 with yellow quivers indicating the directions of the tracked sub-volume center points. In this case, the PVM was large enough in the image to select eight points on each side to track.

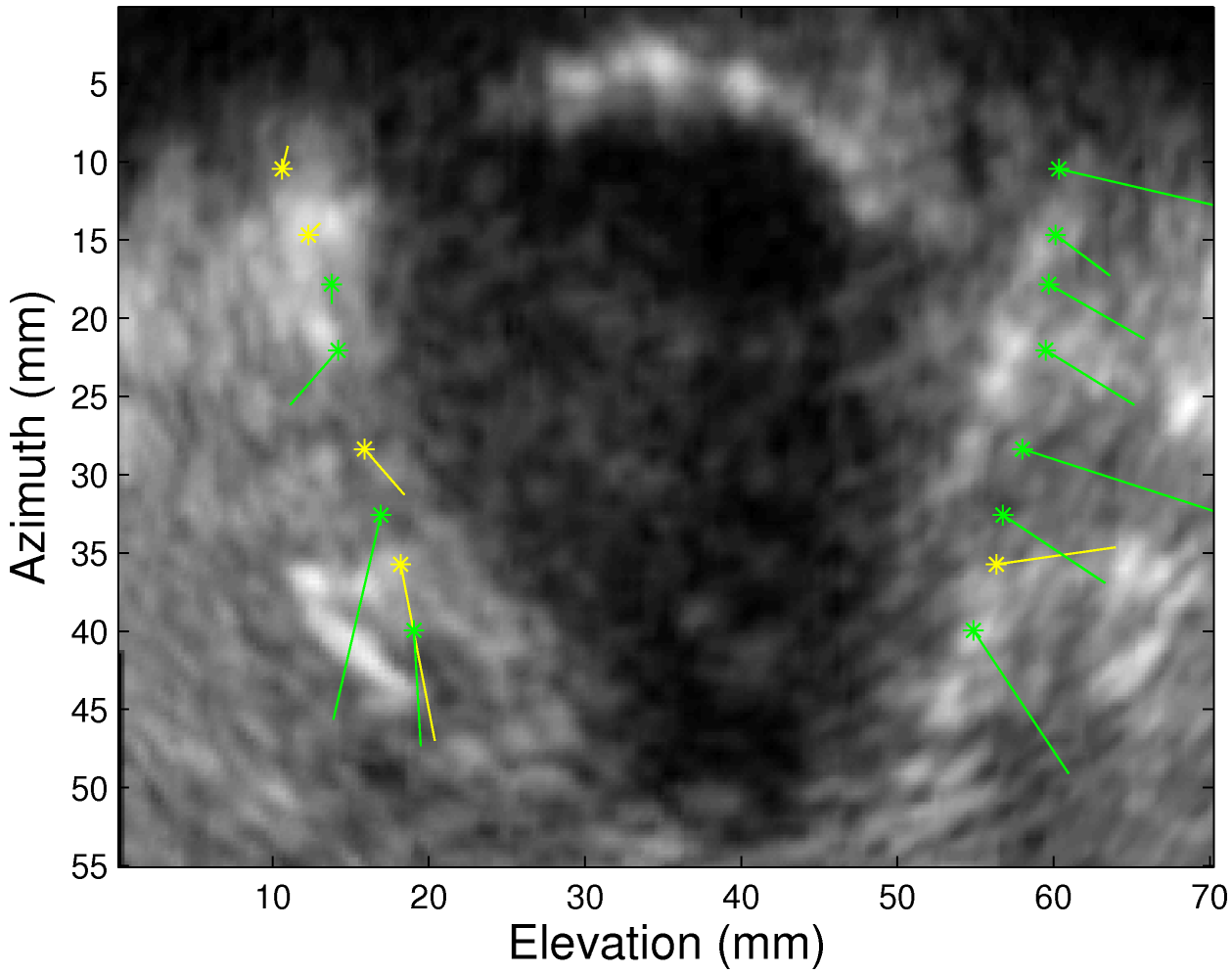

Figure 4.10: The image from Fig. 4.9 with points that moved in a direction consistent with the visualized direction of deformation shown in green. In this case, one strain was measured in the anterior right region of the PVM, two were measured in the posterior right, and three strains each were measured in the anterior left and posterior left regions of the PVM.

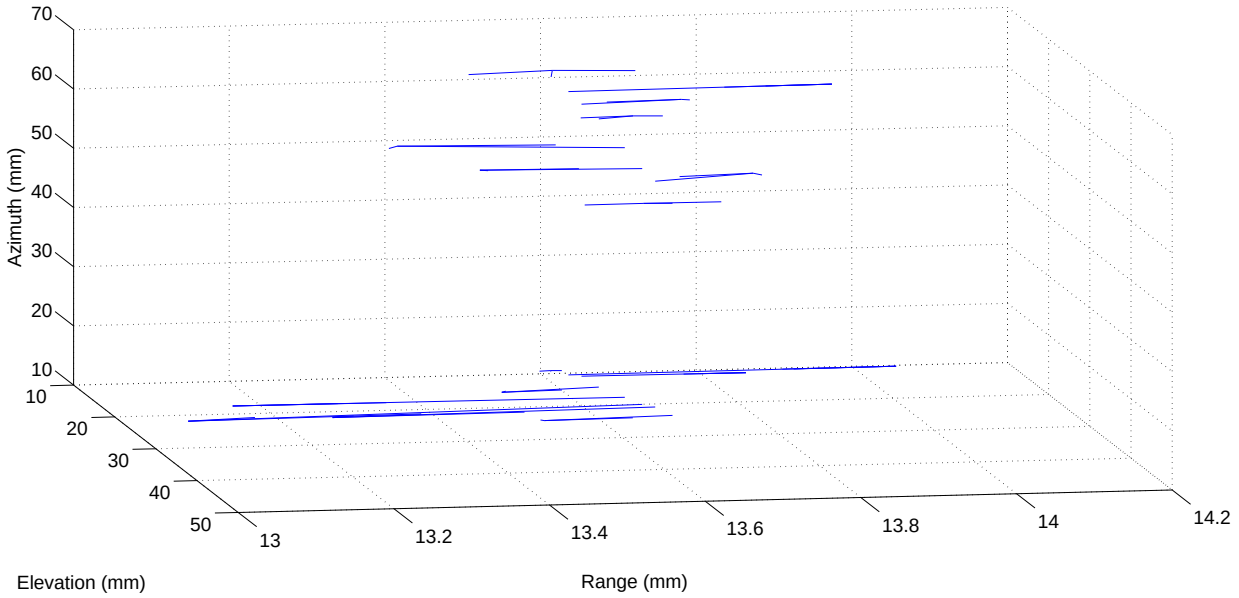

Figure 4.11: Three dimensional quiver plot of the displacement data shown in Fig. 4.9 angled to show the out-of-plane (range) direction.

adjacent points whose midpoint was within the top half of the PVM on the right side was used to compute strain in the anterior right PVM. If the midpoint was within the lower half of the PVM on the right side, the strain was considered to be in the posterior right PVM. Strains were calculated likewise on the left side for the anterior and posterior portions of the left PVM. When feasible, multiple strains were measured in each region, depending on the dimensions of the PVM and the number of points that could be tracked accurately. In order to compare strains from this study to those measured by Derpapas et al. (2012), strain was also calculated across the hiatus. The strain between the middlemost point on the right and the middlemost point on the left was considered to represent the strain across the hiatus.

Ideally, this would leave three runs for each panelist each with four regional strains for statistical analysis. However, in some cases the imaging window did not allow the PVM to be seen in all regions or damage to the PVM made strain too difficult to measure. Criteria for inclusion of strain data were that all points must be at least 4 mm from the edge of the initial image and that the PVM be without obvious damage in the region under consideration.

Intra-abdominal pressure can be estimated from the pressure inside of the balloon as

$$\Delta P_{\text{IAP}} = \Delta P_{\text{inside}} - c\Delta d, \tag{4.1}$$

where ΔP_{IAP} is the change in intra-abdominal pressure, ΔP_{inside} is the measured change in pressure inside of the balloon, c is the slope of an estimated linear pressure-diameter relationship for the balloon, and Δd is the change in balloon diameter inside the body. This approach is meant to correct the pressure measured inside the balloon for the portion of internal pressure used to overcome wall tension, leaving the amount of pressure transmitted to the body.

While the change in pressure of the balloon inside and outside the body was measured for all of the panelists, the balloon diameter outside the body was measured only for the first panelist and assumed to be similar for all of the balloons. The change in diameter inside the body was manually measured from the ultrasound images at the level of the PVM (Fig. 4.12). However, this could only be measured in ultrasound images where the balloon borders could be easily visualized. Because of these issues, the measured ΔP_{inside} was multiplied by the scale factor in Eq. 4.2 to obtain an estimate of intra-abdominal pressure:

$$\Delta \acute{P}_{\text{IAP}} = \Delta P_{\text{inside}} \left(1 - \frac{\overline{c}\overline{\Delta d}}{\overline{\Delta P_{\text{inside}}}}\right), \text{ where} \tag{4.2}$$

$$\overline{c} = \frac{\overline{\Delta P_{\text{outside}}}}{\Delta d_{\text{outside}}}, \tag{4.3}$$

$\Delta \acute{P}_{\text{IAP}}$ is the estimated intra-abdominal pressure, $\overline{c}$ is the average slope of the balloons' diameter-pressure relationships, $\overline{\Delta d}$ is the average change in balloon diameter from those images in which the balloon borders could be identified, and $\overline{\Delta P_{\text{inside}}}$ is the average change in pressure inside the body. The average slope of the balloon pressure-diameter relationship,

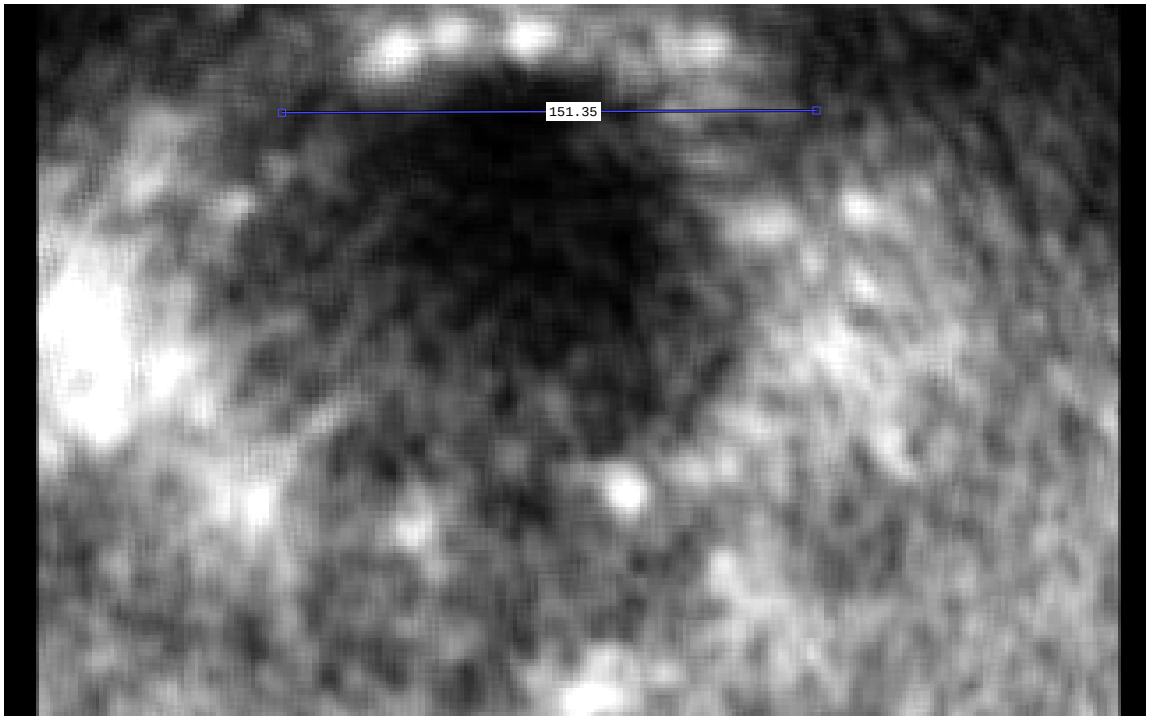

(a)

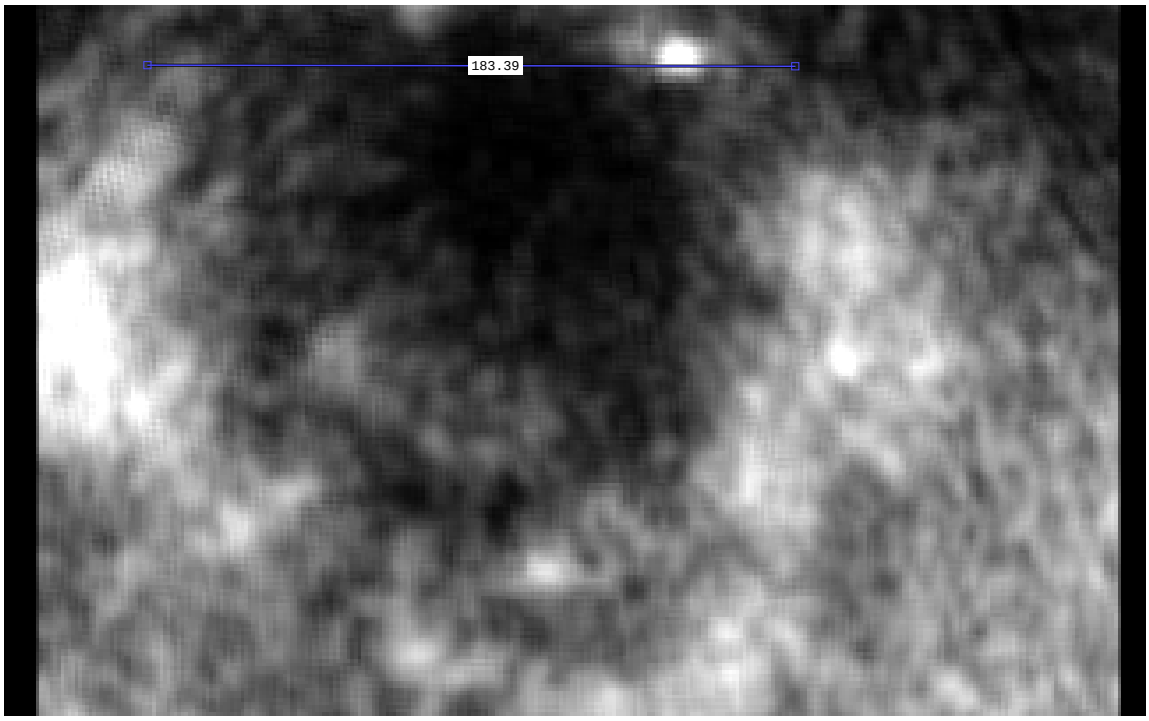

(b)

Figure 4.12: The initial (a) and final (b) axial images at the level of the tracked points from the first run of panelist 1 showing how the balloon diameter was measured manually. The length scale on each image is the distance of the balloon diameter in voxels. The resolution is 0.2037 mm per voxel.

$\bar{c}$, is calculated using $\Delta d_{\text{outside}}$ equal to the 7 mm increase measured for the *ex vivo* balloon diameter and the average change in balloon pressure outside the body $\overline{\Delta P_{\text{outside}}}$.

The estimated intra-abdominal pressure averaged over the three runs was divided by the strain (ϵ) averaged for all possible strains in each region over the three runs to provide a measure of stiffness for each region. Uncertainty for this quotient of means was calculated through error propagation:

$$\text{Uncertainty} = \frac{\text{mean}(\Delta \acute{P}_{\text{IAP}})}{\text{mean}(\epsilon)} \times \sqrt{\left(\frac{\text{std}(\Delta \acute{P}_{\text{IAP}})}{\text{mean}(\Delta \acute{P}_{\text{IAP}})}\right)^2 + \left(\frac{\text{std}(\epsilon)}{\text{mean}(\epsilon)}\right)^2}. \tag{4.4}$$

In MATLAB, two-tailed, paired t-tests compared stiffness from the anterior to the posterior regions and the left to the right sides of the PVM. Unpaired t-tests were used to compare the mean PVM stiffness, the $\Delta \acute{P}_{\text{IAP}}$, and PVM thickness between asymptomatic and symptomatic women. For the pressure comparison, the mean change in pressure over the three runs was used for each panelist and for the PVM thickness, the mean of both the left and right (when available) thickness over the three runs was used for each panelist.

4.3 Results

With three runs of data for each of the six panelists, this study had a total of 18 data sets in which to measure strain in the PVM. Due to image borders, the anterior right PVM could not be seen in five runs, the posterior right could not be seen in five runs, the anterior left could not be seen in one run, and the posterior left could not be seen in two runs. An example of a volumetric image in which only one side of the PVM could be visualized can be seen in Fig. 4.13. In one panelist, there was a large tear in the PVM on the right side, so that strain could not be measured in the right side locations, as can be seen in Fig. 4.14.

Balloon borders were clear enough to allow the diameter to be measured from both the

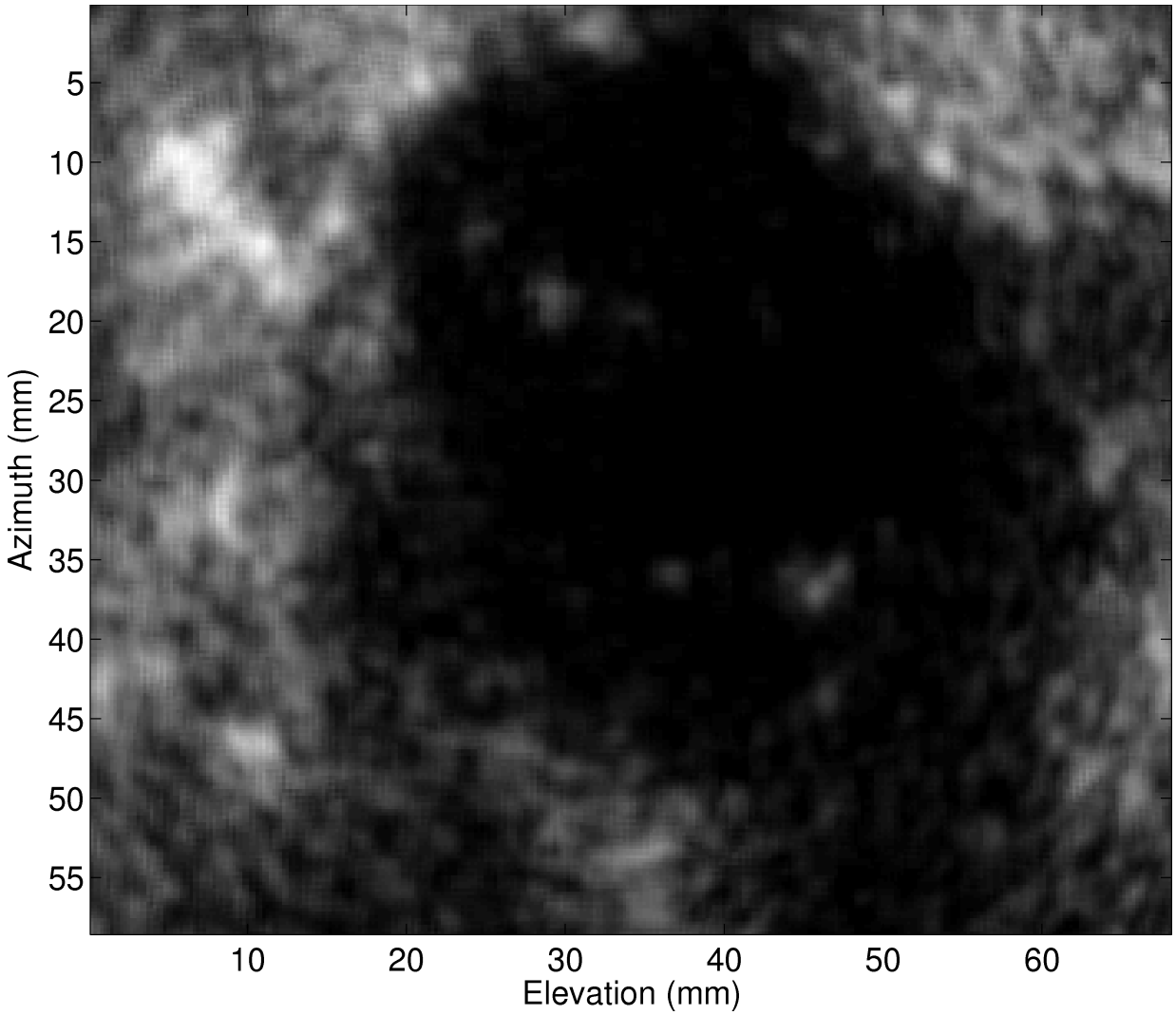

Figure 4.13: Initial axial image of panelist 5, in which the left side of the PVM could not be analyzed due to the image dimensions.

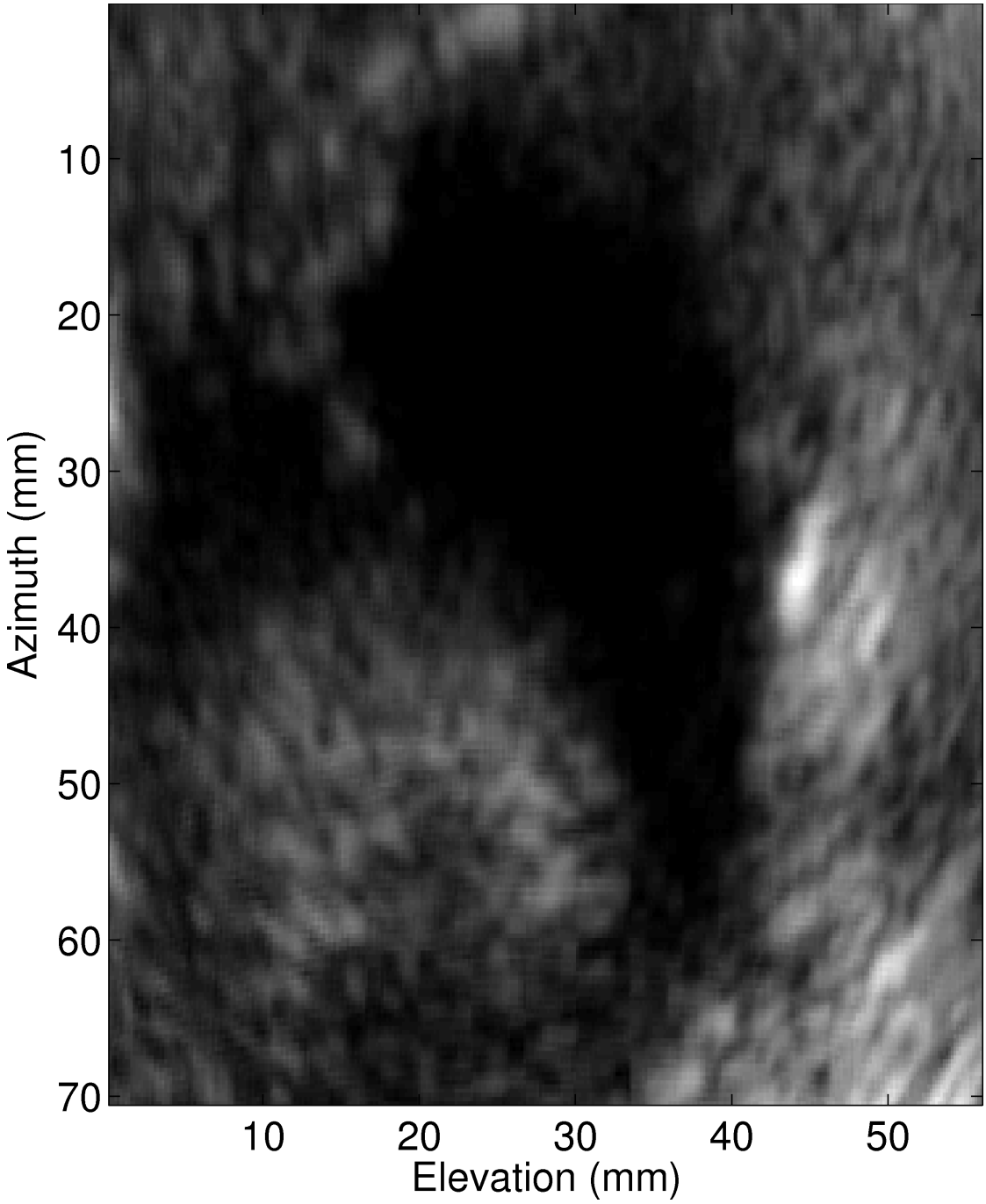

Figure 4.14: Initial axial image of panelist 6, in which the right side of the PVM could not be analyzed due to a visible tear in the tissue.

initial and final volumetric ultrasound images in 7 of the 18 runs. The initial diameters were used in Eq. 4.1 to confirm that the estimated initial intra-abdominal pressure was within the range of 0 to 1.8 kPa, the normal range IAP for a supine person who is not pregnant (Paramore, 1913; Chionh et al., 2006). The mean and standard deviation of the change in diameter was $\overline{\Delta d} = 4.57 \pm 0.71$ mm, in contrast to the 7 mm change in diameter seen outside the body.

The mean and standard deviation of change in balloon pressure outside the body for the 7 runs in which the balloon diameter could be measured was $\overline{\Delta P_{\text{outside}}} = 6.11 \pm 1.20$ kPa, only slightly smaller than the mean for all 18 runs of $\overline{\Delta P_{\text{outside}}} = 6.43 \pm 0.91$ kPa. The mean and standard deviation of change in balloon pressure inside the body for the 7 runs in which the balloon diameter could be measured was $\overline{\Delta P_{\text{inside}}} = 4.77 \pm 0.63$ kPa, which again was only slightly smaller than the mean for all 18 runs of $\overline{\Delta P_{\text{inside}}} = 5.39 \pm 0.73$ kPa. The values from the 7 runs were used in Eq. 4.2 to calculate $\overline{c} = 0.918$ kPa/mm and $\Delta \acute{P}_{\text{IAP}}/\Delta P_{\text{inside}} = 0.121$, which was then multiplied by each run's change in balloon pressure *in vivo* to obtain an estimate of intra-abdominal pressure.

Results from the strain, pressure, thickness, and stiffness measurements for each panelist are summarized in Table 4.2 and Figures 4.15 and 4.16. The results of the series of t-tests can be seen in Table 4.3. There were no significant differences between stiffness measurements from different locations nor between the different groups of panelists, as is expected for such a small sample size. The correlation coefficient between mean PVM stiffness and age was likewise not statistically significant ($r = 0.379, p = 0.459$). To determine the sample size of a future study using this protocol, a power study was performed in R (R Core Team, 2013) using the mean and standard deviation of the stiffness in asymptomatic women, 10.96 ± 4.93 kPa, and the mean stiffness in symptomatic women, 14.92 kPa. An independent sample study in a two tailed t-test with $\alpha = 0.05$ and power = 0.8 would require 25 asymptomatic women and 25 symptomatic women. The test comparing estimated change

in intra-abdominal pressure between asymptomatic women and symptomatic women found no significant difference, but the test comparing PVM thickness found that the PVM was significantly thicker in asymptomatic women than in symptomatic women.

Table 4.2: Measured and calculated pressure, strain, and stiffness results. The columns correspond to the panelist numbers from Table 4.1. The following symbols and terms are used to indicate the number of measurements used in each entry: ' for one, " for two, * for three, † for four, ‡ for five, and NA (not available) for none.

	Panelist 1	Panelist 2	Panelist 3	Panelist 4	Panelist 5	Panelist 6
Pressure (kPa, mean ± standard deviation)						
ΔP_{inside}	5.58 ± 0.06*	6.26 ± 0.09*	5.38 ± 0.08*	4.15 ± 0.19*	4.91 ± 0.07*	6.21 ± 0.11*
$\Delta \acute{P}_{\text{IAP}}$	0.67 ± 0.01*	0.76 ± 0.01*	0.65 ± 0.01*	0.50 ± 0.02*	0.59 ± 0.01*	0.75 ± 0.01*
PVM thickness (mm, mean ± standard deviation)						
Right side	8.30 ± 1.34*	7.71 ± 0.91*	NA	6.40 ± 0.66*	5.10 ± 0.60"	NA
Left side	8.78 ± 0.87*	7.37 ± 1.19*	7.38 ± 0.51*	6.36 ± 0.30*	4.31 ± 0.45"	4.69 ± 0.56*
Strain (mm/mm, mean ± standard deviation)						
Right ant	0.106 ± 0.015*	0.044 ± 0.046*	NA	0.041 ± 0.050†	0.103 ± 0.064"	NA
Right post	0.036 ± 0.006*	0.058 ± 0.037†	NA	0.065 ± 0.071†	0.026 ± 0.064"	NA
Left ant	0.159 ± 0.116*	0.058 ± 0.053†	0.054 ± 0.026*	0.027 ± 0.042‡	0.061'	0.060 ± 0.100*
Left post	0.121 ± 0.044*	0.103 ± 0.087†	0.054 ± 0.058*	0.021 ± 0.028†	0.037 ± 0.049"	0.081 ± 0.103†
Across hiatus	0.069 ± 0.010*	0.023 ± 0.014*	NA	0.031 ± 0.011*	0.042'	NA
Stiffness (kPa, quotient of means ± uncertainty)						
Right ant	4.8 ± 0.90	9.5 ± 19.14	NA	25.0 ± 14.92	5.7 ± 3.58	NA
Right post	13.8 ± 3.13	10.1 ± 8.32	NA	8.9 ± 8.43	8.5 ± 56.20	NA
Left ant	10.1 ± 3.09	17.6 ± 11.92	12.0 ± 12.93	11.1 ± 28.88	8.4 ± 21.25	25.9 ± 20.84
Left post	12.5 ± 4.01	6.6 ± 3.14	14.4 ± 5.80	8.6 ± 31.83	10.8 ± 2.84	10.9 ± 11.78
Across hiatus	11.0 ± 1.42	44.5 ± 20.02	NA	10.7 ± 5.78	11.9	NA

Table 4.3: Results of the t-tests comparing measurements from different locations and between the two groups of women. N is the number of measurements in each group.

Comparison	Test type	t statistic	p value	N
Left vs. right strain	Paired t-test	0.1962	0.8501	12
Anterior vs. posterior strain	Paired t-test	-0.9507	0.3666	12
Asymptomatic vs. symptomatic strain	Unpaired t-test	-1.5520	0.1381	12
Asymptomatic vs. symptomatic $\Delta\acute{P}_{\mathrm{IAP}}$	Unpaired t-test	0.8774	0.4728	3
Asymptomatic vs. symptomatic PVM thickness	Unpaired t-test	12.5609	0.0063	6

4.4 Discussion

The purpose of this study was to show feasibility and to establish a protocol for a method to measure regional strain and pressure of the *in vivo* PVM in women. The PVM was deformed in incremental steps by a catheterized balloon while measuring pressure and taking volumetric ultrasound images from which intra-abdominal stress and regional PVM strain were estimated. While we have shown that this is feasible, there is room for improvement in the protocol. Improvements include how the balloon's characteristics are measured, how the balloon is placed and deformed within the body, how the ultrasound transducer is set up, and how the texture tracking algorithm functions. Before a larger study is conducted, work should be done to address these issues to improve accuracy and repeatability.

When the baseline pressure and volume of the balloon were measured *ex vivo*, we failed to also record the diameter in the intermediate steps. This means there are inaccuracies in the assumed relationship between balloon diameter and its wall tension. We have modeled it assuming a linear relationship, but the relationship may follow a more complex hyperelastic material model. When the balloon's pressure is measured *ex vivo* before the start of each experiment, the diameter should be measured at each volume as well. If this were done, the relationship between diameter and pressure could be better quantified in case it is not

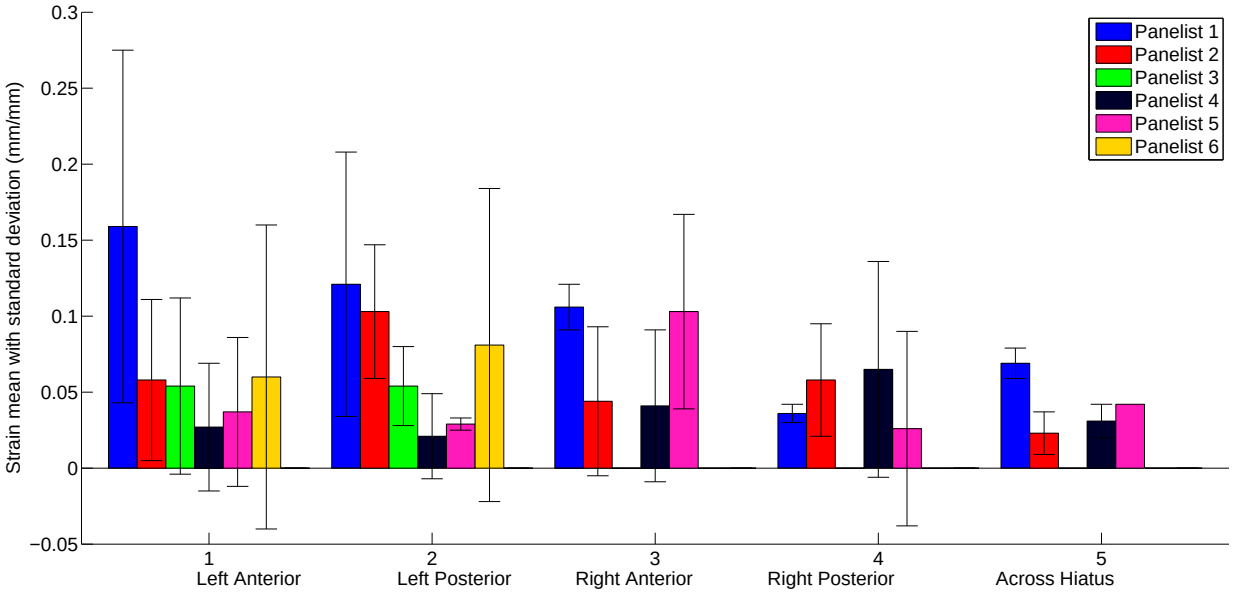

(a)

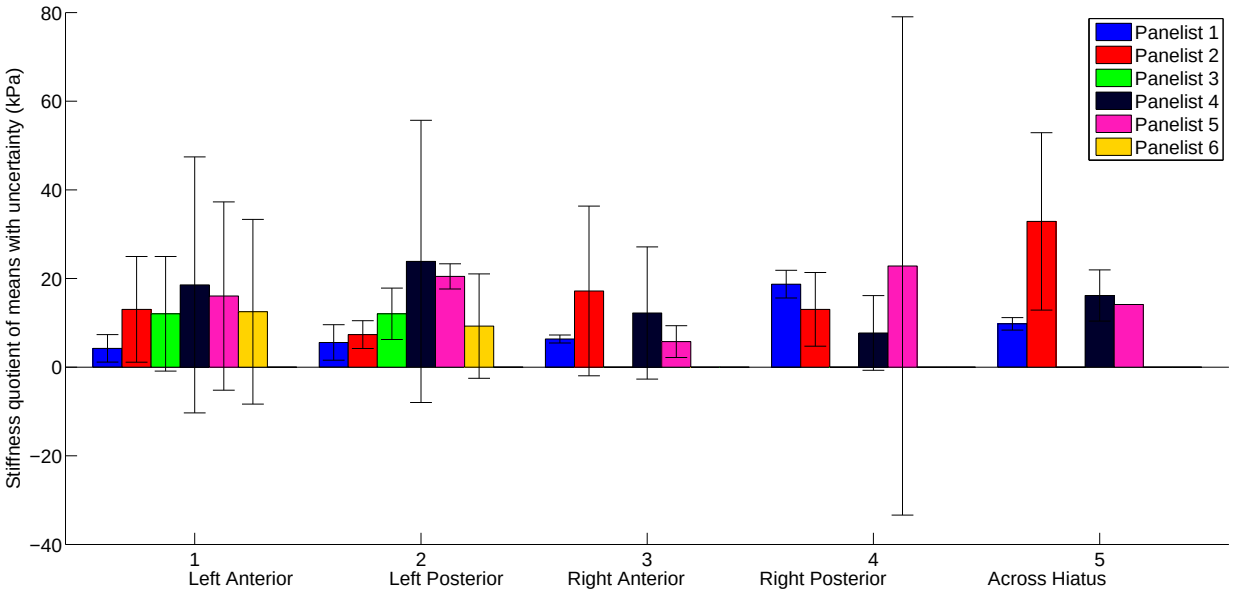

(b)

Figure 4.15: Bar plot of mean and standard deviation of the regional strain (a) and regional stiffness with uncertainty (b) estimations for each panelist.

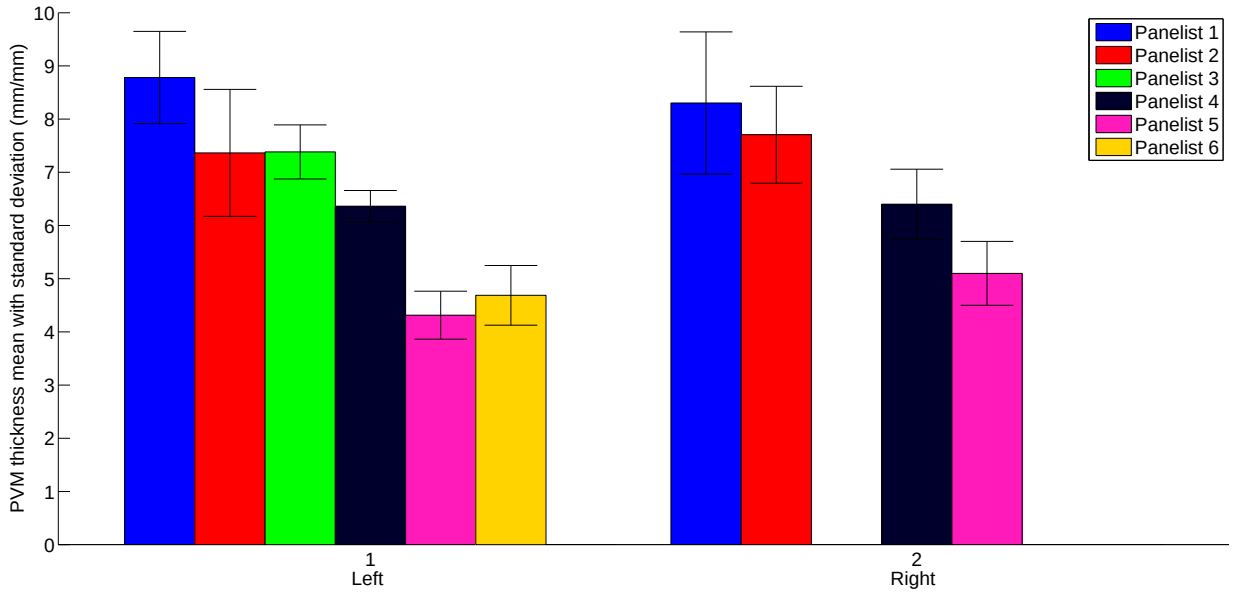

Figure 4.16: Bar plot of mean and standard deviation of the PVM thickness estimations for each panelist on each side of the body.

perfectly linear. Another source of inaccuracy is measuring the balloon diameter from the *in vivo* images, as the balloon borders are not always clear. With a more precise balloon diameter measurement at each step, we could make a full stress-strain curve that could have a constitutive model fit to it.

Some of the volumetric images were not wide enough in the elevation direction, so that the PVM was too close to an image border. The transducer was positioned using the mid-sagittal image as the main guide, so it was not clear at the time of imaging that this was an issue. In future studies, the axial view should be examined as well to ensure that the image shows the full width of the PVM. Although the balloon was meant to be placed with its proximal end at the vaginal opening, in many cases the balloon's proximal end was further inside the body. Because of this, the plane at which points were tracked, in which the PVM was thickest, the balloon was not always at its full diameter. More effort to ensure that the balloon is kept at the end of the vagina could eliminate this issue.

Variability in strains over the three runs for each panelist was fairly high, with coefficients

of variance greater than 50% in the majority of cases. Some of this may be due to natural differences within each panelist from run to run, but much may also be due to issues with the texture tracking algorithm. The fact that tracked points sometimes moved opposite to the balloon deformation shows that the method could use refinement. Work remains to improve methods of detecting and fixing points that do not track accurately. Currently, points were manually selected based on direction of displacement, but that should be automated in the future. The value of the likelihood parameter was investigated as a method to choose which points were least reliable, but this led to discarding points that seemed to track accurately yet allowed some points that clearly tracked poorly to remain. While the prior proposed by Clocksin et al. (2002) was shown to be unhelpful in Chapter 3, a more complex prior that takes into account the magnitude and direction of strain could make it unnecessary to manually choose the points that would be used to determine strain. Ideally, points would not have to be discarded, but would be replaced by better displacement estimations through the use of a well structured prior.

The texture tracking algorithm had been validated on an *ex vivo* model of the PVM as previously described in Chapter 3. The magnitude of final strains was similar between the two studies: the mean strain in the fiber direction in the *ex vivo* study was 0.069 ± 0.037 and the mean strain along the PVM in this study was 0.054 ± 0.042. However, the final strain was reached in 16–24 steps in the *ex vivo* study, which is about 3–4 times the six steps used in this protocol. When the data from the *ex vivo* PVM model were analyzed using a step size similar to that used in the *in vivo* study, the normalized strain error of the texture tracking increased to 60%, well above the 20% strain error from the smallest displacement size. 4D ultrasound imaging can obtain four or more volumes per second without compromising image quality (Dietz, 2010), so that may be a preferable method to obtain smaller increments of strain in future *in vivo* studies.

The level of correlation calculated between images was much smaller than in the *ex vivo*

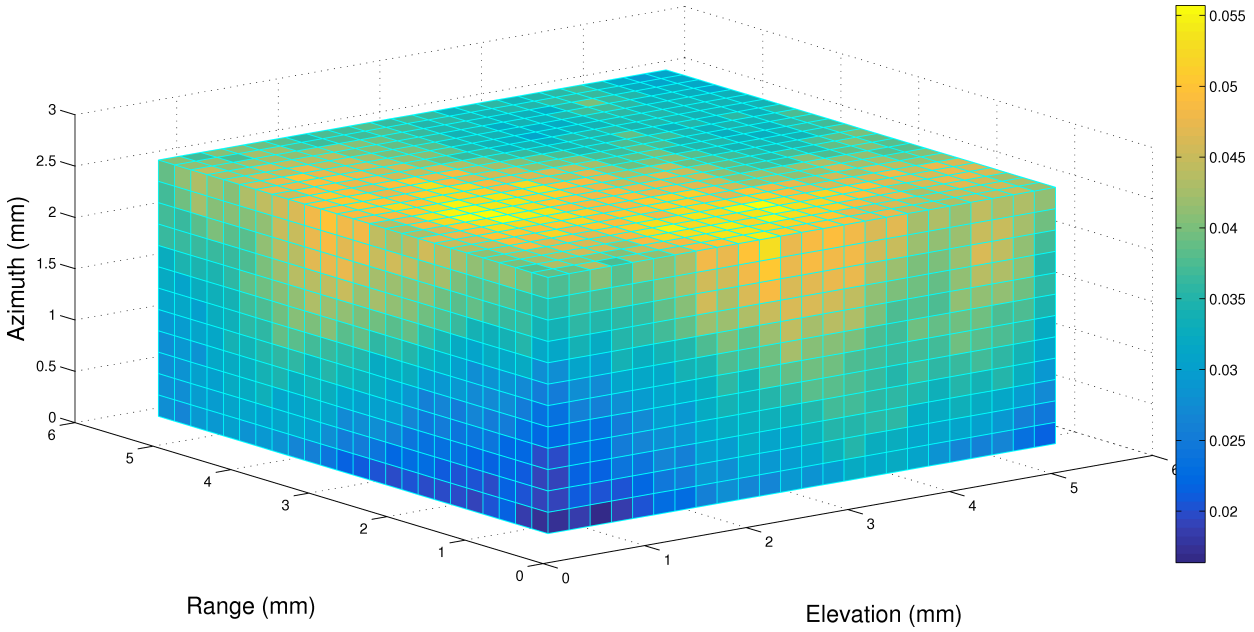

Figure 4.17: Middle cross section of a likelihood map using the Clocksin exponential sum likelihood with α set to 1 using volumetric images of panelist 5.

validation study. For two images separated by a similar displacement, the *ex vivo* study typically had maximum Pearson correlation coefficients in the range 0.8–1 and maximum Clocksin correlations in the range 0.96–1, while in the *in vivo* study, the maximum Pearson correlation coefficients were in the range of 0.6–0.9 and the maximum Clocksin correlations were in the range of 0.04–0.12. Some of the likelihood maps themselves did not have a single clear peak, an example of which can be seen in Fig. 4.17. This is due to the texture within the image at those locations lacking well defined features in certain directions. The use of a prior that takes direction and magnitude into account would be useful in these cases.

Many parameters of the PVM are important to consider for use in diagnosing and better understanding pelvic floor disorders. In this study, PVM stiffness and change in intra-abdominal pressure did not have significant differences between the symptomatic and asymptomatic groups, but the PVM thickness did. Other parameters, such as boundary conditions of the PVM, have not yet been measured to our knowledge, but may be of high importance.

The results of the study suggest that PVM stiffness may be similar between women with and without pelvic floor disorders but that PVM thickness is not, so thickness measurement may be more a more useful parameter for diagnosis purposes. Perhaps a slight increase in PVM stiffness occurs in women with PFD to compensate for muscle atrophy. Further studies with larger populations, including women with intermediate stages of PFD, will be necessary to investigate the importance of these PVM parameters.

Dimensions of the PVM including thickness, perimeter length, and the hiatus diameter have been measured by other groups (Dietz et al., 2005; Yang et al., 2006). Their PVM thickness measurements on women without pelvic floor disorders were similar to those in the present study: Dietz et al. (2005) measured a mean and standard deviation of PVM thickness of 0.73 ± 0.16 cm in 52 women aged 18-24, Yang et al. (2006) measured 0.84 ± 0.17 cm in women aged 19-38, and we measured 0.79 ± 0.62 in women aged 25-32.

Derpapas et al. (2012) calculated PVM strain with increasing pressures of the Valsalva maneuver in women with PFD. If the line from their data, shown in Fig. 4.18, were extrapolated to the mean intra-abdominal pressure used in this study of 0.65 kPa (approximately 6.6 cm H_20), it would be associated with a strain of 0.07, which is only slightly higher than the mean strain measured across the hiatus in this study of 0.04 for the women with PFD. This strain is representative of the deformation of the vagina, urethra, and other soft tissues in the urogenital hiatus rather than the PVM itself, but there is no published PVM strain measured similarly in human subjects to compare to the results of this study.

In the results of Chapter 2 on *ex vivo* LA biomechanics (Fig. 2.9), the mean LA strain at 0.65 kPa (0.00065 MPa) was only 0.006, which is an order of magnitude smaller than the mean PVM strain seen in this study of 0.07. However, it is inappropriate to compare the results of the two studies directly. The direction of force and extension were along the fiber direction in the *ex vivo* case, which is a simpler situation than the circular force in the *in vivo* study, where the LA was both compressed and extended. To get the true stress-strain

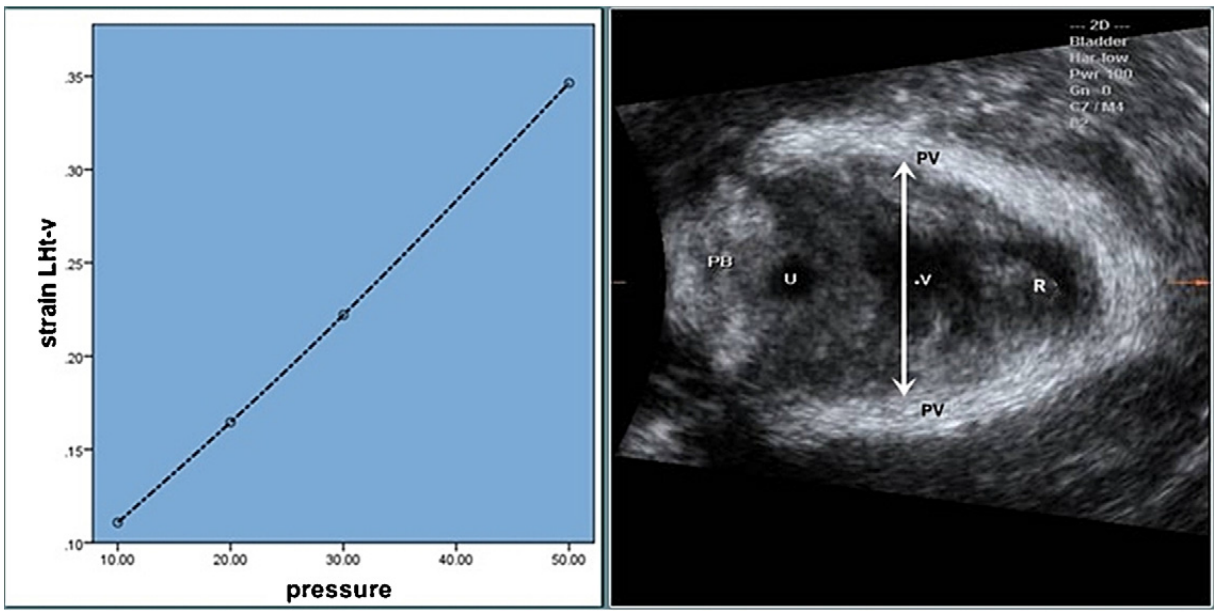

Figure 4.18: Image from Derpapas et al. (2012) showing deformation curve of the levator hiatus in the transverse diameter with Valsalva pressure measured in cm H_20.

relationship from the *in vivo* data, an inverse finite element analysis would be required. In Chapter 2, the muscle had been excised from its attachments and fascia, making the boundary conditions of its deformation significantly different than *in vivo*. In the *in vivo* analysis, points were chosen along the PVM along the apparent fiber direction, but this could not be certain as in the *ex vivo* study where the muscle fibers were clearly visible. Different portions of the LA were analyzed: the samples used in Chapter 2 were from the illioccygeus portion of the LA while the PVM was measured in Chapter 4. In the *ex vivo* study, all of the samples were from post-menopausal women whose PFD status was unknown. In the *in vivo* study, there was a mix of pre- and post-menopausal panelists, and all the post-menopausal women had diagnosed PFD. In the *ex vivo* study, the muscle underwent passive stretching. In the *in vivo* study, the panelists were asked to relax and not to consciously tense their muscles, but because the LA has a resting tone, there would be some active component in its behavior.

From this study, we have shown feasibility of this method to measure stress and strain in

the PVM and discussed ways to improve the method. We were able to obtain biomechanical data similar to results to levator hiatal biomechanical data from a previous study by Derpapas et al. (2012). We did not see a significant difference between the stiffnesses in different regions of the PVM, which was expected. We also did not see a significant difference between the PVM stiffness between the two groups of women, but did see a significant difference in PVM thickness. This lack of statistical significance is probably partially due to small sample size and to the high variability of the method used to measure strain, but may also reflect that PVM stiffness may not be as important as PVM thickness in affecting pelvic floor function.

Chapter V

Summary and Conclusions

5.1 Research Summary

The goal of this dissertation was to measure the mechanical properties of the levator ani (LA) at small strains. Though there is a small amount of data in the literature about levator ani biomechanics, none has concentrated on biomechanics at the small strains seen in daily life. We have performed both *ex vivo* and *in vivo* experiments on the LA, resulting in new data on LA biomechanics and showing feasibility for several methods of measuring strain and pressure in the LA.

In Chapter 2, the passive biomechanics of the LA were measured using samples of the ilioccygeus obtained from post-menopausal, female cadavers. The samples underwent uniaxial extension biomechanical testing and five constitutive models from the literature were fit to the stress-strain data. A power-law model from Sokolis et al. (2002) for arteries at low strains and a hybrid linear-exponential constitutive equation from Fung (1993) for collagen both had very good fits to the stress-strain data. The power-law model had a slightly better fit and has the advantage of only having two fit parameters, making it simpler to implement. This data supports Hypothesis A, that the low strain *in vitro* passive levator ani biomechanical properties can be modeled with a constitutive equation. Using the power-law

model with mean fit parameters may yield more accurate results in FEM of the LA than models currently used. Although it was designed for small strains, it can model properties adequately up to nearly the yield strain. There was a noticeable but statistically insignificant positive correlation between parameter k and age, which is why Hypothesis C was designed to determine if a similar relationship would be seen in the *in vivo* levator ani.

In Chapter 3, a correlation-based texture tracking algorithm was validated and optimized in a model of the pubovisceral muscle (PVM) constructed from bovine skeletal muscle with strain independently measured by sonomicrometry. Volumetric ultrasound images of the PVM model were obtained of a series of incremental indentations into the PVM model. Strains were computed from displacements estimated from the algorithm using both an exponential sum function by Clocksin et al. (2002) and the Pearson correlation coefficient as the likelihood function. Both likelihood functions gave very similar results in most cases, but in one experiment, the Clocksin likelihood performed significantly better. Sub-volumes sized three to four times the correlation length of the image gave the best results. Decorrelation and strain error increased as the magnitude of displacement and strain increased between adjacent images. The results of this chapter support Hypothesis B, that a correlation-based texture tracking algorithm in volumetric ultrasound images measures regional strain of *ex vivo* muscles accurately compared to strain measured independently by sonomicrometry.

In Chapter 4, a study was conducted to determine feasibility of using the algorithm from Chapter 3 to measure *in vivo* deformation of the PVM. Women with and without PFD underwent volumetric ultrasound imaging while the PVM was deformed by a series of incremental volume increases in a transvaginal balloon catheter. The intra-abdominal pressure was estimated from the pressure inside the balloon after adjustment for tension in the balloon wall. Stiffness was calculated as the intra-abdominal pressure normalized by the PVM strain in the posterior right, anterior right, posterior left, and anterior left regions of the muscle averaged over three repetitions of the procedure. The variability of the pressure

measurements was low, but the variability of the strain measurements was high, implying that improvements to how strain is measured may be necessary to provide more repeatable data. Mean PVM stiffness was slightly higher in post-menopausal women, but the difference was statistically insignificant and therefore did not support Hypothesis C, that the *in vivo* stiffness as measured by normalizing the intra-abdominal pressure by level of strain of the PVM is higher in women with diagnosed pelvic floor disorders than in non-symptomatic women. Because the PVM stiffness was close between the two groups, it probably would not be useful for PVM diagnosis. However, if the technique were improved and a larger sample size were used, it could be used to more accurately measure *in vivo* PVM stress and strain which could be combined with the data from Chapter 2 to make a more full model of PVM biomechanics taking into account both active and passive contributions.

5.2 Alternate Applications

The data and techniques used in these studies have applications beyond those specified in this dissertation. The power-law model proposed by Sokolis et al. (2002) that was found to work well for modeling the stress-strain relationship of the passive LA may also be useful for other tissues. The model was designed to be used for the aorta, a smooth muscle, but was shown in Chapter 2 to work very well for the levator ani, a skeletal muscle. While the linear-exponential model proposed by Fung (1993) is more traditional and has the advantage of being easier to interpret as a model of collagen recruitment, the power-law model has the advantage of being easier to implement in a finite element model and showed higher accuracy.

The correlation-based texture tracking algorithm optimized and validated here can be used on any medical images of tissue deformation (Nageswaran, 2008). Some of our preliminary studies involved applying the texture tracking algorithm to ultrasound, digital photography, CT, and MRI images of a variety of soft tissues including the liver, urethra, bladder,

intestinal tract, vagina, uterus, skeletal muscles from many parts of the body, and the heart. It was found that so long as there is sufficient texture in the image and small enough deformations to avoid decorrelation, displacements and strains could be successfully measured. An example of the use of this algorithm for measuring liver motion is found in Hooi et al. (2015), where it was used to measure in-plane displacements of swine liver during an *in vivo* radiofrequency ablation (RFA) treatment.

Echo decorrelation imaging has important applications in guiding RFA and other thermal ablation methods to treat cancerous tumors in real time. Echo decorrelation performs better than other ultrasound monitoring methods for spatial mapping of tissue ablation because it is not degraded by bubble activity, and it is significantly less expensive than MRI monitoring (Mast et al., 2008). The data quantifying the effect of displacement on echo decorrelation is important to allow methods to be developed to compensate for artifactual decorrelation due to motion (Hooi et al., 2015).

5.3 Future Directions

Larger and more varied sample populations of the studies presented could provide additional useful results. This is particularly true for the *in vivo* study of Chapter 4 where an estimated group size of 25 women per group would be necessary to measure a difference in PVM stiffness between women with and without PFD. Although the *ex vivo* passive biomechanical testing of Chapter 2 and the texture tracking algorithm validation of 3 had sufficient sample sizes to provide statistically significant results, a wider range of ages in Chapter 2 would be useful to determine the effect of age on LA biomechanics, and additional experiments in Chapter 3 with different transducers and imaging systems may show which imaging parameters provide the best data for analysis using the texture tracking algorithm.

The procedure of Chapter 4 should be modified to improve strain results so that they

are more repeatable. The PVM stiffness measured in this study can be compared to other stiffness measurements made in the same manner, but to determine the true stress-strain relationship, an inverse, iterative finite element analysis would have to be performed. Then, the data from Chapter 2, representing the passive levator ani biomechanics, could be subtracted from the *in vivo* stress-strain data to isolate the active component of the muscle behavior, which will be useful for use in finite element models. The PVM biomechanics may also be useful as a diagnosis tool, but the PVM stiffnesses from Chapter 4 were very close between the symptomatic women and the asymptomatic women, so there may be other parameters more useful in differentiating the two groups.

In all of the studies presented, viscoelasticity properties were ignored. The experiments were designed to be repeatable regardless of viscoelastic effects: a slow strain rate was used in Chapter 2, and in Chapters 3 and 4, the tissue under deformation had time to relax before imaging commenced. However, the motions performed in daily life do not always involve time for the muscles to relax, so quantifying the viscoelastic properties of the muscle will be important in modeling its full behavior. Further *ex vivo* and *in vivo* experiments are necessary to determine how to model the viscoelastic properties.

This dissertation concentrated on levator ani strains less than 10%, but larger strains are important to investigate as well. This is especially true when modeling the strains of childbirth, but even a maximum pelvic floor contraction and maximum Valsalva have been shown to induce larger strains. In the *ex vivo* uniaxial biomechanical tests, it was found that the model fit to the stress-strain data at strains less than 10% could be successfully extrapolated to 77-100% of the yield strain without high errors. The texture-tracking algorithm is capable of calculating strain at higher levels, provided that the images are of small, incremental displacements to prevent high levels of decorrelation between image frames. The *in vivo* study as currently used would not be able to induce much higher strains in the PVM because the maximum possible diameter of the balloon catheter was only marginally larger

than the maximum diameter used in the current study. However, if the PVM were deformed by a different method, such as having the panelist perform a Valsalva maneuver while 4D volumetric images were recorded, it should be possible to measure larger strains.

Bibliography

Abramowitch, S. D., Feola, A., Jallah, Z., and Moalli, P. A. (2009). Tissue mechanics, animal models, and pelvic organ prolapse: a review. *European Journal of Obstetrics & Gynecology and Reproductive Biology*, 144:S146–S158.

Ahmad, A. N., Hainsworth, A., Williams, A. B., and Schizas, A. M. (2015). A review of functional pelvic floor imaging modalities and their effectiveness. *Clinical Imaging*, 39(4):559–565.

Alam, S. K. and Ophir, J. (1997). On the use of envelope and RF signal decorrelation as tissue strain estimators. *Ultrasound in Medicine & Biology.*, 23(9):1427–1433.

Ashton-Miller, J. A. and DeLancey, J. O. (2007). Functional anatomy of the female pelvic floor. *Annals of the New York Academy of Sciences*, 1101:266–296.

Ashton-Miller, J. A. and DeLancey, J. O. (2009). On the biomechanics of vaginal birth and common sequelae. *Annual Review of Biomedical Engineering*, 11:163–176.

Barber, M. D. (2007). Questionnaires for women with pelvic floor disorders. *International Urogynecology Journal*, 18(4):461–465.

Boresi, A. P., Chong, K., and Lee, J. D. (2010). *Elasticity in Engineering Mechanics*. John Wiley & Sons.

Bourcier, A., McGuire, E. J., and Abrams, P. (2004). *Pelvic Floor Disorders*. Saunders.

Bump, R. C., Mattiasson, A., Bø, K., Brubaker, L. P., DeLancey, J. O., Klarskov, P., Shull, B. L., and Smith, A. R. (1996). The standardization of terminology of female pelvic organ prolapse and pelvic floor dysfunction. *American Journal of Obstetrics and Gynecology*, 175(1):10–17.

Byram, B., Trahey, G., and Palmeri, M. (2013a). Bayesian speckle tracking. Part I: an implementable perturbation to the likelihood function for ultrasound displacement estimation. *IEEE Transactions on Ultrasonics, Ferroelectrics and Frequency Control*, 60(1):132–143.

Byram, B., Trahey, G. E., and Palmeri, M. (2013b). Bayesian speckle tracking.Part II: biased ultrasound displacement estimation. *IEEE Transactions on Ultrasonics, Ferroelectrics and Frequency Control*, 60(1):144–157.

Céspedes, I., Huang, Y., Ophir, J., and Spratt, S. (1995). Methods for estimation of subsample time delays of digitized echo signals. *Ultrasonic Imaging*, 17(2):142–171.

Chen, J.-F., Fowlkes, J. B., Carson, P. L., and Rubin, J. M. (1997). Determination of scan-plane motion using speckle decorrelation: theoretical considerations and initial test. *International Journal of Imaging Systems and Technology*.

Chen, L., Ashton-Miller, J. A., and DeLancey, J. O. (2009a). A 3D finite element model of anterior vaginal wall support to evaluate mechanisms underlying cystocele formation. *Journal of Biomechanics*, 42(10):1371–1377.

Chen, L., Ashton-Miller, J. A., Hsu, Y., and DeLancey, J. (2006). Interaction among apical support, levator ani impairment, and anterior vaginal wall prolapse. *Obstetrics & Gynecology*, 108(2):324–332.

Chen, L., Treece, G. M., Lindop, J. E., Gee, A. H., and Prager, R. W. (2009b). A quality-guided displacement tracking algorithm for ultrasonic elasticity imaging. *Medical Image Analysis*, 13(2):286–296.

Chionh, J. J., Wei, B. P., Martin, J. A., and Opdam, H. I. (2006). Determining normal values for intra-abdominal pressure. *ANZ Journal of Surgery*, 76(12):1106–1109.

Chu, T., Ranson, W., and Sutton, M. (1985). Applications of digital-image-correlation techniques to experimental mechanics. *Experimental Mechanics*, 25(3):232–244.

Clocksin, W. F., da Fonseca, J. Q., Withers, P. J., and Torr, P. H. S. (2002). Image processing issues in digital strain mapping. *Proceedings of the SPIE*, 4790:384–395.

Constantinou, C., Hvistendahl, G., Ryhammer, A., Nagel, L. L., and Djurhuus, J. (2002). Determining the displacement of the pelvic floor and pelvic organs during voluntary contractions using magnetic resonance imaging in younger and older women. *British Journal of Urology International*, 90(4):408–414.

Constantinou, C. E. and Omata, S. (2007). Direction sensitive sensor probe for the evaluation of voluntary and reflex pelvic floor contractions. *Neurourology and Urodynamics*, 26(3):386–391.

DeLancey, J. O. (2005). The hidden epidemic of pelvic floor dysfunction: achievable goalsÂ for improved prevention and treatment. *American Journal of Obstetrics and Gynecology*, 192(5):1488–1495.

DeLancey, J. O., Kearney, R., Chou, Q., Speights, S., and Binno, S. (2003). The appearance of levator ani muscle abnormalities in magnetic resonance images after vaginal delivery. *Obstetrics & Gynecology*, 101(1):46–53.

DeLancey, J. O., Morgan, D. M., Fenner, D. E., Kearney, R., Guire, K., Miller, J. M., Hussain, H., Umek, W., Hsu, Y., and Ashton-Miller, J. A. (2007). Comparison of levator ani muscle defects and function in women with and without pelvic organ prolapse. *Obstetrics & Gynecology*, 109(2, Part 1):295–302.

Derpapas, A., Digesu, A. G., Vijaya, G., Fernando, R., and Khullar, V. (2012). Real-time in vivo assessment of levator ani muscle deformation in women. *European Journal of Obstetrics & Gynecology, and Reproductive Biology*, 165(2):352–356.

Devreese, A., Staes, F., Weerdt, W. D., Feys, H., Assche, A. V., Penninckx, F., and Vereecken, R. (2004). Clinical evaluation of pelvic floor muscle function in continent and incontinent women. *Neurourology and Urodynamics*, 23(3):190–197.

Dickinson, R. and Hill, C. (1982). Measurement of soft tissue motion using correlation between A-scans. *Ultrasound in Medicine & Biology*, 8(3):263–271.

Dietz, H. P. (2010). Pelvic floor ultrasound: a review. *American Journal of Obstetrics and Gynecology*, 202(4):321–334.

Dietz, H. P., Hoyte, L. P., and Steensma, A. B. (2008). *Atlas of Pelvic Floor Ultrasound*. Springer.

Dietz, H. P., Shek, C., and Clarke, B. (2005). Biometry of the pubovisceral muscle and levator hiatus by three-dimensional pelvic floor ultrasound. *Ultrasound in Obstetrics and Gynecology*, 25(6):580–585.

Federative Committee on Anatomical Terminology (1998). *Terminologia Anatomica*. Thieme Stuttgart.

Fung, Y. (1993). *Biomechanics: Material Properties of Living Tissues*. Springer.

Fung, Y. (1994). *A First Course in Continuum Mechanics*. Prentice Hall.

Gao, L., Parker, K., Lerner, R., and Levinson, S. (1996). Imaging of the elastic properties of tissue—a review. *Ultrasound in Medicine & Biology*, 22(8):959–977.

Gao, Y., Kostrominova, T. Y., Faulkner, J. A., and Wineman, A. S. (2008). Age-related changes in the mechanical properties of the epimysium in skeletal muscles of rats. *Journal of Biomechanics*, 41(2):465–469.

Goff, M. L. (2009). Early post-mortem changes and stages of decomposition in exposed cadavers. *Experimental and Applied Acarology*, 49(1-2):21–36.

Hall, T. J., Bilgen, M., Insana, M. F., and Krouskop, T. A. (1997). Phantom materials for elastography. *IEEE Transactions on Ultrasonics, Ferroelectrics and Frequency Control*, 44(6):1355–1365.

Haridas, B., Hong, H., Minoguchi, R., Owens, S., and Osborn, T. (2005). PelvicSim-a computational-experimental system for biomechanical evaluation of female pelvic floor organ disorders and associated minimally invasive interventions. *Studies in Health Technology and Informatics*, 119:182–187.

Holzapfel, G. A. (2000). *Nonlinear Solid Mechanics*. John Wiley & Sons.

Holzapfel, G. A., Gasser, T. C., and Ogden, R. W. (2001). A new constitutive framework for arterial wall mechanics and a comparative study of material models. *Journal of Elasticity*, 61:1–48.

Hooi, F. M., Nagle, A. S., Subramanian, S., and Mast, T. (2015). Analysis of tissue changes, measurement system effects, and motion artifacts in echo decorrelation imaging. *Journal of the Acoustical Society of America*, 137(2):585–597.

Insana, M., Cook, L., Bilgen, M., Chaturvedi, P., and Zhu, Y. (2000). Maximum-likelihood approach to strain imaging using ultrasound. *Journal of the Acoustical Society of America*, 107(3):1421–1434.

Janda, S. (2006). *Biomechanics of the Pelvic Floor Musculature*. PhD thesis, Delft University of Technology.

Jansson, T. T., Mast, T. D., and Waag, R. C. (1998). Measurements of differential scattering cross section using a ring transducer. *The Journal of the Acoustical Society of America*, 103(6):3169–3179.

Jelovsek, J. E. and Barber, M. D. (2006). Women seeking treatment for advanced pelvic organ prolapse have decreased body image and quality of life. *American Journal of Obstetrics and Gynecology*, 194(5):1455–1461.

Jing, D. (2010). *Experimental and Theoretical Biomechanical Analyses of the Second Stage of Labor.* PhD thesis, University of Michigan.

Jing, D., Ashton-Miller, J. A., and DeLancey, J. O. (2012). A subject-specific anisotropic visco-hyperelastic finite element model of female pelvic floor stress and strain during the second stage of labor. *Journal of Biomechanics*, 45(3):455–460.

Kearney, R., Sawhney, R., and DeLancey, J. O. (2004). Levator ani muscle anatomy evaluated by origin-insertion pairs. *Obstetrics & Gynecology*, 104(1):168–173.

Khraishi, T. A. and Shen, Y.-L. (2014). *Continuum Mechanics: Constitutive Equations and Applications*. Momentum Press Engineering.

Lawrence, J. M., Lukacz, E. S., Nager, C. W., Hsu, J. W., and Luber, K. M. (2008). Prevalence and co-occurrence of pelvic floor disorders in community-dwelling women. *Obstetrics & Gynecology*, 111(3):678–685.

Lerner, R. M. and Waag, R. C. (1988). Wave space interpretation of scattered ultrasound. *Ultrasound in Medicine & Biology*, 14(2):97–102.

Li, X., Kruger, J. A., Nash, M. P., and Nielsen, P. M. (2010a). Effects of nonlinear muscle elasticity on pelvic floor mechanics during vaginal childbirth. *Journal of Biomechanical Engineering*, 132(11):111010.

Li, X., Kruger, J. A., Nash, M. P., and Nielsen, P. M. (2010b). Modeling childbirth: elucidating the mechanisms of labor. *Wiley Interdisciplinary Reviews: Systems Biology and Medicine*, 2(4):460–470.

Li, X., Kruger, J. A., Nash, M. P., and Nielsen, P. M. (2011). Anisotropic effects of the levator ani muscle during childbirth. *Biomechanics and Modeling in Mechanobiology*, 10(4):485–494.

Lien, K. C., Mooney, B., DeLancey, J. O., and Ashton-Miller, J. A. (2004). Levator ani muscle stretch induced by simulated vaginal birth. *Obstetrics & Gynecology*, 103(1):31–40.

Lowder, J. L., Ghetti, C., Moalli, P., Zyczynski, H., and Cash, T. F. (2010). Body image in women before and after reconstructive surgery for pelvic organ prolapse. *International Urogynecology Journal*, 21(8):919–925.

Margulies, S. S., Lei, G. T., Farkas, G. A., and Rodarte, J. R. (1994). Finite-element analysis of stress in the canine diaphragm. *Journal of Applied Physiology*, 76(5):2070–2075.

Mariappan, Y. K., Glaser, K. J., and Ehman, R. L. (2010). Magnetic resonance elastography: a review. *Clinical anatomy*, 23(5):497–511.

Markland, A. D., Richter, H. E., Fwu, C.-W., Eggers, P., and Kusek, J. W. (2011). Prevalence and trends of urinary incontinence in adults in the united states, 2001 to 2008. *The Journal of Urology*, 186(2):589–593.

Mast, T. D. (2007). Fresnel approximations for acoustic fields of rectangularly symmetric sources. *Journal of the Acoustical Society of America*, 121(6):3311–3322.

Mast, T. D. (2010). Convolutional modeling of diffraction effects in pulse-echo ultrasound imaging. *The Journal of the Acoustical Society of America*, 128(3):EL99–EL104.

Mast, T. D., Pucke, D. P., Subramanian, S. E., Bowlus, W. J., Rudich, S. M., and Buell, J. F. (2008). Ultrasound monitoring of in vitro radio frequency ablation by echo decorrelation imaging. *Journal of Ultrasound in Medicine*, 27(12):1685–1697.

Moalli, P. A., Howden, N. S., Lowder, J. L., Navarro, J., Debes, K. M., Abramowitch, S. D., and Woo, S. L. (2005). A rat model to study the structural properties of the vagina and its supportive tissues. *American Journal of Obstetrics and Gynecology*, 192(1):80–88.

Morse, P. M. and Ingard, K. U. (1968). *Theoretical acoustics*. Princeton university press.

Nageswaran, A. R. (2008). Deformation analysis of soft tissues by digital image correlation. Master of Science Thesis, University of Cincinnati.

Nagle, A. S., Barker, M. A., Kleeman, S. D., Haridas, B., and Mast, T. D. (2014). Passive biomechanical properties of human cadaveric levator ani muscle at low strains. *Journal of Biomechanics*, 47(2):583–586.

Nagle, A. S., Nageswaran, A. R., Haridas, B., and Mast, T. D. (2013). Validation of three-dimensional strain tracking by volumetric ultrasound image correlation in a pubovisceral muscle model. *Proceedings of Meetings on Acoustics*, 19:75053.

Ng, J., Prager, R., Kingsbury, N., Treece, G., and Gee, A. (2006). Modeling ultrasound imaging as a linear, shift-variant system. *IEEE Transactions on Ultrasonics, Ferroelectrics and Frequency Control*, 53(3):549–563.

Noakes, K. F., Pullan, A. J., Bissett, I. P., and Cheng, L. K. (2008). Subject specific finite elasticity simulations of the pelvic floor. *Journal of Biomechanics*, 41(14):3060–3065.

Noonan, T. J., Best, T. M., Seaber, A. V., and Garrett Jr, W. E. (1993). Thermal effects on skeletal muscle tensile behavior. *The American Journal of Sports Medicine*, 21(4):517–522.

O'Donnell, M. and Silverstein, S. D. (1987). Optimum displacement for compound image generation in medical ultrasound. *IEEE Transactions on Ultrasonics, Ferroelectrics and Frequency Control*, 35(4):470–476.

Ophir, J., Cespedes, I., Ponnekanti, H., Yazdi, Y., and Li, X. (1991). Elastography: a quantitative method for imaging the elasticity of biological tissues. *Ultrasonic Imaging*, 13(2):111–134.

Paramore, R. (1913). The intra-abdominal pressure in pregnancy. *Journal of the Royal Society of Medicine*, 6(Obstet Gynaecol Sect):291–334.

Parente, M. P., Jorge, R. M., Mascarenhas, T., Fernandes, A. A., and Martins, J. A. (2008). Deformation of the pelvic floor muscles during a vaginal delivery. *International Urogynecology Journal and Pelvic Floor Dysfunction*, 19(1):65–71.

Parente, R. C. M., Bergqvist, L. P., Soares, M. B., and Moraes Filho, O. B. (2011). The history of vaginal birth. *Archives of Gynecology and Obstetrics*, 284(1):1–11.

Parker, K., Doyley, M., and Rubens, D. (2011). Imaging the elastic properties of tissue: the 20 year perspective. *Physics in Medicine and Biology*, 56(1):R1.

R Core Team (2013). *R: A Language and Environment for Statistical Computing*. R Foundation for Statistical Computing, Vienna, Austria.

Ren, S., Xie, B., Wang, J., and Rong, Q. (2015). Biomechanics of pelvic organ prolapse. *Science China Life Sciences*, pages 1–3.

Roan, E. and Vemaganti, K. (2007). The nonlinear material properties of liver tissue determined from no-slip uniaxial compression experiments. *Journal of Biomechanical Engineering*, 129(3):450–456.

Saadoun, K., Ringa, V., Fritel, X., Varnoux, N., Zins, M., and Breart, G. (2006). Negative impact of urinary incontinence on quality of life, a cross-sectional study among women aged 49-61 years enrolled in the GAZEL cohort. *Neurourology and Urodynamics*, 25(7):696–702.

Siafarikas, F., Stær-Jensen, J., Hilde, G., Bø, K., and Ellström Engh, M. (2015). The levator ani muscle during pregnancy and major levator ani muscle defects diagnosed postpartum: a three-and four-dimensional transperineal ultrasound study. *BJOG: An International Journal of Obstetrics & Gynaecology*, 122(8):1083–1091.

Sokolis, D. P., Boudoulas, H., and Karayannacos, P. E. (2002). Assessment of the aortic stress-strain relation in uniaxial tension. *Journal of Biomechanics*, 35(9):1213–1223.

Steensma, A. B., Oom, D. M., Burger, C. W., and Schouten, W. R. (2010). Assessment of posterior compartment prolapse: a comparison of evacuation proctography and 3D transperineal ultrasound. *Colorectal Disease*, 12(6):533–539.

Steers, W. D. (2002). Pathophysiology of overactive bladder and urge urinary incontinence. *Reviews in Urology*, 4(Suppl 4):S7.

Suga, M., Matsuda, T., Minato, K., Oshiro, O., Chihara, K., Okamoto, J., Takizawa, O., Komori, M., and Takahashi, T. (2003). Measurement of in vivo local shear modulus using mr elastography multiple-phase patchwork offsets. *IEEE Transactions on Biomedical Engineering*, 50(7):908–915.

Sun, W., Abad, A., and Sacks, M. S. (2005). Simulated bioprosthetic heart valve deformation under quasi-static loading. *Journal of Biomechanical Engineering*, 127(6):905–914.

Taylor, D. C., Dalton Jr, J. D., Seaber, A. V., and Garrett Jr, W. E. (1990). Viscoelastic properties of muscle-tendon units. the biomechanical effects of stretching. *The American Journal of Sports Medicine*, 18(3):300–309.

Temml, C., Haidinger, G., Schmidbauer, J., Schatzl, G., and Madersbacher, S. (2000). Urinary incontinence in both sexes: prevalence rates and impact on quality of life and sexual life. *Neurourology and Urodynamics*, 19(3):259–271.

Thyer, I., Shek, C., and Dietz, H. P. (2008). New imaging method for assessing pelvic floor biomechanics. *Ultrasound in Obstetrics and Gynecology*, 31(2):201–205.

Van Ee, C. A., Chasse, A. L., and Myers, B. S. (2000). Quantifying skeletal muscle properties in cadaveric test specimens: effects of mechanical loading, postmortem time, and freezer storage. *Journal of Biomechanical Engineering*, 122(1):9–14.

Varghese, T. and Ophir, J. (1996). Estimating tissue strain from signal decorrelation using the correlation coefficient. *Ultrasound in Medicine & Biology*, 22(9):1249–1254.

Varghese, T. and Ophir, J. (1997). A theoretical framework for performance characterization of elastography: the strain filter. *IEEE Transactions on Ultrasonics, Ferroelectrics and Frequency Control*, 44(1):164–172.

Varghese, T. and Ophir, J. (1998). Characterization of elastographic noise using the envelope of echo signals. *Ultrasound in Medicine & Biology*, 24(4):543–555.

Waag, R. C., Astheimer, J. P., and Smith III, J. F. (1992). Analysis and computations of measurement system effects in ultrasonic scattering experiments. *The Journal of the Acoustical Society of America*, 91(3):1284–1297.

Walker, W. F. (2001). Significance of correlation in ultrasound signal processing. In *Medical Imaging 2001*, pages 159–171. International Society for Optics and Photonics.

Weber, A. and Brubaker, L. (2004). *Office Urogynecology*. McGraw Hill Professional.

Weir, L. F., Nygaard, I. E., Wilken, J., Brandt, D., and Janz, K. F. (2006). Postoperative activity restrictions: any evidence? *Obstetrics & Gynecology*, 107(2 Pt 1):305–309.

Wells, P. N. and Liang, H.-D. (2011). Medical ultrasound: imaging of soft tissue strain and elasticity. *Journal of The Royal Society Interface*, 8(64):1521–1549.

Wieczorek, A., Stankiewicz, A., Santoro, G., Woźniak, M., Bogusiewicz, M., and Rechberger, T. (2011). Pelvic floor disorders: role of new ultrasonographic techniques. *World Journal of Urology*, 29(5):615–623.

Wu, J. M., Hundley, A. F., Fulton, R. G., and Myers, E. R. (2009). Forecasting the prevalence of pelvic floor disorders in U.S. women: 2010 to 2050. *Obstetrics & Gynecology*, 114(6):1278–1283.

Wu, J. M., Vaughan, C. P., Goode, P. S., Redden, D. T., Burgio, K. L., Richter, H. E., and Markland, A. D. (2014). Prevalence and trends of symptomatic pelvic floor disorders in us women. *Obstetrics & Gynecology*, 123(1):141.

Yang, J.-M., Yang, S.-H., and Huang, W.-C. (2006). Biometry of the pubovisceral muscle and levator hiatus in nulliparous chinese women. *Ultrasound in obstetrics & gynecology*, 28(5):710–716.

Zahiri-Azar, R. and Salcudean, S. E. (2006). Motion estimation in ultrasound images using time domain cross correlation with prior estimates. *IEEE Transactions on Biomedical Engineering*, 53(10):1990–2000.